POWDER BED BINDER JET 3D PRINTING OF ALLOY 625: MICROSTRUCTURAL EVOLUTION, DENSIFICATION KINETICS AND MECHANICAL PROPERTIES

by

Amir Mostafaei

M.Sc of Materials Science and Engineering, Sahand University of Technology, Iran, 2011

B.Sc of Materials Engineering, Science & Research Branch-Islamic Azad University, Iran, 2008

Submitted to the Graduate Faculty of

Swanson School of Engineering in partial fulfillment

of the requirements for the degree of

Doctor of Philosophy

University of Pittsburgh

2018

UNIVERSITY OF PITTSBURGH

SWANSON SCHOOL OF ENGINEERING

This dissertation was presented

by

Amir Mostafaei

It was defended on

July 20, 2018

for the following committees

Brian M. Gleeson, Ph.D., Professor,

Department of Mechanical Engineering and Materials Science, University of Pittsburgh

Ian Nettleship, Ph.D., Associate Professor,

Department of Mechanical Engineering and Materials Science, University of Pittsburgh

Anthony D. Rollett, Ph.D., Professor,

Department of Materials Science and Engineering, Carnegie Mellon University

Dissertation Director: Markus Chmielus, Ph.D., Assistant Professor,

Department of Mechanical Engineering and Materials Science, University of Pittsburgh

POWDER BED BINDER JET 3D PRINTING OF ALLOY 625: MICROSTRUCTURAL EVOLUTION, DENSIFICATION KINETICS AND MECHANICAL PROPERTIES

Amir Mostafaei, PhD

University of Pittsburgh, 2018

Binder jet 3D printing (BJ3DP), a non-beam based, additive manufacturing (AM) method, refers to the technology in which powdered material is deposited layer-by-layer and selectively joined in each layer with binder and then densified through sintering or infiltration. Binder jetting of metals holds distinctive promise among AM technologies due to its fast, low-cost manufacturing; stress-free structures with complex internal and external geometries; and the isotropic properties of the final parts. Also, by taking advantage of traditional powder metallurgy, BJ3DP machines can produce prototypes of metal parts in which material properties and surface finish are similar to those achieved with metal injection molding or traditional powder metallurgy. Therefore, a comprehensive overview of the fundamental science of metallurgical structure after sintering and post heat-treatment steps are provided in this work to understand the microstructural evolution and properties of BJ3DP parts. Further, to determine the effects of the BJ3DP process on metallurgical properties, an empirical framework to describe the role of particle size, morphology and powder size distribution, and sintering followed by a post heat-treatment is discussed. With the growth of AM and the need for post-processing in BJ3DP parts, an understanding of the microstructural evolution is necessary, and in this work sintering steps and mechanisms are explained and aligned with the BJ3DP process.

Nickel-based alloy 625 was BJ3DP from water- and gas-atomized powders for a detailed comparative study on densification behavior, microstructural evolution and mechanical properties

in terms of hardness, tensile strength and fatigue life. Then, gas-atomized alloy 625 powders of three different powder size distributions were printed and sintered in order to extend existing knowledge of sintering of alloy 625 to binder jetted parts. Sintering was evaluated in the context of microstructural evolution, using grain and pore intercept length, pore separation, surface area per unit volume and number of pore sections per unit area. The results suggest that particle size distribution is a determining factor for densification kinetic and final microstructure, if printing parameters such as layer thickness, binder saturation and drying time are similar.

TABLE OF CONTENTS

ACKNOWLEDGEMENTS IX

1.0 INTRODUCTION 1

2.0 BACKGROUND 7

2.1 BINDER JET 3D PRINTING 7

2.2 DESIGN PHILOSOPHY FOR BINDER JET 3D PRINTING 13

2.2.1 Designing the part 13

2.2.2 Powder type and chemistry 14

2.2.3 Powder size distribution (PSD) and morphology 15

2.2.4 Spread speed and print speed 23

2.2.5 Layer thickness and powder packing density 28

2.2.6 Binder selection 36

2.2.7 Binder saturation 37

2.2.8 Drying time 43

2.2.9 Binder burnout, densification and shrinkage 44

2.2.10 Sintering 46

2.2.10.1 Sintering Theory 46

2.2.10.2 Sintering Thermodynamics 49

2.2.10.3 Sintering Kinetics 50

2.2.10.4 Solid-State Sintering 50
2.3 BINDER JET 3D PRINTING OF NICKEL-BASED ALLOYS 53
3.0 HYPOTHESIS 70
4.0 OBJECTIVES 74
5.0 MATERIALS AND METHODS 78
5.1 BINDER JET 3D PRINTING OF ALLOY 625 78
5.2 FATIGUE LIFE STUDIES 81
5.3 KINETIC STUDIES 83
6.0 RESULTS AND DISCUSSION 88
6.1 BJ3DP OF WATER AND GAS ATOMIZED ALLOY 625 88
6.1.1 Powder feedstock characterizations 88
6.1.2 Shrinkage and relative density measurements 90
6.1.3 Microstructural observations 94
6.1.4 XRD analyses and phase formation 102
6.1.5 Phase and microstructure evolution 105
6.1.6 Mechanical properties 106
6.1.7 Summary 110
6.2 CHARACTERIZING SURFACE FINISH AND FATIGUE BEHAVIOR 111
6.2.1 Fatigue testing 111
6.2.2 Materials characterization of the samples 115
6.2.3 Combining characterization and fatigue results 121
6.2.4 Summary 123
6.3 DENSIFICATION KINETICS OF BJ3DP ALLOY 625 124

6.3.1 Summary 153

7.0 FUTURE WORK 156

BIBLIOGRAPHY 158

LIST OF TABLES

Table 1. EDS composition of WA and GA nickel-based alloy 625 powders and oxygen and carbon content of as-received powders and printed/sintered samples [wt.-%]..... 78

Table 2. Grain and pore size analysis and microhardness values of the WA and GA powder alloy 625 sintered samples depending on sintering temperature. 96

Table 3. Chemical composition in wt.-% of the selected points on SEM micrographs in Figure 36. 101

Table 4. Crystallographic parameters of the WA and GA nickel-based alloy 625 samples compared to a γ-Ni reference (ICSD Reference code: 98-011-6293)..... 104

Table 5. Average values of UTS, $YS_{0.2\%}$ and elongation of the BJP WA and GA nickel-based alloy 625 samples..... 108

Table 6. Crystallographic parameters comparison between as sintered and mechanically ground BJ3DP alloy 625 after sintering process. Units for D-spacing, peak position and FWHM are [Å], [°] and [°], respectively. 120

LIST OF FIGURES

Figure 1. Parts produced by Binder Jet 3D-Printing: a) turbine component, 420 stainless steel infiltrated with bronze (design: Airbus Deutschland GmbH); b) mold insert from X190CrVMo20 tool steel, green part (l.) and sintered to full density (r.); c) earring, 316L stainless steel; d) wrench, 420 stainless steel [15]. 6

Figure 2. Schematic of binder jet 3D printing machine with two types of powder feeding techniques, (left) powders are supplied using a hopper and with oscillation, powders are spread on the powder bed and powder compaction is achieved using a roller (e.g. in the M-Flex ExOne printer) and (right) there is a powder supply as a feeder in which a roller swipe powder on the powder bed on the top layer of the built area (e.g. in the X1 Lab printer). 10

Figure 3. (A) Images of individual metal particles, produced using gas atomization, illustrate the many different shapes of particle that may result from the process, (B) effect of Powder morphology on apparent density, (C) variations of Powder Size Distribution and (D) differential (left) and Cumulative (right) Size Distribution [56]. 17

Figure 4. (a) Particle size distributions of four different TiNiHf powders, (b) green strength of 3D mesh structures from four different size particles, (c) . Mesh structure images for four different size TiNiHf powders are illustrated in (d) less than 20 μm, (e) 20–45 μm, (f) 45–75 μm, and (g) 75–150 μm. The left side image is 3D structure, the middle image is 2D mesh wire structure and the right side image is the surface 3D profiles for different powder size [38]. 19

Figure 5. Schematic illustrating the proposed different droplet penetration behavior within (left) homogeneously distributed and (right) heterogeneously distributed powder beds. For close packing powders such as gas atomized powder with spherical powder morphology, the fluid drainage is relatively uninhibited. However, as liquid penetrates powders containing large macro-voids the liquid front will tend to cease when the pore radius increases suddenly. This happens whenever a capillary pore reaches a macro-void (The macro-void space does not contribute to the effective capillary volume or surface area) [62,63]. 20

Figure 6. (A) Morphology and PSD analysis results of (a) 420 SS (b) Ti-6Al-4V powders. (B) Contact angle and specific surface area measurement results. (C) Capillary characteristic curves for 420 SS and Ti-6Al-4V [65]. 22

Figure 7. (A) a: Powder particles with complex geometric shapes, b: light microscope images of some of the powder particles (first row) and corresponding particle models using the multisphere method (second row), c: cumulative and volume density distribution dada, (B) schematic overview of the main element for the simulation, (C) Schematice of the powder roller interaction during printing process, (D) powder layer applied onto the part to be built with various roller speed of 20 mm/s (left) and 180 mm/s (right), and (E) dependence of the surface roughness 'δ' on the coating velocity, 'V_R'. Detailed information can be found in [68]. 25

Figure 8. (A) Powder size distribution and morphology. (B, C) The designed geometry for printing samples and part configuration in the powder bed, schematic of single track and multiple tracks experiments are shown. (D) Printed features with different printing speeds (a) 20 mm/sec (b) 100 mm/sec (c) 300 mm/sec (d) 700 mm/sec (e) 1000 mm/sec. (E) Variation of the slot accuracy with printing speed and part orientation. (F) Effect of printing speed on dimensional accuracy of single-track samples. (G) Dimensional accuracy of multiple-track samples fabricated at various printing speeds. (H) Printing speed effect on accuracy of cubic parts [69]..... 27

Figure 9. A comparison between powder particle size and two layer thicknesses affecting powder bed density. 29

Figure 10. A schematic showing the effect of powder particle size and distribution on packing density for a bimodal mixture, showing five possible structures. The maximum density for a homogeneous mixture f* occurs at a certain mixture, which is far above the rule of mixtures density [80]. 31

Figure 11. Apparent density and Hall flow of gas atomized iron powder as a function of the particle size [81]..... 32

Figure 12. (A) 'a' DS-layering steps for dispensing each powder layer; 'b' setups of the self-developed 3DP machine, (B) working principles of the powder-layering apparatus: 'a' apparatus move- ments for the first smoothing; 'b' apparatus movements for the second smoothing, (C) experimental setup in the layering tests, (D) cavity proportion observed in the powder-layering tests, (E) results of part shifting and flat errors measured on the printed specimens, (F) powder densification results measured in the powder-layering tests, (G) results of uniformity analysis along specimens' length , and (H) results of uniformity analysis along specimens' height..... 35

Figure 13. Possible surface defect formation due to improper saturation level; (a) low-level saturation leads to powder loss, and (b) over-saturation leads to excessive powder bond [88,89]. 37

Figure 14. Optical micrographs of 3D printed TiNiHf square wire from powders with particle size distribution less than 20 μm and mean particle size of ~5.50 μm. Effects of saturation lever and layer thickness are compared [90]..... 39

Figure 15. Different printing layer thickness and binder spreading. 40

Figure 16. (A) Designed 3D network structure, (B) diagram of tensile stress–strain for uninfiltrated ZP102 powder, (C) diagram of flexural stress–strain for uninfiltrated ZP102 powder. Stereomicroscope images of specimens with (D) 0.1 mm layer thickness and 90% saturation, (E) 0.087 mm layer thickness and 90% saturation, (F) 0.1 mm layer thickness and 125% saturation, (G) 0.087 mm layer thickness and 125% saturation [39]. 42

Figure 17. Schematic of parts printed with different in-process binder curing parameters (a) insufficient drying parameters (b) appropriate drying parameters (the dashed arrows indicate the potential binder migration paths inside the powder bed) [65]..... 44

Figure 18. (A) Cellular material sample in its various representations during the manufacturing process chain: (a) CAD model, (b) green part, and (c) part after sintering [91]. (B) CAD model, green part and sintered sample with dogbone shape [52]. 45

Figure 19. Schematic showing the general sintering process for a powder system, (a) un-sintered powder, (b) initial stage of sintering where sinter necks form, (c) intermediate sintering stage where the density increases due to shrinkage and pores closure, and (d) final stage where the grain coarsening may happen [97]. 48

Figure 20. Two-particle geometry for possible transport mechanisms during solid-state sintering (detailed explanation can be found in [98,101]). 52

Figure 21. (a) Effect of layer thickness and sintering temperature on the density of alloy 718 parts produced by binder jetting and (b) shrinkage percentage of the alloy 718 depending on sintering temperature [113]. 56

Figure 22. Optical micrographs taken from the BJ3DP alloy 718 printed with the layer thickness of 100 μm and 125 μm and sintered at different temperatures for 4 h [113]. Yellow arrows indicate porosity. 57

Figure 23. Scanning electron micrographs taken from sintered sample at (a,b) 1280 °C showing precipitate formation and (c,d) 1300 °C showing the partially dissolved precipitates [113]. 57

Figure 24. (a) Powder size distribution from gas atomized alloy 718. (b) Scanning electron micrographs with two magnification for (c) 7 μm, (d) 21 μm, and (e) 70 μm powder particles [17,37]. 59

Figure 25. (a) Shrinkage for the three different powder sizes as a function of temperature, (b) Temperature dependence of liquid volume fraction for the three different powder samples based on Thermocalc calculations, (c-f) Optical micrographs comparing

porosity in 7 μm, 21 μm, and 70 μm samples sintered at 1290 °C and the reduction in porosity of 21 lm sintered at 1330 °C [26]. 61

Figure 26. SEM micrographs taken from BJ3DP alloy 718 with three different powder sizes and sintered at two temperatures. Here, dependence of neck size on particle size and sintering temperature in solid-state sintering regime is illustrated [26]. Binder saturation level was reported as 80%, 80% and 70% for sample printed from powder size of 7 μm, 21 μm and 70 μm, respectively. 62

Figure 27. Scanning electron micrographs comparing microstructures of alloy 718 samples printed from three different powder particle size and then sintered to attain maximum density of 99.9% [26]. 65

Figure 28. (a) SEM micrographs of the alloys 625 powder, (b) powder size distribution, (c) DSC-TGA curves of the alloy 625 powder, (d) optical micrographs of the sintered parts, (e) relative density of samples sintered at different temperatures ranging from 1200 to 1300 °C, (f) dimension and volume variations of the sintered samples depending on sintering temperature, (g) SEM micrographs taken from the sintered samples,..... 68

Figure 29. Powders characterization: SEM micrographs of nickel-based alloy 625 powders: (a) WA powder and (d) GA powder. SEM cross sectional micrographs taken from the (b) WA and (e) GA powders showing pores inside the atomized powders. μCT scans of the as-received nickel-based alloy 625 powders contained in a plastic straw (c) WA and (f) GA. 89

Figure 30. (a) Particle size distribution and (b) DSC and TGA curves of WA and GA alloy 625 powders. 89

Figure 31. μCT images of the as-printed, alloy 625 powder sample (a) WA powders and (b) GA powder..... 91

Figure 32. (a) Average shrinkage values of the WA and GA nickel-based alloy 625 sintered samples depending on sintering temperature. (b) Relative density of the GA and WA nickel-based alloy 625 samples based on the optical micrograph analysis using ImageJ software and Archimedes method. Data points are staggered at each temperature for better readability even though sample sets were sintered at the indicated temperatures (e.g. 1225 °C). 92

Figure 33. Optical microstructure of the WA nickel-based alloy 625 samples sintered at (a) 1225 °C, (b) 1240 °C, (c) 1255°C, (d) 1270 °C, (e) 1285 °C, and (f) 1300 °C for 4 h. 95

Figure 34. Optical microstructure of the GA nickel-based alloy 625 samples sintered at (a) 1225 °C, (b) 1240 °C, (c) 1255°C, (d) 1270 °C, (e) 1285 °C, and (f) 1300 °C for 4 h. 97

Figure 35. SEM micrographs of the WA nickel-based alloy 625 samples sintered at (a) 1225 °C, (b) 1255°C, (c) 1285 °C, and (d) 1300 °C for 4 h. SEM micrographs of the GA nickel-based alloy 625 samples sintered at (e) 1225 °C, (f) 1255°C, (g) 1285 °C, and (h) 1300 °C for 4 h..... 99

Figure 36. SEM micrographs with corresponding EDS point analysis taken from the (a) WA and (b) GA samples sintered at 1300 °C. (c,d) SEM micrographs of a GA sample sintered at 1285 °C for 4 h and then aged at 745 °C for 20 h. (e) SEM micrographs of a WA sample sintered at 1270 °C for 4 h and then aged at 745 °C for 20 h..... 100

Figure 37. XRD patterns of the as-received powders and sintered WA and GA nickel-based alloy 625 samples: (a) GA powder, (b) GA sintered at 1225 °C, (c) GA sintered at 1300 °C, (d) GA aged for 20 h, (e) WA powder, (f) WA sintered at 1225 °C, (g) WA sintered at 1300 °C, (h) WA aged for 20 h..... 103

Figure 38. Schematic showing phase and microstructure evolution model for differently heat-treated BJP alloy 625 samples from gas- ad water-atomized powder. 106

Figure 39. (a) Average microhardness values and (b) Engineering stress–strain curves of the WA and GA nickel-based alloy 625 samples sintered at different temperatures for 4 h. Data points are staggered at each temperature for better readability even though sample sets were sintered at the indicated temperatures (e.g. 1225 °C). 107

Figure 40. SEM micrograph of the fracture surface after tensile test taken from the GA sample (a) sintered at 1285 °C and then (b) aged at 745 °C for 20 h; and WA sample (c) sintered at 1270 °C and then (d) aged at 745 °C for 20 h..... 109

Figure 41. Fatigue life data of the BJ3DP alloy 625 for the as-printed condition (black points) and after mechanical ground (red). The horizontal arrows indicate that the runout condition of 10^7 cycles has been met and the test was stopped. For comparison, fatigue data is included from Ref. [165] for cast samples of alloy 625. 112

Figure 42. Fatigue fracture, crack initiation and crack growth micrographs taken from the as-sintered samples at the applied stress value of (a) 175 MPa, (b) 275 MPa and (c) 375 MPa. (d) Selected fracture surface of the mechanically ground sample at the applied stress value of 350 MPa. Two different fracture modes are shown in BSE micrographs as transgranular (TG) and intergranular (IG) fatigue fracture failures. Different magnifications indication regions with different features such as brittle and ductile fractures..... 114

Figure 43. Optical micrographs of the external surface of the samples (a,a_1) as-printed part from gas atomized powder, (b,b_1) as-sintered, and (c,c_1) mechanically ground. 115

Figure 44. Optical profilometry was used to collect surface scans of the material in its (a) as-sintered and (b) and mechanically ground state. (c) Line scans of topography were collected using stylus profilometry. (d) The h_{rms} value is compared between conditions. 117

Figure 45. Optical micrographs taken from the cross-section of the central part of the fatigue sample in which failure may happen. Comparison shows that he as-printed sample has a rough surface while the mechanically ground sample shows smooth surface..... 118

Figure 46. Hardness measurements on the as-sintered and mechanically ground fatigue samples. 119

Figure 47. XRD patterns taken from the curved surface of the as-sintered and mechanically ground samples..... 120

Figure 48. Cumulative and volume percentile results indicating powder size distribution for (a) original powder defined as 16-63 μm, (b) sieved powder with particle size below 25 μm, defined as 16-25 μm, and (c) sieved powder with particle size between 53 and 63μm, defined as 53-63 μm. 124

Figure 49. Optical micrographs of BJ3DP alloy 625 samples sintered at different temperatures for 4 h..... 125

Figure 50. (a) Solid volume fraction obtained from image analysis shown in Figure 49, (b) relative density for different particle sizes as a function of temperature and (c) linear shrinkage in x, y and z directions for the three different powder particle sizes as a function of temperature. 128

Figure 51. Optical micrographs of the BJ3DP alloy 625 samples sintered at 1240 °C. 130

Figure 52. Optical micrographs of the BJ3DP alloy 625 samples sintered at 1270 °C. 131

Figure 53. Optical micrographs of the BJ3DP alloy 625 samples sintered at 1280 °C. 132

Figure 54. (a-c) Relative or apparent density, (d-f) comparison between density obtained from Archimedes method (solid points) and image analysis results (emply points), (g-i) linear shrinkage as a function of temperature, and (j-l) surface area per unit volume results. 136

Figure 55. Volume strain rate (densification rate) vs (a-c) density or (d-f) holding time indicating the relationship for isotermal sintering of different powder particle sizes. 138

Figure 56. The average grain, pore and pore separation intercept length plotted against density. Samples were BJ3DP from three different powder sizes and distibutions of alloy 625. 140

Figure 57. The average grain, pore and pore separation intercept length plotted against sintering time. Samples were BJ3DP from three different powder sizes and distributions of alloy 625..... 141

Figure 58. Dimenssionless results vs. relative density for (a-c) the pore separation to grain intercept ratio, (d-f) the grain to pore intercept ratio, and (g-i) The solid-solid surface area to solid-vapor surface area ratio. Samples were BJ3DP from three different powder sizes and distibutions of alloy 625..... 143

Figure 59. Dimenssionless results vs. sintering time for (a-c) the pore separation to grain intercept ratio, (d-f) the grain to pore intercept ratio, and (g-i) The solid-solid surface area to

solid-vapor surface area ratio. Samples were BJ3DP from three different powder sizes and distibutions of alloy 625. 144

Figure 60. Number of pore sections per unit area against relative density or sintering time for the BJ3DP from three different powder sizes and distibutions of alloy 625. 147

Figure 61. Plot of log volume strain rate against log inverse intercept length of grain intercept for the BJ3DP from three different powder sizes and distibutions of alloy 625. 149

Figure 62. Schematic of the green parts, initial, intermediate and final stage of sintering of the BJ3DP parts from three different powder sizes and distibutions of alloy 625. Red dash lines shown in green parts are indicative of the printed layers with 100 μm thickness. After sintering, samples experienced shrinkage. In the final stage of sintering, residual pores are displayed by red color. 151

Figure 63. SEM micrographs taken from the 16-63 μm powder sintered at 1280 °C for 4 h. a very small liquid film was observed at the boundaries. 153

ACKNOWLEDGEMENTS

I would like to sincerely thank my advisors Prof. Markus. Chmielus for his support, ideas, guidance, and organizational help during the last four years. I also want to appreciate Prof. Ian Nettleship for his invaluable ideas and comments on the densification kinetics and microstructural evolution of the binder jetted alloy 625. I would also like to thank Dr. Tevis Jacobs for assisting with surface roughness analysis and relevant discussion on the fatigue behavior of the binder jetted alloy 625. At University of Pittsburgh, I want to thank my colleagues Erica Stevens and Jakub Toman for their great help, ideas on microscopy and mechanical testing. I want to thank especially Pierangeli Rodriguez De Vecchis for her hard working, enthusiasm, assisting with sample preparation, microscopy, image analysis and fruitful discussions on different parts of my research at the University of Pittsburgh.

This work was supported by the Air Force Research Laboratory [agreement number FA8650-12-2-7230], the Commonwealth of Pennsylvania, acting through the Department of Community and Economic Development [Contract Number C000053981], the NSF [grant number 1434077, REU supplement], and the Swanson School of Engineering. Additionally, I would like to thank Elsevier and Springer for permission of reprinting few images as well as using one of my research article as part of my dissertation (section 6.1). All figures and section were properly cited accordingly. Besides, I am preparing new manuscripts for new submission in Elsevier from section 2.0 (as part of a review on the binder jetting), section 6.2 (fatigue behavior) and section 6.3 (will be presented as two manuscripts).

Finally, I want to thank my family, my parents Mohammad Ebrahim Mostafaei and Mahin Bigdeli, my sister Anahita Mostafaei and especially my wife Linmin (Carolyn) Kang for their continuous support and confidence.

1.0 INTRODUCTION

In recent decades, there are significant attention to the production of parts with complex geometry from different types of materials such as high temperature alloys, high entropy alloys, biomaterials, shape memory alloys, structural materials and ceramic. Over the years, several common processing steps for manufacturing with subsequent post processing are developed.

Casting technique is one of the common conventional methods for producing polycrystalline materials and/or single-crystal made from nickel-based, chromium-based, and stainless steel. In this technique, pre-alloyed or pure materials are melted at high temperature which may result in an increase in the impurity level (e.g., carbon, oxygen), and segregation during solidification affecting properties of the final product. In structural and high temperature alloys, corrosion resistance and mechanical properties might be affected by segregation and composition gradient in the alloy. Additionally, localized corrosion attack can be due to composition variation leading to the galvanic cell formation and selective corrosion of an element and/or alloy. In shape memory and magnetic shape memory alloys, crystal structure as well as secondary phases formation influence phase transformation temperature and twin boundary motion [1,2]. Besides, machinability is the other challenge for different types of materials such as high strength stainless steel and nickel-based alloys 625 and 718, magnetic shape memory materials (showing brittle nature due to the formation of intermetallic composition), super-ductile alloys (e.g. nitinol) which results in excessive tool wear [3].

Powder metallurgy (PM) and metal injection molding (MIM) are other conventional techniques used for producing near-net-shape parts. Powder preparation and feedstock preparation are required steps prior to PM and MIM processing, respectively. One of the main drawbacks of PM method is the high impurity pick-up resulted from the large surface area of the powder particles. In MIM technique, considerable amount of polymer is mixed with the metal powder, therefore de-binding and burn-out steps are required to remove polymer; however, carbon and oxygen residue on the powder surface may lead to prior particle boundary (PPB) formations [4]. In fact, surface oxides on the powder as well as the presence of carbon in the used polymer at particle surfaces are preferential nucleation sites for carbides. Moreover, these techniques are limited in the producing complex components and controlling the size and shape of porosity [5].

Thus, traditional manufacturing of metallic material components from castings, powder metallurgy and thermomechanical processing methods includes extensive effort in terms of post processing and machining to achieve final product with the desired geometry. During past decades, additive manufacturing has attracted attention for processing of different materials since AM techniques have circumvented many of the challenges associated with the conventional methods. AM technologies, also known as 3D printing, is a process of selectively adding material, usually layer upon layer, to create an object from three-dimensional (3D) model data in contrast to traditional subtractive manufacturing, which creates a considerable amount of waste. AM provides the possibility of directly manufacturing parts with internal and external complexity designs, with limited material and chemical waste, superior control of part size and shape, and rapid prototype creation from various materials such as metal, polymer, ceramic, sand and glass [6,7]. Other advantages of AM are a lower number of required parts for complex design solutions and rapid creation of product prototypes and design iterations, which results in a faster market introduction

[6]. Besides, there is no specific tooling required to make the AM part while forging, casting and even highly complex machining components all require some form of tooling to be made to produce the parts. Therefore, timing and costs can be cut down since tooling does not need to be designed, produced and delivered.

Generally, AM techniques can be divided into two categories including (1) fusion based methods such as direct energy deposition (DED), selective laser melting (SLM), electron beam melting (EBM) and direct metal laser sintering (DMLS), and (2) non-beam based methods such as binder jet 3D printing (BJ3DP) and hybrid additive manufacturing system integrating binder jetting and material extrusion [8]. Post-processing may include light machining of support material, surface finishing, sintering, and infiltration depending on the 3D printing methods [9]. In contrast to the conventional cast and injection molding techniques of material processing, in AM, there are limited options to modify microstructures after manufacture, mostly because products are fabricated to near-net shape; however, post heat-treatment may alter microstructure and properties.

While there is extensive literature on the use of fusion based AM technologies (e.g. melting and solidification) on structural [9], biomaterial [10], functional materials [3] and microfabrication [11], there has been limited research on the use of binder jetting, especially published works have mainly presented microstructure and density studies rather than characterization of properties such as mechanical, thermal and magnetic behavior. The BJ3DP of metallic component has its origins in metal powder technology, sintering and prototyping [12]. Successful understanding of a specific BJ3DP process includes the printing process as well as the formulation of an appropriate combination of a powder and binder material system along with process details for printing and post-processing to attain final parts with desired mechanical properties. The existing knowledge base in these technologies is useful, however, it may not address many of the important features

of BJ3DP including (1) powder characteristics control and qualification, (2) binder strength, stability and burnout characteristics and (3) correlation of sintering kinetics to complex geometries. It is important to keep in mind that creating a specific instantiation of BJ3DP with a new material combination requires a number of steps such as (1) Powder formulation and characteristics, (2) binder selection and its deposition method, (3) liquid binder formulation, it compatibility with printing and powder, (4) specification of printing process parameters (e.g. printing speed, layer thickness, drying time, roller speed etc.), and (5) specification of post-processing procedures (e.g. sintering, infiltration, post heat-treatment, surface finish etc.). Although the many decades of research efforts have resulted in a relatively mature knowledge base of powder metallurgy and sintering, the path forward for the research and development of BJ3DP of metallic materials is going to be a long road. The journey has already begun with a growing interest for research, particularly of structural metallic materials, biocompatible, composite and functional materials. Compared to other AM methods, BJ3DP is relatively new and rapidly evolving, a periodic assessment of our understanding is vital and here we seek to fulfill this need. With a resolution similar to or better than most of the rapid prototyping systems, binder jetting also provides a distinctive opportunity to take advantage of earlier works in other fields and adapt them successfully. In general, the pre- and post-processing steps of an adapted powder-based method may remain similar, however, BJ3DP can be used to fabricate shapes with complexity that are difficult or impossible to be created by traditional means.

The thermal post-processing steps (e.g. sintering and/or infiltration) for ceramics and metals are similar to those in traditional powder metallurgy methods and do not need the potentially extensive laser optimization experimentations as required for selective laser sintering (SLS) [13] and selective laser melting (SLM) [14]. Compared to fusion based methods, BJ3DP

systems usually cost significantly less than other AM systems that can produce metallic parts. In addition to the AM machine cost, operating costs are lower and numerous parts can be binder jetted in one run. Another benefit of a binder jetting system is the operation at ambient temperature without controlling atmosphere during production. Compared to the fusion based AM methods that have restrictive built size, binder jetting is capable of 3D printing parts of any applicable size. However, BJ3DP is usually unable to process ultra-fine and loosely packed powders since ultra-fine powders are difficult to spread owing to low flowability and potential powder agglomeration due to humidity, creating defects in the green parts. As a drawback of the binder jetting method, one may point out that the printed parts require post processing and typically have considerable porosity. However, it is worth mentioning that this feature is unique in additive manufacturing due to controlling the porosity and microstructure of the post-processed part based on the application. Finally, many different types of powder (polymers, metals and ceramics) can be binder jetted since BJ3DP is a non-thermal process in which the issues surrounding cracking, over-heating, segregation etc. such as those seen in fusion based AM methods are not present. In Figure 1, examples of binder jetted parts with different materials and then sintered or infiltrated to attain near-full density are shown.

A detailed review on the binder jetting of different materials is conducted, particularly on the printing process, structure, post-printing processes followed by characterization of the final products. Binder jetting is explained in details and design psychology for 3D printing is addressed. The mature knowledge based of powder characteristics, Powder/binder interaction during printing process, sintering and metallurgy can provide powerful synergistic benefit for deeper scientific understanding of BJ3DP. Further-Existing knowledge on sintering process has been extended to binder jet 3D printing in which solid-state sintering, liquid-phase sintering and super solidus

liquid-phase sintering conditions are applied on the BJ3DP components to produce parts with relative densities from porous (~45%) to near-full density (~99%). This review emphasizes on the understanding of binder jetting additive manufacturing and its future capability in the production of complex parts. It is hoped to be helpful to comprehend the current state of the technology, the gaps in scientific work and the research needs most beneficial for the advancement and expansion of BJ3DP of different materials.

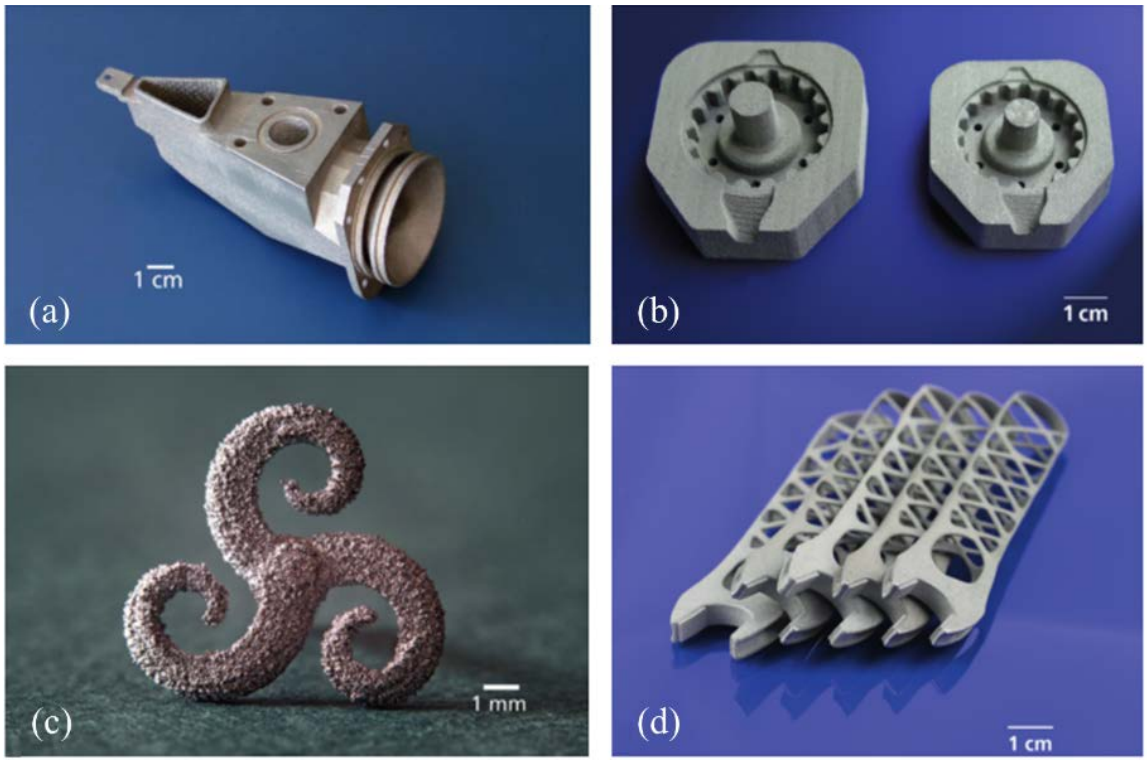

Figure 1. Parts produced by Binder Jet 3D-Printing: a) turbine component, 420 stainless steel infiltrated with bronze (design: Airbus Deutschland GmbH); b) mold insert from X190CrVMo20 tool steel, green part (l.) and sintered to full density (r.); c) earring, 316L stainless steel; d) wrench, 420 stainless steel [15].

2.0 BACKGROUND

2.1 BINDER JET 3D PRINTING

Additive manufacturing (AM) describes a set of new manufacturing methods, processes and technologies that produce parts through material addition, in contrast to the established traditional subtractive manufacturing methods. Design and printing of complex geometries, waste elimination and recycling of the used materials are merits of AM technology [16]. Rapid prototyping is the most extensive use of AM principles, by fabricating of models and prototypes for concept assessment as well as functional testing of new products. In general, AM uses computer-aided design and manufacturing (CAD/CAM) to facilitate the build-up of materials. Therefore, the main advantage of rapid prototyping includes 3D printing allows accurate, one-time fabrication of complex structures of various materials with properties that are highly desirable in many applications including personalized medical and dental applications with tailoring of parts to each patient [17] and aerospace components [18].

Binder jetting (one of the AM classes based on ASTM standard), also referred to as binder jet 3D printing (BJ3DP), is an AM method in which metal powder or sand is deposited layer-by-layer and selectively joined in each layer with binder, a polymeric liquid [19]. BJ3DP, also known as powder bed binder jet printing and 3D printing, was initially developed at the Massachusetts

Institute of Technology and patented in 1993 [20]. Compared to fusion-based AM methods, binder jetting has received less attention in industry and the research community.

To form the 3D green parts, the following steps are performed [21]:

(i) A 3D CAD file is sliced into layers, and an STL file is generated and used as BJP input.

(ii) During BJP, each layer begins with a thin distribution of powder over the surface of a powder bed. Then, a roller compacts and smoothens the new layer.

A 3D printer can be separated into four parts as follows:

- Feed stage that provides dry powder or slurry for powder feeding and indicates deposited layers with smooth surface and uniform thickness. In wet powder binder jetting, mixture of a solid and liquid is used to form a homogeneous slurry [22,23].
- Leveling roller is required after formation of a homogenous powder packing or slurry forming on the powder bed. Leveling rollers are used to feed the powder from the feed stage to the build stage. Based on the 3D printer and applications, different leveling rollers are available. There are two main methods for spreading the new layer, including traversing counter-rotating roller is the most common one that roller rotates the opposite direction to the traversing direction and feeds new layers from the powder bed without disturbing the previous layers. Typically, a piston that supports the powder bed lowers the part-in-progress so that a roller spreads powder from the powder supply, as in the X1 Lab printer [24]. The other type of the leveling roller can be a recoater that spreads powder from the powder supply using oscillation, and then a traversing counter-rotating roller swipes the extra powder to smoothen powder be, as in the ExOne M-Flex printer [25]. Schematic of two types of binder jet 3D printers is shown in Figure 2.
- Build stage is the area that the powder bed is ready for printing step.

❖ Binder jetting head (printhead) that sprays binder on which the part is forming.

(iii) A binder is jetted onto the powder layer via ink-jet cartridges and selectively joins powder particles where the object is to be formed. A water- or solvent-binder can be used during printing the green part. The volume of the sprayed binder is defined by the binder saturation parameter as an input parameter based on the estimation of powder packing density. The binder saturation, *S*, is expressed as $S = V_{binder}/V_{air}$ where V_{binder} is the volume of binder and V_{air} is the volume of open spaces i.e. pores in the powder bed [26]. Based on an estimate of the powder bed density, binder saturation is calculated and used as an input by the user.

(iv) After printing each layer, the build stage in the built box goes down for the next layer of printing. During printing step, binder saturation level denotes the ratio of binder to bed volume. This parameter basically depends on the droplet spacing and size, bed packing density and layer thickness [14]. If the binder saturation level is too high, it might result in excess powder binding causing heterogeneous and uneven surface on the build bed; however, a low saturation level may lead to insufficient binder penetration into the powder and delamination happens. Drying time after printing of each layer is an important factor, in which enough drying time is required to let binder fully bound with powder to avoid cracking of the powder bed or agglomeration and sticking of powder on the roller's surface during printing. Finally, the preferred layer thickness is at least three times that of the powder particle size.

(v) After printing step, the green part is then heated in an oven at about 200 °C (depending on the used binder) to cure the binder and increase strength of the BJ3DP part [27]. The binder is cured to hold the powder together to fabricate the component, however, the product is still fragile at this step and needs densification. Watters et al. proposed a protocol for improved strength of binder-jetted 3D printed parts [28].

(vi) To get the 3D parts after curing step, the excess powder should be removed from the part. Depowderization is conducted on the cured parts to remove extra powder and then the BJ3DP metal powder part follows debounding and sintering for densification. Processing steps are summarized in Figure 2. Some green parts or even partially sintered products are infiltrated with a second material to further improve mechanical properties. Infiltration of the 3D printed parts can be divided into processes including low-temperature (for low temperature materials such as polymenrs) and high-temperature materials (ceramics and high temperature alloys).

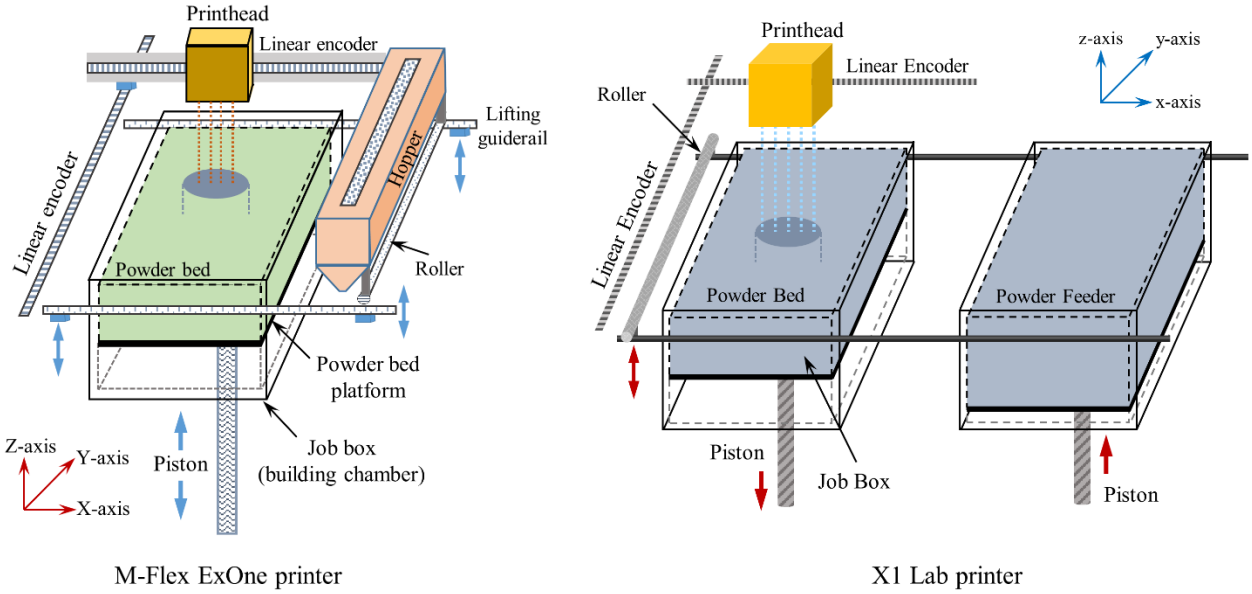

Figure 2. Schematic of binder jet 3D printing machine with two types of powder feeding techniques, (left) powders are supplied using a hopper and with oscillation, powders are spread on the powder bed and powder compaction is achieved using a roller (e.g. in the M-Flex ExOne printer) and (right) there is a powder supply as a feeder in which a roller swipe powder on the powder bed on the top layer of the built area (e.g. in the X1 Lab printer).

Printing ceramic and polymer with binder or ink jetting may seem similar in terms of the printing process, however, densification and consolidation will be quite different [29,30]. With regards to ceramics, due to the high melting point of the printed part, necking among powder may happen and high density should be achieved by infiltration. With regards to polymers, polymerization happens after each layer printing by applying UV light. In some cases, the BJ3DP parts are infiltrated with copper, bronze etc. to achieve higher density. Since the powder does not melt during printing, the density after printing is about 50%. Densification is achieved in different ways such as infiltration (using bronze) [31] or sintering [26,32] and hot isostatic pressing [27]. Therefore, the fundamental steps in printing of different materials with binder jetting are similar while post processing for densification are very different.

Important features of the AM processes are maximum size of the component that can be fabricated, their production times, ability to produce complex parts and the product qualities such as dimensional accuracy and defects of the final product. In fusion based AM processes, a build plate is added to the part to get stability during printing processes, and therefore requiring more time and material; while in BJ3DP, the part is supported by loose powders in the job box. Additionally, no support structure is required for any part geometry produced by BJ3DP while other AM methods basically need support structure if there are overhanging features. In fact, binder jetting is a powder bed technique. Unlike fusion AM processes in which heat source is required to create part leading to residual stresses in the final product, there is no employed heat during the build process in BJ3DP of material. In powder based AM processes, the production time is high due to the limitations of powder feeding rate, scanning speed and low layer thickness. However, large parts can be produced using binder jetting and is often more cost effective than other additive manufacturing methods. Besides, products with wide variety of shape, size and thickness can be

fabricated. Compared to the fusion based AM techniques, various densities with controlled porosity in terms of shape and size are achievable using binder jetting based on the sintering temperature and holding time [33,34]. Additionally, BJP parts do not have thermally-induced stresses and distortions due to large thermal gradients and binder jetting has no difficulties building overhanging structures [35]. Therefore, BJ3DP can be a potential method to attain controlled microstructure regardless of the parts dimensions. The main companies that produce commercial binder jetted 3DP machines is a follow: (1) ProMetal, a division of ExOne Company (Irwin, PA), has a sand-based metal casting system as well as metal-based material systems, including nickel-based alloys, stainless steels, bronze, and high noble gold, (2) Voxeljet Technology (Augsburg, Germany) has a sand-based system for metal casting and a PMMA-based system for plastic parts, (3) Z-Corporation Company (Burlington, MA) also has a sand-based system for metal casting as well as systems for composite or elastomeric parts. The lack of readily available material systems as well as size of the products can be two main challenges and motivating factors for the creation of new material systems and 3DP machines. As a well-known group in utilization of BJ3DP technique, ExOne Company (digital part materialization) manufactures wide range of binder jet 3D printers for different applications with built volume and speed from 160×65×65 mm^3 and 30 s/layer (Innovent printer) to 1800×1000×700 mm^3 and 60-85 L/h (S-Max printer) [36]. Therefore, binder jetting is a scalable technology as it does not require an enclosed chamber and features high throughput enabled by the inkjet printing technology [37].

During BJ3DP process, defects may show up due to powder features incorporated with improperly chosen printing parameters. The cavity-type layering defects, which come together with powder failure, indicates that the powder on the top surface are peeled from the smooth powder-layer surface along with the free flow of powder particles, leaving hollows on the powder

bed surface. Moreover, part shifting is considered as another main type of layering defects in which undesirable part dragging happens within the powder bed and layer location was slightly altered within each layer. Many researches have studied the influence of powder and printing processes effects on the BJ3DP parts, such as the effect of particle sizes [38]; layer thickness and binder saturation [39], layer thickness and printing direction [40], and the effect of printing parameters on the layering defects formation is investigated in [41].

2.2 DESIGN PHILOSOPHY FOR BINDER JET 3D PRINTING

Due to limited published work on the BJ3DP from metallic powder, it is important to be aware of a pathway to fabricated product and conduct in-depth investigations on the effects of each parameter on the final material quality i.e. ease of depositing green part, porosity, and microstructure of the final part. One may consider the following steps and variables in fabrication of near-net shaped parts using BJ3DP:

2.2.1 Designing the part

Generally, binder jetting is capable of printing almost any geometry from any type of powder (polymer, ceramic, metal etc.) by depositing the binder selectively on the powder bed. One limitation in any powder bed AM technique is that after printing the part is with internal channels, the part geometry should involve at least one outlet to remove the loose powder particles from the hollow surfaces. The powder can be extracted and recovered as long as the outlet size is three times that of the powder diameter [26]. Additionally, nozzles of the printhead and binder saturation may

affect this limitation. Nandwana et al. reported that powder recovery from an outlet smaller than 200 μm is extremely difficult even if the outlet is larger than the powder.

2.2.2 Powder type and chemistry

The materials used in BJ3DP fall into two main categories including (1) material powder that makes up the bulk of the green part and basically remains after the sintering process, (2) powder binder made from a solid-state binding agent that is mixed with the material powder. The binder powder composes a small portion of the green part, in the range of the 1-4 wt%. These powders fit into the interstitial spaces between the material powder particles and enhance the green part strength while the green part density decreases leading to the higher shrinkage after sintering step. Powder chemistry indicates how the thermodynamics of solidus and liquidus curves of a material may change and the knowledge of powder feedstock chemistry, particularly trace elements such as S, B, C, Zr in Fe- and Ni-alloys known to lower the melting point, is important in choosing appropriate sintering process [42–44].

Two commonly used atomization techniques to produce metal powder are (1) gas atomization (GA), which results in spherical particles and high packing density and (2) water atomization (WA), which yields irregular particles that have better shape retention ability and lower cost [45,46]. It is known that powder characteristics, e.g. morphology and size, directly affect processing parameters in powder metallurgy technology such as injection molding [47–49] or in various additive manufacturing technology including selective laser melting [50,51] and binder jet printing [52]. Atomization leads to different shapes, sizes and morphologies of powder particles which affect powder properties and utilization. Porosity also varies due to differing atomization, this is important to quantify as it can be used to predict internal defects and final part quality [53]. Therefore, utilization of powders with similar characteristics between different batches are crucial.

2.2.3 Powder size distribution (PSD) and morphology

Powders produced from different atomization techniques will be inclined to vary in terms of their morphology, particle size and powder size distribution (see Figure 3A) which affects the packing density and flow properties of the feedstock. Generally, highly spherical particles are often desired in the powder bed AM processed since particle shapes that conform towards unity can gradually enhance both its powder packing density and rheology performance as shown in Figure 3B. While powder morphology reveals the visual structure of powder particles, the powder size distribution (PSD) is commonly used to quantify particle sizes in terms of volume composition. The powder size distribution is an important parameter in AM technology affecting flowability and deposition of the part to post processing via sintering. It also determines the packing fraction of the powders and consequently the binder saturation levels, the surface finish of the green and final part, and influences layer thickness. Various methods can be used to determine the powder size distribution such as optical or electron microscopies [43], laser microtrac particle size analyzer [54], sieving and micro-computed tomography technique [55]. Many commercial feedstocks used for the powder bed techniques follow a *Gaussian* distribution although the addition or removal of powder particles through mixing and sieving operations could substantially affect the behavior of the distribution curve resulting in other model variants as shown in Figure 3C.

In normal distributions (also known as *Gaussian*), the mode, mean and median coincides at a single central tendency of the curve; however, the negatively and positively skewed distributions are asymmetrical as a result of higher fractions in coarse and fine particles, respectively. Besides, it is possible to have multimodal distributions exhibiting two or more distinct peaks at discrete particle sizes which show the respective modes of the distribution. As shown in Figure 3D, PSD results are usually presented in a differential curve to distinguish the

mode, mean and median particle sizes of the feedstock and a cumulative graph which identifies the volume content in terms of size gauges (D_{10}, D_{50} and D_{90}) [56–58]. Typically, PSD influences packing behaviors which affect shrinkage and densification of forming parts in conventional sintering processes. While features on a size distribution curve provide qualitative indications of the overall powder behavior, various techniques such as sieving, laser diffraction and dynamic image analysis are required to characterize the volume of measured particle sizes through shape detection and size screening procedures. In a study by Mostafaei et al. [54], water and gas atomized alloy 625 powders were characterized with different techniques such as morphology, shape and size using optical microscopy, scanning electron microscopy, laser particle size analyzer, sieving, and micro-computed X-ray tomography (μCT) with different resolution and sample setup. Besides, powders porosity was studies by cross-sectional observation to determine internal porosity to understand the differences between conventional destructive techniques compared to μCT.

Spherical powder particles are preferred due to better flowability and lower friction than faceted or anisotropic powders [59]. Decost et al. developed computer vision and machine learning for autonomous characterization of AM powder feedstocks [60]. It was shown how feature detection and description algorithms were applied to create a microstructural scale image representation that could be used to cluster, compare, and analyze powder micrographs. Besides, the proposed approach was not limited to powder micrographs analysis and could be extended to new image data sets, including bulk microstructural images. Chen et al. [61] reported when the particle radius 'R' decreases over the range of R > 21.8 μm, the powder flowability is improved, which benefits the quality of powder bed; while, in the range of R < 21.8 μm, the effect of the Van der Waals' force rises and therefore dominates owing to the decreasing of particle radius worsening powder flowability and thus reducing the quality of layered powder bed.

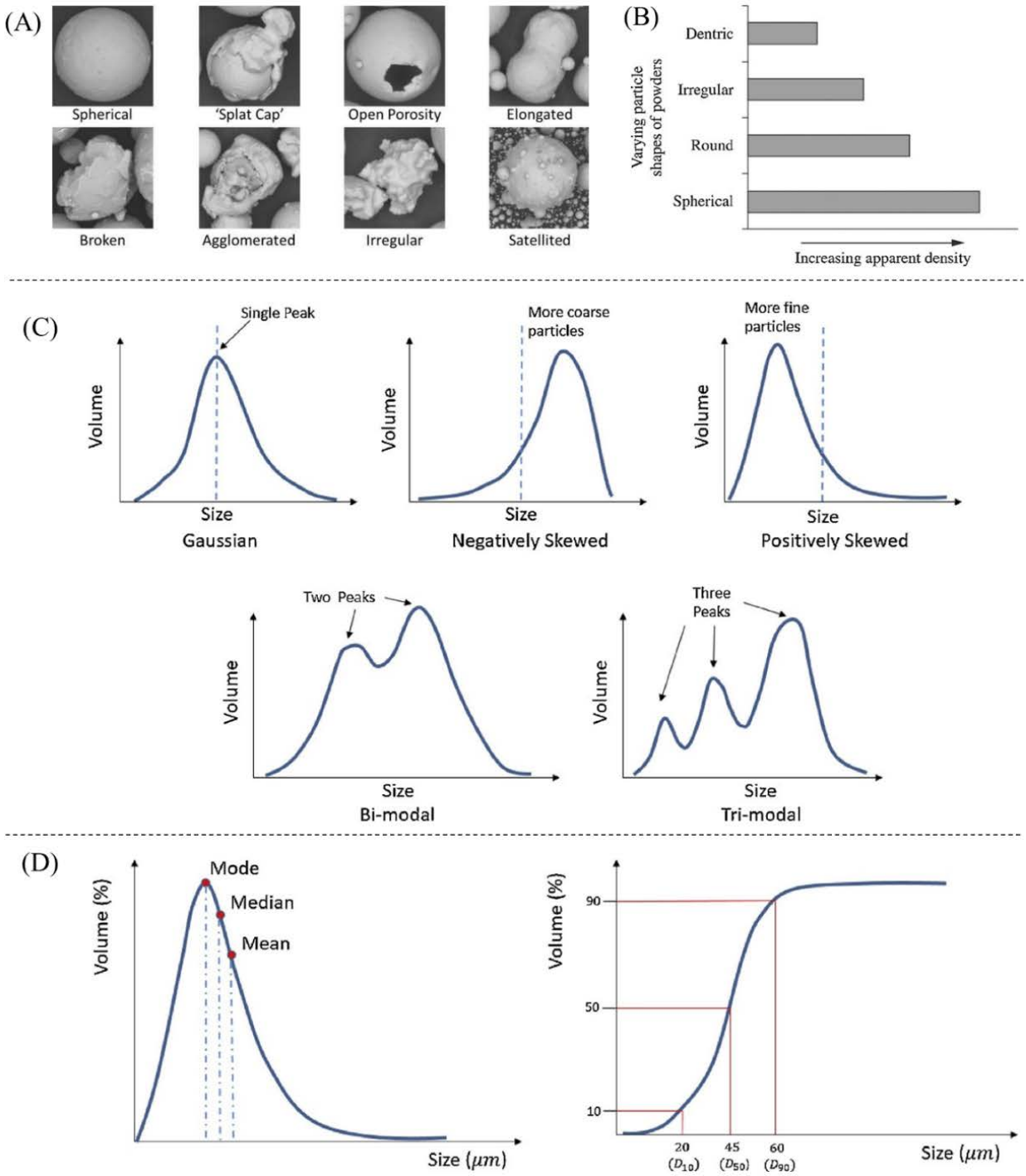

Figure 3. (A) Images of individual metal particles, produced using gas atomization, illustrate the many different shapes of particle that may result from the process, (B) effect of Powder morphology on apparent density, (C) variations of Powder Size Distribution and (D) differential (left) and Cumulative (right) Size Distribution [56].

Besides effects on powder flowability, powder size also has huge influences on the property of final parts. Lu et al. [38] used TiNiHf powder particles with four different SPD as shown in Figure 4a. They observed that large particles are preferred for binder jetting due to its excellent flowability and low surface area; while, fine powder is spread as slurry due to the high surface area and its nature to easily absorb moisture leading agglomeration and less powder flowability. Additionally, they found that the BJ3DP parts prepared using fine powder (<20 μm) had high mechanical strength (shown in Figure 4b) which can be explained by several aspects including (1) contact points between powder particles (even though smaller powder particles has lower packing rate, there are more contact points for a given cross section area), (2) the smaller powder particles (small radii) have a higher tendency to attract binder flow and therefore providing higher bonding strength at the contact points, (3) binder spreading process is different for different size (see Figure 4c) in which smaller powder size causes slower binder flow in the powder bed. In fact, different factors may result in differences in the binder spreading time and rate including (1) smaller powder particles cause higher capillary force for the binder to flow and spread, (2) smaller powder particles have lower powder packing rate (~35%) and therefore cause higher porosity in the powder bed for the binder to spread. However, it needs to be addressed that the surface area and frictional force between the binder and the particles affect binder spreading in which small pores and increased total surface area in small powder particle result in longer binder spreading time and lower binder spreading rate. Due to binder spreading process, the binder is not confined along the designed width line and lateral spreading is instantaneous. Thus, that inevitably increases the actual wire width.

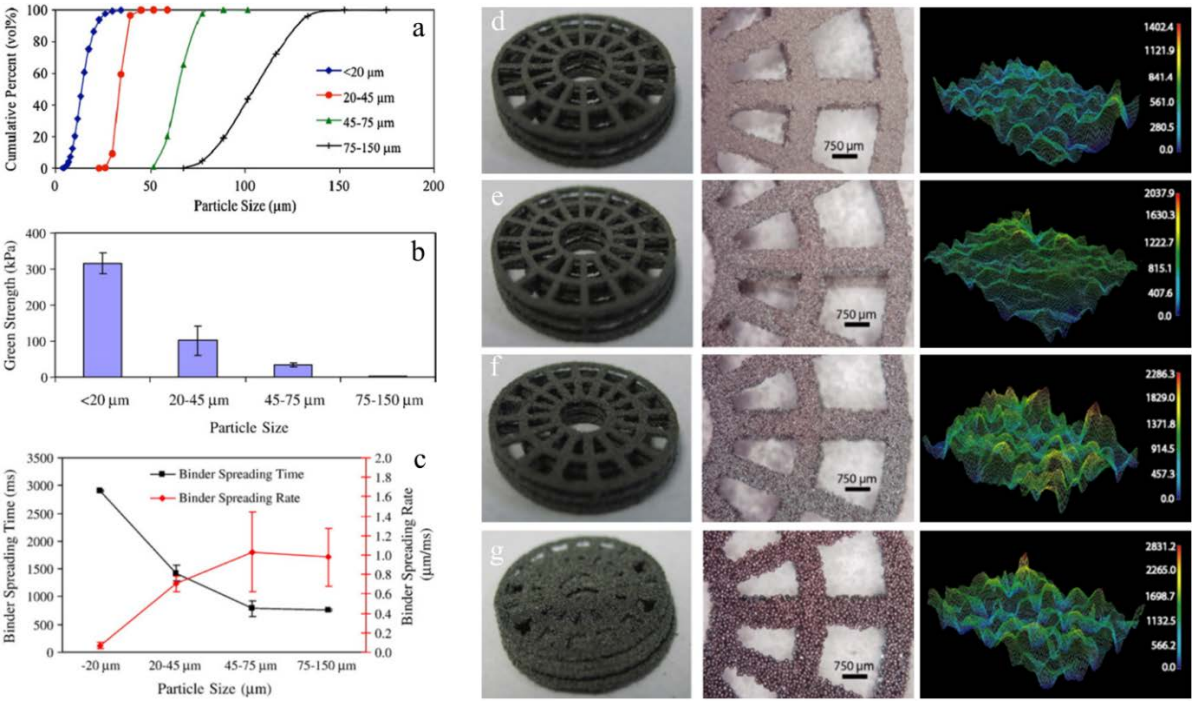

Figure 4. (a) Particle size distributions of four different TiNiHf powders, (b) green strength of 3D mesh structures from four different size particles, (c) . Mesh structure images for four different size TiNiHf powders are illustrated in (d) less than 20 μm, (e) 20–45 μm, (f) 45–75 μm, and (g) 75–150 μm. The left side image is 3D structure, the middle image is 2D mesh wire structure and the right side image is the surface 3D profiles for different powder size [38].

Thus, powder size, powder packing rate, and binder drop volume affect accuracy and tolerance of the BJ3DP part. Even though large powder particle has better flowability and packing rate compared to fine powder particles, the shape retention ability and surface finishing and roughness are undesirable (see Figure 4d-g). From a manufacturing point of view, a powder bed with rough surface will negatively affect the 3D printing resolution leading to dimensional inaccuracy of the printed component compared to the inputted CAD model. It is necessary to keep in mind that the fundamental motivation of developing rapid prototype techniques is to assist in the control and replication of a product.

In a study conducted by Hapgood et al. [62], it was found that changing the powder particle size may affect the pore size distribution within the powder bed and thus alter the drop penetration behavior of the water-based binder. Typically, as the powder bed is heterogeneously distributed (e.g. it may happen for water atomized powder or ball-milled powder with irregular powder morphology, see Figure 5), it takes a longer time for the binder droplet to completely penetrate. In addition, small powder particles may cause creation of many macro-voids within this powder bed due to the formation of fine powder agglomerates and consequently, the drop penetration time increases. As the macro-voids radius increases, a decrease in the surface curvature of the flow front occurs and fluid stops the liquid advancing into that macro-void. Therefore, liquid has to flow through neighboring micro-voids around the macro-void and eventually increases a longer drop penetration time as well as a void formation [62,63]. In contrast, the liquid has more paths to penetrate through a more homogeneously distributed bed (see Figure 5). Therefore, optimizing the powder size distribution as well as the binder selection can help to reduce number of issues related to the printing step.

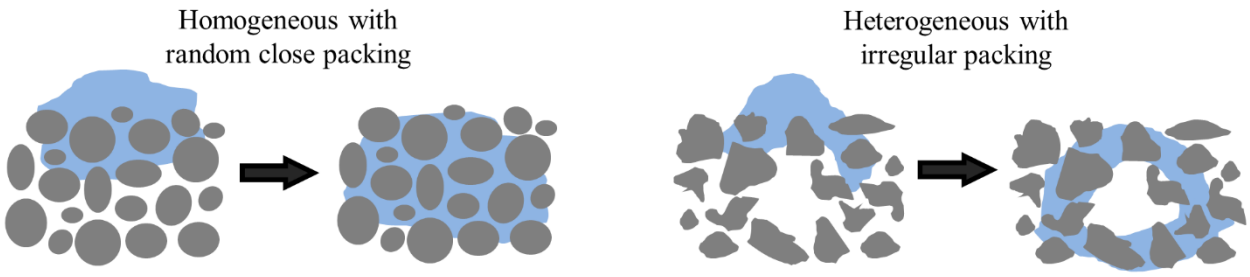

Figure 5. Schematic illustrating the proposed different droplet penetration behavior within (left) homogeneously distributed and (right) heterogeneously distributed powder beds. For close packing powders such as gas atomized powder with spherical powder morphology, the fluid drainage is relatively uninhibited. However, as liquid penetrates powders containing large macro-voids the liquid front will tend to cease when the pore radius increases suddenly. This happens whenever a capillary pore reaches a macro-void (The macro-void space does not contribute to the effective capillary volume or surface area) [62,63].

Depending on binder jet printer features and capabilities, size distribution may vary between 5 μm and 100 μm. Nevertheless, if powder size distribution ranges from 16-63 μm with the average particle size of 30-35 μm as the powder used here, green part density will be approximately 50% and will experience similar shrinkage, just at different sintering temperatures. Typically, finer powder particles (less than 20 μm) result in faster sintering kinetics and the shrinkage depends on the initial powder packing. If green density could be increased, e.g. using powder with a bimodal, trimodal size distribution, printed parts will experience lower shrinkage during sintering. In other words, by applying coarse and fine powder particles together in binder jetting, one may gain advantages from both large and small particles in which the flowability will be guaranteed by larger particles and small particles fill voids between large particles to increasing the packing density. However, the ratio of the fine powder to coarse powder needs to be optimized in case that the addition of fine powder decreases the flowability of the mixture, which will be deleterious to the powder packing. Based on McGeary [64], the maximum packing fraction of about 82% can be attained using bimodal powder size distributions with a ratio between the size of the coarser and finer powders of 10:1. In other study conducted by Zhou et al. [63] on effects of particle size on binder jetting of calcium sulfate/calcium phosphate scaffolds, it was found that the addition of fine calcium phosphate powder did not increase the bed packing density and the flowability was the predominant factor, leading to the formation of rougher surface and low packing density due to the addition of the fine binder. Compared to the base green density of ~50% in BJ3DP parts, it can be concluded that the higher the green density, the lower would be the resulting part shrinkage on final densification. As the powder particle size decreases below ~5 μm, safety of powder handling and respiratory will be main concerns and therefore is not recommended.

Miyanaji et al. [65] studied two types of powder (1) 420 SS powder with spherical particles and unimodal size distribution of 35 μm average particle diameter and (2) Ti-6Al-4V powder with bimodal size distribution of 6 μm and 32 μm average particle sizes (morphology and size distribution results are illustrated in Figure 6A). The packing density of the powders spread with the traverse rate of 2 mm/s was measured to be 55% and 66% for the 420 SS and Ti-6Al-4V, respectively. The surface area and contact angle measurement results were given in Figure 6B and it was seen that the surface area in the 420 SS powder was higher due to the presence of porosity in powder particles. The low contact angle values for both powder types corresponded to the increase of the capillary pressure levels under the equilibrium condition. Figure 6C illustrated the variation of saturation level vs. capillary pressure. It was reported that the in general smaller pore size corresponds to higher packing density, which in turn indicates higher capillary pressure of powder material [66]. Therefore, Ti-6Al-4V powders showing higher packing density had higher capillary pressure compared to that of 420 SS powder.

(A)

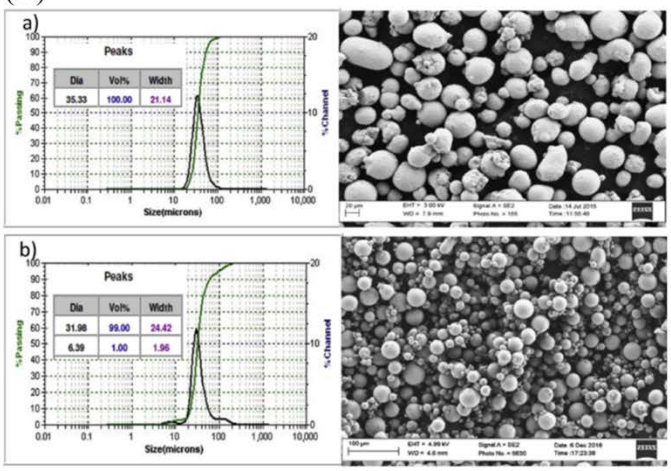

(B)

Sessile Drop Method and BET results.

Material	Contact angle (degree)	Specific Surface Area from BET (m)
420 SS	25°	2
Ti-6Al-4V	40°	0.75

(C)

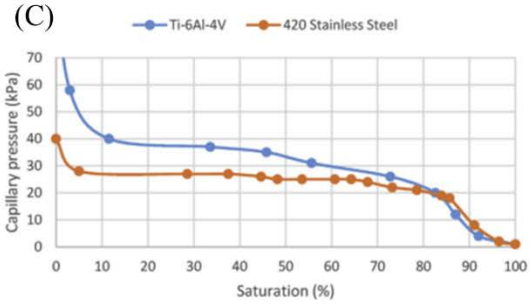

Figure 6. (A) Morphology and PSD analysis results of (a) 420 SS (b) Ti-6Al-4V powders. (B) Contact angle and specific surface area measurement results. (C) Capillary characteristic curves for 420 SS and Ti-6Al-4V [65].

2.2.4 Spread speed and print speed

Spread speed is an input parameter determining the speed of the counter-rotating roller to deposit the powder bed which varies between 0.1 mm/s and 4 mm/s. Depending on the printer type and spreading powder system, parameters such as recoat speed (mm/s), oscillator speed (rpm), roller speed (rpm), roller traverse speed (mm/s) can be different inputs that user needs to consider prior printing [52]. Speeds over 4 mm/s spread may result in a non-uniform powder bed resulting in layer delamination after printing multiple layers. Currently, the determination of the uniformity of powder bed has been determined based on the visual observation during printing process and may have variability. Since there is no qualitative model to determine spread speeds based on PSD and powder morphologies, users need to determine the spread speed by trial and error method and visual observations. In a study by Shrestha [67], experimental design was conducted on the spread speed between 6 mm/s and 14 mm/s and was found that 6 mm/s resulted in higher accuracy. If authors tested lower than 6 mm/s could have resulted in higher accuracy rather than 6 mm/s.

To develop reliable strategies for part production with optimized processing parameters, it is vital to have a quantitative understanding of the interaction and mechanical behavior of the powder particles during the application process. In a study by Parteli and Poschel [68], a particle-based numerical tool for the simulation of powder application is proposed to investigate the characteristics of the powder layer deposited on to the part using a roller as the coating system. In this study, the complex geometric shapes of the powder particles were taken explicitly into account in which irregular powder particles and non-spherical powders are considered as an important parameter during simulation (Figure 7A). In binder jetting system, roller roatates in the counter-clockwise direction as shown in Figure 7B. It was shown that increasing the coating speed (with translational velocity V_R between 20 mm/s and 180 mm/s) led to an increase in the surface

roughness of the powder bed affecting part quality (Figure 7E). Besides, it was found that powders with broader size distribution may increase surface roughness while small powder particles are prone to agglomerate leading to an increase in the packing's porosity. More importantly, the applied load during the coating process may vary over an order of magnitude and therefore causing an inhomogeneity of interparticle forces in the granular packing. It was shown in Figure 7C that the evolution of the magnitude of the components of the total force on the part in the horizontal and vertical directions (F_x and F_z, respectively), as a function of time. As the roller passes the print area (green part), an inhomogeneous force appears due to the interaction among neighboring powder particles. Hence, it is essential to perceive how the process dynamics influence the packing behavior of the powder bed during bender jet printing. The main benefit of the proposed numerical method in [68] is to assist investigations of the flowability and packing behavior of different powder systems as a function of material and process parameters, as results were shown in Figure 7. Thus, it is possible to attain powder layer characteristics not only by altering process parameters like the roller's speed but also by changing the PSD of the applied powder. It is worth noting that the powder spreading method (e.g. mechanical vibration and rolling), powder geometry, powder surface texture and the roller’s surface texture affect the porosity and surface roughness of the deposited powder layer. Additionally, size segregation or compaction in the powder bed might be influenced by the powder spreading system.

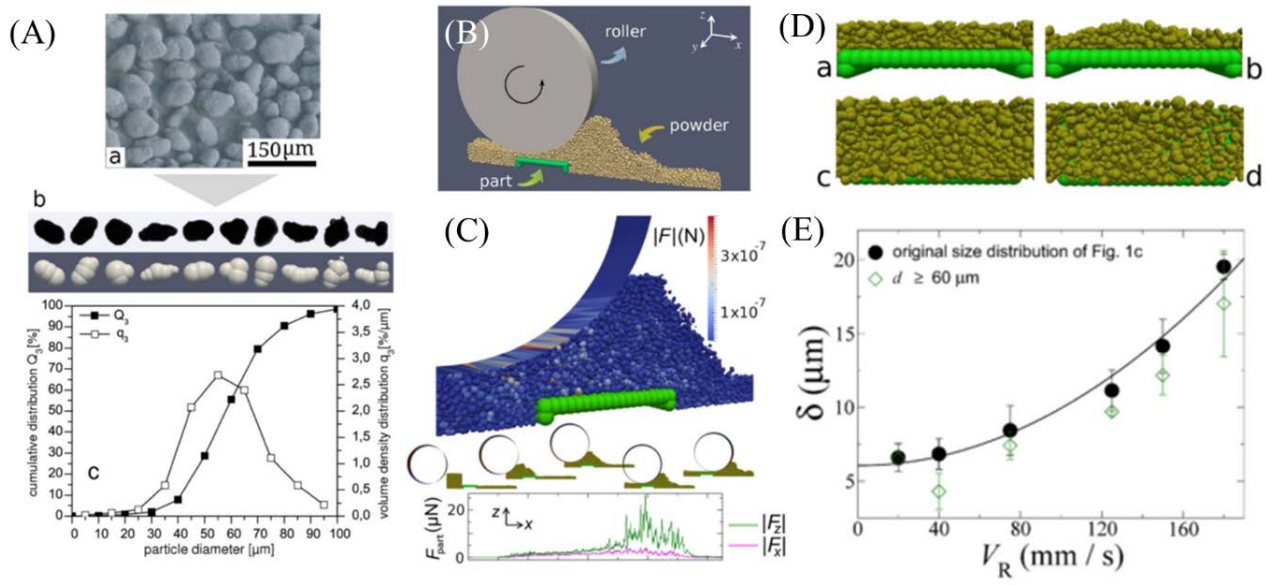

Figure 7. (A) a: Powder particles with complex geometric shapes, b: light microscope images of some of the powder particles (first row) and corresponding particle models using the multisphere method (second row), c: cumulative and volume density distribution dada, (B) schematic overview of the main element for the simulation, (C) Schematice of the powder roller interaction during printing process, (D) powder layer applied onto the part to be built with various roller speed of 20 mm/s (left) and 180 mm/s (right), and (E) dependence of the surface roughness 'δ' on the coating velocity, 'V_R'. Detailed information can be found in [68].

The influence of the printing speed on quality and integrity of the printed components was experimentally evaluated on the 420 Stainless powder (Figure 8A). Two different variants were studies including printing direction and track size (Figure 8B-C). It is reported by Miyanaji et al. [69] that increasing printing speed led to the reduction of the accuracy of the fabricated parts regardless of the printing orientation in the powder bed that can be attributed to the enhanced inertia forces. Generally, the accuracy of parts printed in x-direction was different from the y-oriented samples associated to the asymmetrical spreading of the droplets favored toward the printing direction (see Figure 8D). This concept might be due to the horizontal velocity of droplets. As illustrated in Figure 8E, as the printing speed increases, splashing phenomenon might happen

during binder deposition through printhead resulted in the loss of the slot features in the x-oriented printed parts and the reduced accuracy in the y-oriented features. The effect of printing speed on dimensional accuracy of single-track, multi-track, and cubic features are depicted in Figure 8F-G, respectively. Basically, the effect of printing speed on accuracy in y-direction (printing direction) was greater than that of x-direction (perpendicular to Y direction). A linear correlation was seen between the printing speed and dimensional accuracy of printed features in y-direction indicative of accuracy prediction based on the selected processing parameters is passible. It is vital to note that the obtained results in [69] were highly dependent on the powder feedstock characteristics and the liquid binder properties, as they significantly control physics of the interaction between liquid binder and powder upon impact and permeation. Another aspect of printing speed is its influence on the variation of equilibrium saturation. It was shown in [69] that higher printing speed resulted in the increased volume of the printed samples. In fact, as the nominal binder amount during printing process remained constant, the increased volume resulted in lower equilibrium saturation that may deteriorate the mechanical strength of the printed part [69,70].

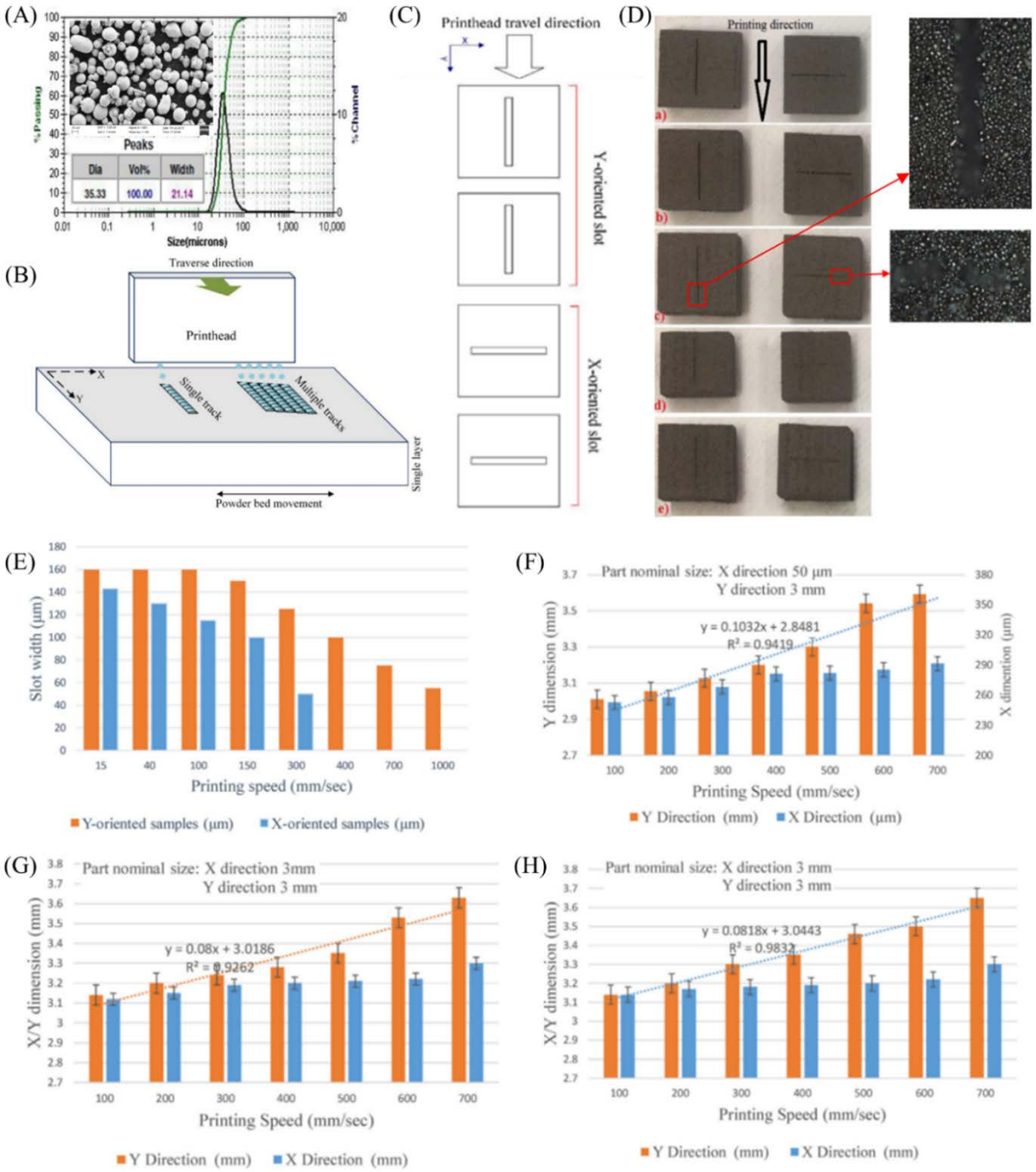

Figure 8. (A) Powder size distribution and morphology. (B, C) The designed geometry for printing samples and part configuration in the powder bed, schematic of single track and multiple tracks experiments are shown. (D) Printed features with different printing speeds (a) 20 mm/sec (b) 100 mm/sec (c) 300 mm/sec (d) 700 mm/sec (e) 1000 mm/sec. (E) Variation of the slot accuracy with printing speed and part orientation. (F) Effect of printing speed on dimensional accuracy of single-track samples. (G) Dimensional accuracy of multiple-track samples fabricated at various printing speeds. (H) Printing speed effect on accuracy of cubic parts [69].

2.2.5 Layer thickness and powder packing density

Layer thickness is determined by the PSD varying between 20-300 μm. Generally, the layer thickness should be larger than the diameter of the largest particle powder feedstock. To overcome the issues of low powder bed density and high surface roughness, fine powders within the size range of 15 μm to 150 μm are often employed. Although smaller powder particles can enhance particle packing and reduces surface roughness of the AM part, agglomeration tendency might be a constraint in using fine powder particles [71–73]. The particle size determines the layer minimum thickness as well as the minimal size of the part features that can be built using AM techniques. In case that the layer thickness is greater than the maximum particle size, then all the powder particles regardless of the powder particle size will be deposited/dispensed into the build volume. In other words, if a layer thickness is smaller than the maximum particle size, a preferential deposition of a finer distribution of powder particles will happen [42,74]. In binder jetting, the deposited layers were bonded together using a binder where their strength is still low; therefore, the wiper or roller should not apply force on the large powder particles affecting the previously printed parts. More importantly, increasing of the layer thickness may lead to the reduction in the density of each powder bed layer. The desired layer thickness defines as a limit to the maximum powder particle size. The optimum layer thickness of 100 μm is suggested [67] for the PSD of 16-53 μm with mean of 35 μm [33]. Powder bed density is another important aspect in the case of binder jetting in which sintering is carried out as one of the steps to achieve full densification. Shrinkage happens during densification depending upon the powder bed density. Thus, it is necessary to understand the role of powder feedstock (e.g. morphology and size distribution) on controlling the powder bed density. Figure 9 illustrates the effect of layer thickness on the powder bed density. Generally, the powder bed density directly affects the green part density where a higher green density ensures

reduced shrinkage during densification step. As an example, a compact powder bed with a green density of 40% would shrink by 60% (which is the pores volume fraction) during full densification. On the other hand, an increase in green density to 70% will result in about 30% shrinkage [75]. With the same powder size distribution, gas atomized powder with spherical powder shape has higher green density compared to the water atomized powder with irregular powder shape [33].

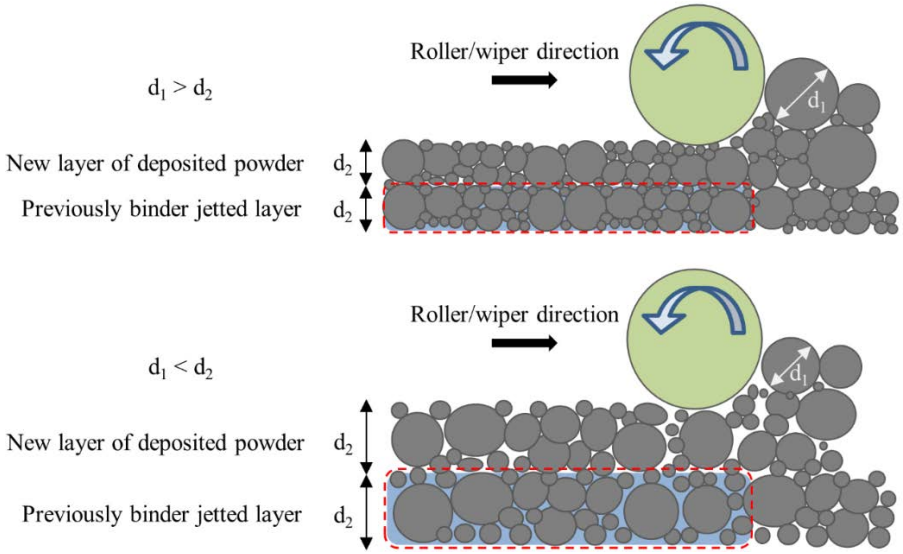

Figure 9. A comparison between powder particle size and two layer thicknesses affecting powder bed density.

Powder packing density is an essential parameter to determine how efficient powder particles are able to arrange themselves with maximum particle-to-particle contact and minimum voids within the granular network. As explained earlier, several key factors affect particle packing behavior including morphology, PSD, inter-particle forces, surface chemistry as well as flowability [76]. Figure 10 shows how the packing density may reach a maximum as the PSD includes both fine and coarse particles. In general, actual powders do not reflect the close-packed behavior of uniform and equivalent-sized spheres found in cubic and/or hexagonal-close-packed

systems. In fact, they are loosely arranged in a poly-dispersed manner with a mixture of random particle sizes as well as an arbitrary order of interstitial pore distribution, leading to relative packing densities of ~60–70%. In this figure, f_s and f_l denote the packing density of the small and large powder particles. It is necessary to point out that the packing density during binder jetting is lower since there is limited compaction during 3D printing process where the green density of ~40-60% can be achieved. Powders with a wide PSD and adequate amounts of fine particles present in its distribution array are inclined to display high packing densities. One approach to enhance a high powder packing density is adding fine particles of discrete diameters and generate a multimodal size distribution with secondary or tertiary peaks. To determine the size ratio between coarse and fine particles, the existing void size and morphology of the base powder need to be taken into account. The quantity of fine particles depends on apparent densities of the respective powders. An effective packing density improvement was reported at a coarse to fine size ratio of 1:7 where fine particles can percolate through triangular pores in the coarse matrix [56,77]. Karapatis et al. [78] adopted the bimodal approach by to improve the packing density of direct metal laser sintered nickel powders by using a coarse to fine size ratio of 10:1 and powder layer density was reported to increase from 53% to 63% following the addition of 30% fine particles. In another study, Zhu et al. [79] reported that the apparent density of copper alloy powder was enhanced from ~77% to ~88% when the amount of fine binder particles increased by 10%. Generally, addition of fine particles may be influential in modifying powder packing density which could either skew a Gaussian distribution or generate a multimodal distribution wherein both approaches result in the extension of size distribution widths. Moreover, the multimodal approach may offer a more straightforward solution to improve packing behavior as void sizes are typically predetermined as compared to a random distribution of unknown voids [56].

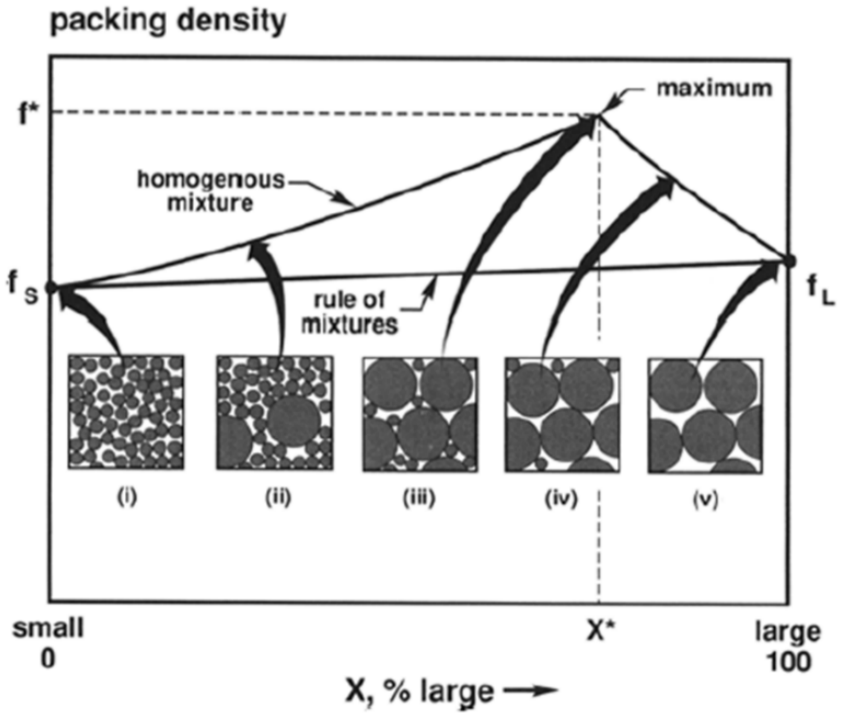

Figure 10. A schematic showing the effect of powder particle size and distribution on packing density for a bimodal mixture, showing five possible structures. The maximum density for a homogeneous mixture f* occurs at a certain mixture, which is far above the rule of mixtures density [80].

Thus, addition of fine particles can be influential in modifying powder packing density in terms of (1) skewing a Gaussian distribution or (2) generating a multimodal distribution; wherein both approaches result in the extension of size distribution widths (see Figure 3C). It was thought that the multimodal approach may offer a more straightforward solution to enhance the packing behavior as void sizes are typically predetermined as compared to a random distribution of unknown voids. Generally, AM metal powders are necessarily fine to meet the requirement to form a powder bed just tens of microns thick. On the other hand, fine powders can be problematic in terms of flowability. As the particle size decreases, the forces of attraction between particles increase and therefore finer powders are usually less free-flowing than coarser analogues. It is worth noting although blending of fine particles with coarse powder may provide beneficial effects

towards enhancing powder packing density, the incorporation of fine particles might introduce certain downsides on flowability due to increased powder cohesion and inter-particle forces. In a study by Schade et al. [81], it was displayed that the powder flow and particle size have an inverse relationship as shown in Figure 11. Powder flowability becomes more restricted with decreasing particle size. The resulting agglomeration effects is also detrimental to powder apparent density since the fine particles have higher tendency to adhere with each other, forming irregularly shaped powder clusters instead of filling up the inter-particle voids within the coarse matrix.

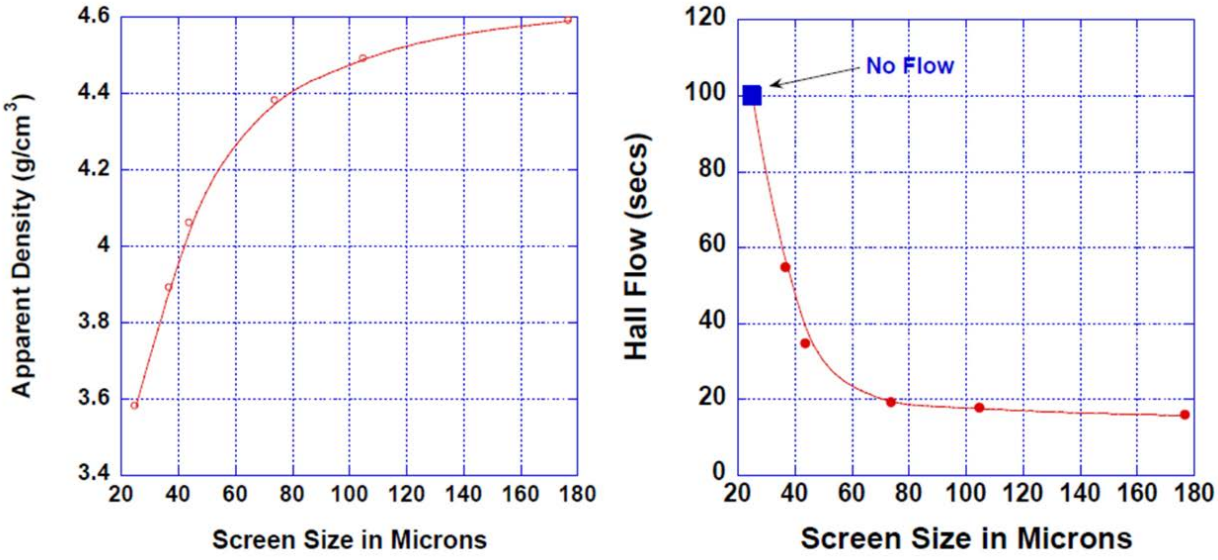

Figure 11. Apparent density and Hall flow of gas atomized iron powder as a function of the particle size [81].

Cao et al. [41] investigated the double-smoothing (DS) mechanism on ultra-thin powder layering in 3D printing process. Generally, it is known that thinner powder layers are beneficial to the 3DP parts to attain high accuracy, surface quality and densification. In the case of counter-rolling (CR) layering as a conventional layering method, it is quite impossible to achieve ultra-thin

layering due to the considerable layering defects such as the cavity defect and part-shifting defect or complicated expensive processes are required. For the first time, Lee [82] used a DS layering method to spread each layer as shown in Figure 12Aa. Double-smoothing is not commercialized in the 3DP machines and Cao et al. [41] developed a printer for this purpose with details shown in Figure 12Ab and Figure 12B. It was illustrated that with the roller excited to vibrate, the powder bed obtained the relative densities of 49.5 ± 4.3% after 120 rounds of CR layering with 100 μm layer thickness, whereas the relative densities were only 45.1 ± 3.7% without the vibration (please see detailed information in [41]). The experimental setup in the layering tests for dispensing tri-modal powder material system to print ultra-thin powder layers was displayed in Figure 12C. Two observing windows including window I (dry area) and window II (wet-area) were defined to study the part shifting. Analysis for the cavity-type layering defects revealed that the resulting cavities in the wet-areas always appeared more than those in the dry areas (Figure 12D). One possible reason for the formation of cavity might be referred to the residual moisture in the previously printed areas leading to the capillary bridge forces between the powder particles to increase the internal frictions lowering powder spreadability/flowability and increasing the shear stresses applied to the powder particles. Thus, the wet-area results play a significant role to determine the feasibilities of the layering parameters in the viewpoint of restricting cavities. It was found that the CR layering method was not appropriate for the ultra-thin layering of 55 μm, the DS method is suitable for dispensing the 55 μm ultra-thin powder layers. Analysis for the layering defects of part shifting was illustrated in Figure 12E and the similar trends was seen to those of cavity defects in wet-areas.

Analysis for the densification proved (see Figure 12F) that the DS layering was capable of producing denser green specimens and powder bed than the CR method in which the maximum green and relative densities of 69.9 ± 1.7% and 70.2 ± 1.5%, respectively using DS layering, and 31.9 ± 6.1% and 43.7 ± 5.3%, respectively using CR layering were achieved. Uniformity analysis results for printed specimens were shown in Figure 12G and it was found that the deeper powder is always less likely to experience the great densification. As shown in Figure 12G, three specimens with 41.7%, 55.5% and 63.8% bulk green densities were prepared from three different layering test groups and demonstrated several noticeable drops of localized green densities along their length direction; while the specimen with 70.1% green density was achieved from the DS layering test group resulting in much fewer cavities than above three, exhibited very good uniformity in localized green densities. It is worth noting that each printed powder layer is compressible, thus the powder at different positions along the specimens' height can experience different times of additional compressions. Therefore, another uniformity analysis can be considered along the specimens' height. Figure 12H displayed how localized green densities varied where the largest densities were at the bottom position and continuously decreased from the bottom to the top. It was shown that differences of localized densities between the bot- tom and top were about 1.8% for the specimen with 69.9% bulk density from the DS layering test group compared to the maximum 9.4% for the specimen with 42.1% bulk density from the CR layering test group. Based on the theoretical framework on layering issues supported by experimental results [41], it is expected that the future 3DP machines consider it for research and development aspects.

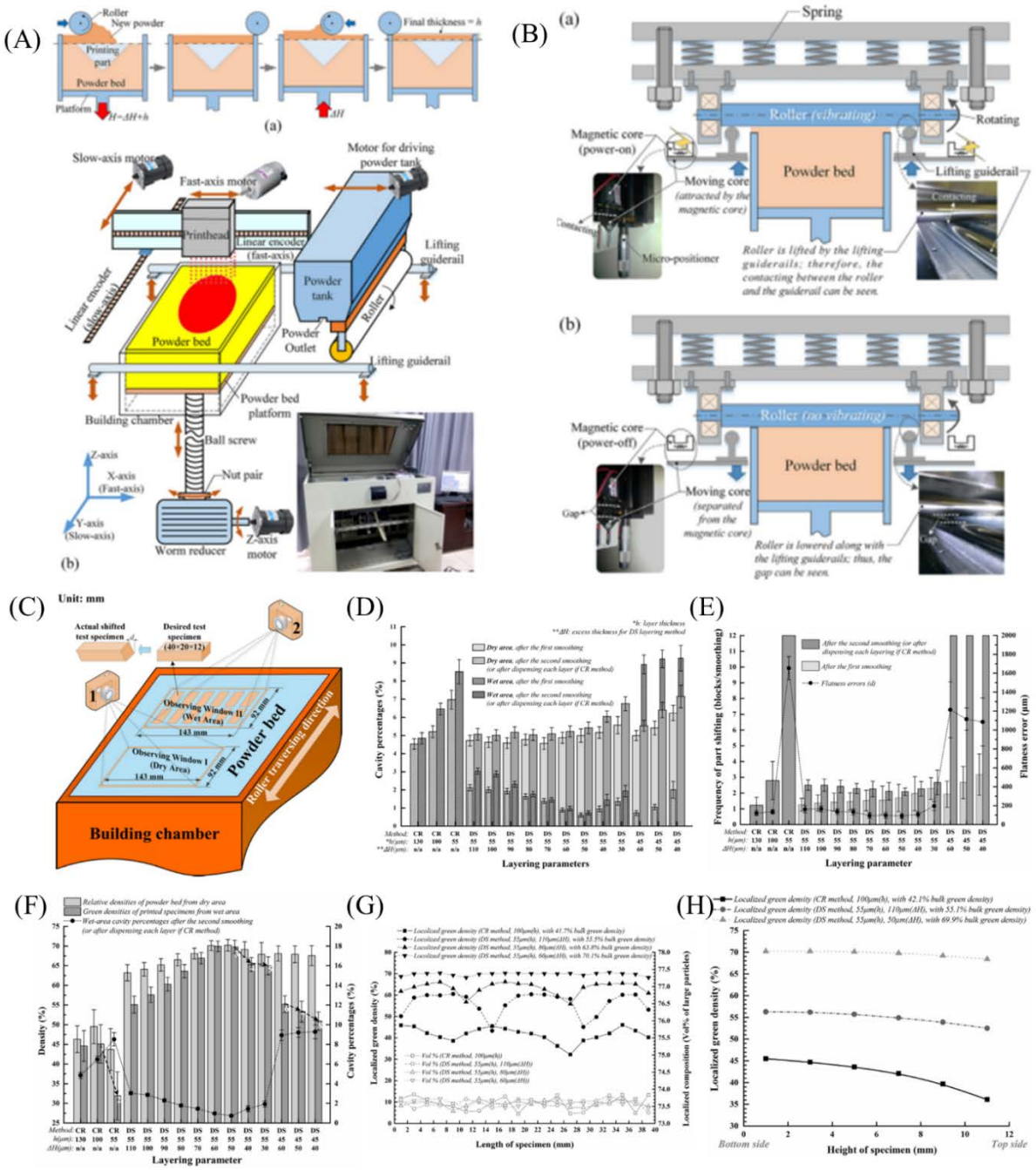

Figure 12. (A) ‘a’ DS-layering steps for dispensing each powder layer; ‘b’ setups of the self-developed 3DP machine, (B) working principles of the powder-layering apparatus: ‘a’ apparatus move- ments for the first smoothing; ‘b’ apparatus movements for the second smoothing, (C) experimental setup in the layering tests, (D) cavity proportion observed in the powder-layering tests, (E) results of part shifting and flat errors measured on the printed specimens, (F) powder densification results measured in the powder-layering tests, (G) results of uniformity analysis along specimens’ length , and (H) results of uniformity analysis along specimens’ height.

2.2.6 Binder selection

Generally, there are two types of binders including (1) organic in which binder binds the powder through the curing process and (2) inorganic where binder binds via colloid gel formation. In another classification, binders can be ordered as (1) acid-base binder that binder controls the powder bonding through acid-base reaction, (2) metal salts binder that forms the bonding with powder by salt recrystallization, reduction of salt crystallization or salt displacement reaction, and (3) aqueous based binder (solvent- or water-based) which is specialized for polymeric powders and creates designed structure after solvent evaporation (See [10] for more information).

Furthermore, depending on the binding mechanisms, binders can be classified as (1) in-bed binders which mixes with the powder in the bed and binds with powder through the jetting liquid from the nozzle (e.g. plasters and cement [83,84]), (2) phase-changing binders that works by solidification of binder to hold the powder together (e.g. 2-Methylpropane-2-OL [85]), and (3) sintering inhibition binders that controls the sintering area via selectively jetting heat-isolating materials, chemical oxidizers, sintering inhibitors and heat-reflective materials [86].

The viscosity of the used binder is important for being used in BJ3DP. The Ohnesorge number (Oh) is a dimensionless number that relates the viscous forces to inertial and surface tension forces between binder and powder surface. Binders with $0.1 < Oh < 1$ can be used for binder jet printing [87]. The used binder during printing process should not be corrosive towards the print nozzles. Two types of binder are currently used in BJ3DP of materials including diethyl glycol (DEG) binder or phenol based binders. DEG binders require curing at 200 °C whereas phenol based binders cure upon contacting with the powder bed.

2.2.7 Binder saturation

Powder packing factor and wettability are two main factors affecting the choice of binder saturation and the required volume of binder. Improper binder saturation can cause inhomogeneous powder bed. Layer delamination may be caused by low binder saturation levels, while higher binder saturation levels lead to excess wetting of the bed causing powder particles stick to the roller. The same as the spread speed, binder saturation is determined by the operator based on the powder bed behavior per visual examination. Theoretical binder saturation (binder saturation [%]) was calculated using the following equation:

$$S = \frac{1000 \times V}{\left(1-\left(\frac{PR}{100}\right)\right) \times X \times Y \times Z} \qquad (2\text{-}1)$$

where V is volume of binder per drop [pL], PR is packing rate [%], X and Y are spacing between binder droplets [μm] and Z is layer thickness [μm]. In order to attain a green part with sufficient mechanical strength and surface quality, optimization in the saturation level is crucial. Thus, the optimal binder saturation level is selected based on the packing rate and wettability. Figure 13 showed surface defects due to improper binder saturation level.

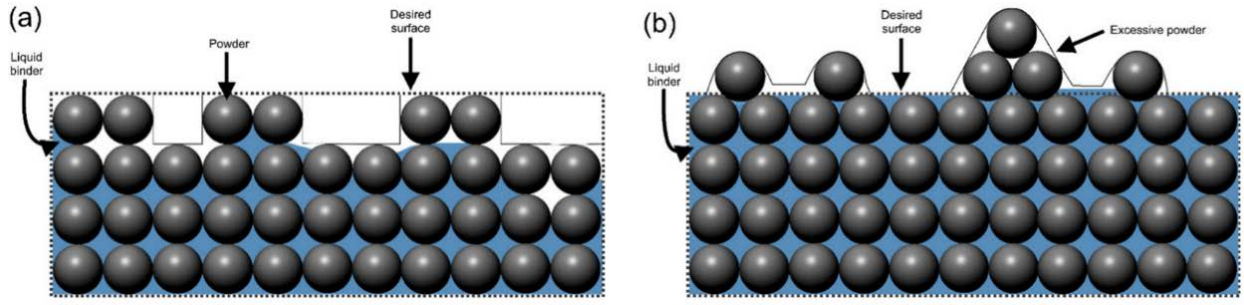

Figure 13. Possible surface defect formation due to improper saturation level; (a) low-level saturation leads to powder loss, and (b) over-saturation leads to excessive powder bond [88,89].

As illustrated in Figure 13a, low binder saturation level can lead to inaccurate geometry and low sintered density leaving porosity after binder burn-out step. In contract, over-saturation can cause the excessive powder bonded to the surface and makes some swells leading to the surface roughness as shown in Figure 13b. Another possible issue related to the over-saturation can be pointed out to the unwanted wetting of the bed sticking powders to the roller and subsequent inhomogeneous powder bed (if higher saturation level is needed, increasing drying time may help to dry the bed).

Lu et al. [90] found that the powder-binder wetting ratio is significantly influenced by the powder packing shown in Figure 14. Typically, the wetting ratio is higher for a densely packed powder bed compared to the same powder bed with loosely packed powder bed. During printing process, binder is jetted from the printhead with a certain drop size. However, the total amount of the jetted binder per layer is proportional to the total volume of the printed powder (here we can say thickness). As the binder reaches the powder bed, it spreads into the interstitial sites of the powder particle in both vertical and lateral directions. Shrestha et al. [67] found that the saturation level of 70% is an optimum binder saturation level when the layer thickness, roll speed and feed to powder ratio values are 100 μm, 6 mm/s and 3, respectively.

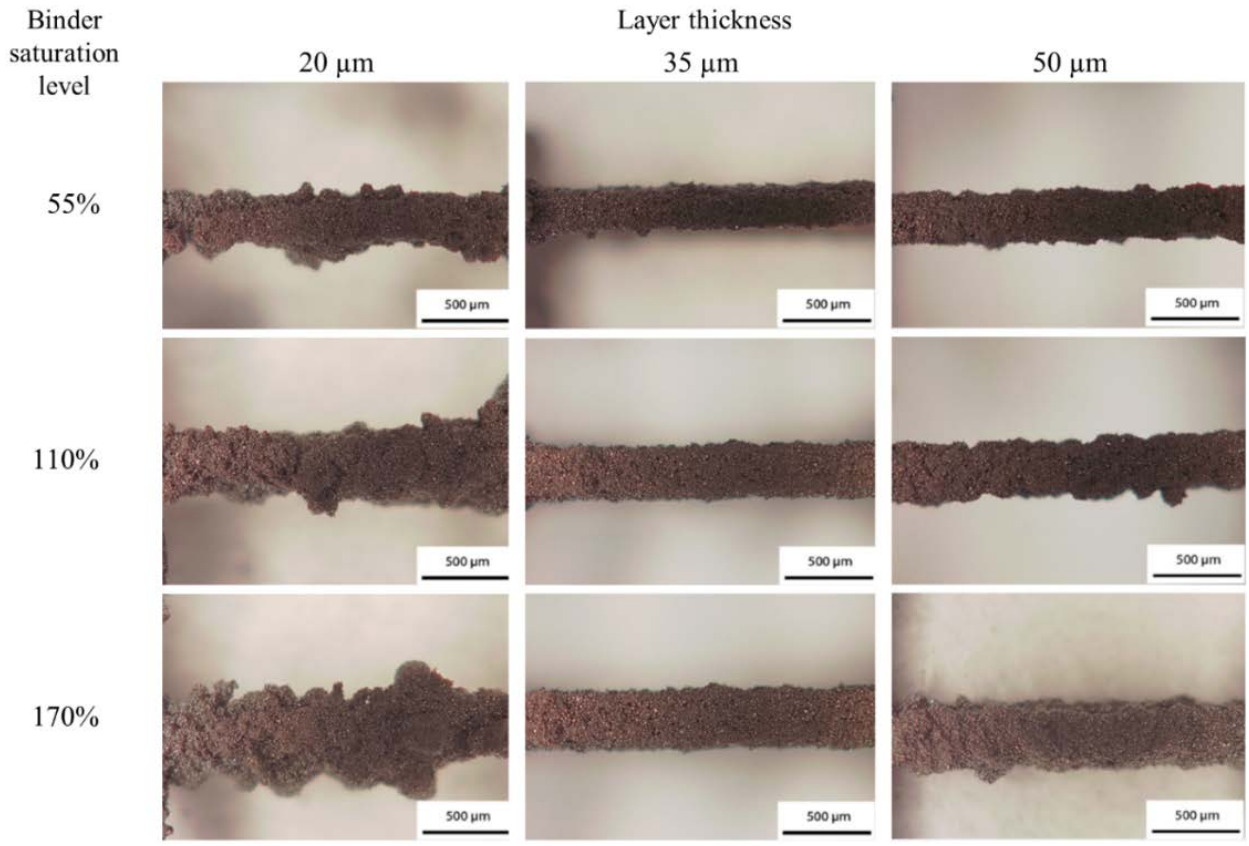

Figure 14. Optical micrographs of 3D printed TiNiHf square wire from powders with particle size distribution less than 20 μm and mean particle size of ~5.50 µm. Effects of saturation lever and layer thickness are compared [90].

As shown in Figure 15, if the powder layer is too thin and the layer thickness is less than the desired powder thickness to accommodate the binder at the applied saturation levels, it is possible that the extra binder spreads from the sides. This issue may cause excessive lateral flow of the binder and thus a larger and uneven printed part (examples were shown Figure 14). If the printed layer is too thickness, uneven lateral spreading becomes less. It may happen that the jetted binder is enough while the binder might have less than sufficient time to diffuse vertically to the previously printed layer. In this case, the same issue of uneven surface may happen. At the optimal printing layer thickness, binder spreading proceeds into vertical and lateral directions in which

there is enough binder to fill out interstitial site. Therefore, the actual binder spreading process requires in-situ observation, an ideal powder-binder should have a rapid spreading rate, appropriate vertical spreading distance and a relatively high wetting ratio.

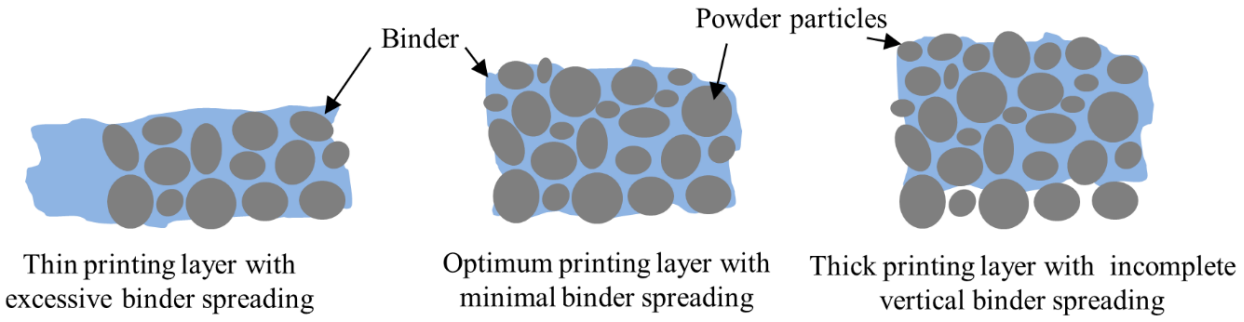

Figure 15. Different printing layer thickness and binder spreading.

In another study by Vaezi et al. [39], the effect of two parameters of layer thickness and binder saturation level on mechanical strength, integrity, surface quality, and dimensional accuracy in the 3D printing process were investigated as results were shown in Figure 16. A plaster-based ZP102 powder and water-based Zb56 binder were binder jetted using a ZCorp.'s Z510/Cx 3D printer apparatus. Two printing layer thicknesses of 0.1 mm and 0.087 mm are evaluated at binder saturation levels of 90% and 125% and then parts were infiltrated using a resin. It was found that under the same layer thickness, increasing of binder saturation level from 90% to 125% resulted in an enhancement of tensile and flexural strengths of the BJ3DP specimens while the dimensional accuracy and surface uniformity might be decreased. Generally, an increase of layer thickness leads to a better powder spreading; while under the same binder saturation level, the number of layers would be increased as the layer thickness decreases, therefore, the integrity is expected to

be higher increasing the tensile strength of the specimens. Additionally, under the same binder saturation level, the flexural strength may decrease due to better binder penetration in vertical and lateral directions over the surface, thus, there might be lesser unoccupied space between powder particles leading to lower porosity. Besides, under the same binder saturation conditions, tensile strength may not increase with a decreased layer thickness; however, a decreased layer thickness to certain limits may increase the materials tensile strength. In general, binder spreading distance in vertical direction is less than lateral direction, thus for the case the layer thickness is selected less than a certain limit, the binder completely penetrates vertically, and consequently the powder is saturated while the binder penetration would be incomplete in lateral direction decreasing sample's integrity and tensile strength. In other words, under the same binder saturation conditions, an increase in layer thickness from 0.087 mm to 0.1 mm showed a decrease in the tensile strength and increase flexural strength with a better uniformity on the surface.

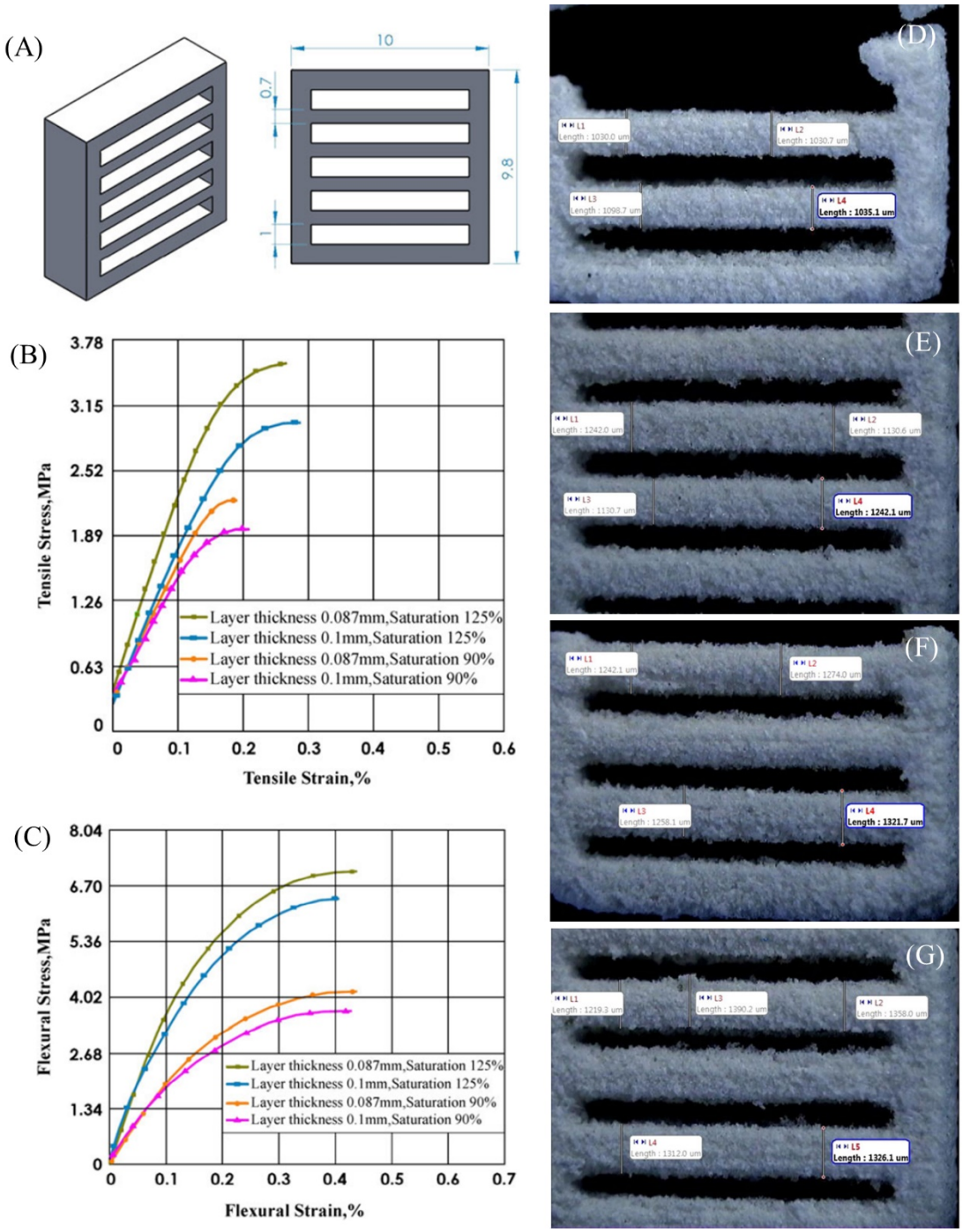

Figure 16. (A) Designed 3D network structure, (B) diagram of tensile stress–strain for uninfiltrated ZP102 powder, (C) diagram of flexural stress–strain for uninfiltrated ZP102 powder. Stereomicroscope images of specimens with (D) 0.1 mm layer thickness and 90% saturation, (E) 0.087 mm layer thickness and 90% saturation, (F) 0.1 mm layer thickness and 125% saturation, (G) 0.087 mm layer thickness and 125% saturation [39].

2.2.8 Drying time

After each time of spraying binder on the powder, the powder bed is subjected to a resistive heater for initial curing and this time is known as drying time. Depends on the choice of binder chemistry and composition, drying time may vary i.e. phenolic binders do not need drying time while DEG binders have a dry time of ~30 s/layer. Additionally, longer drying time (t_d) is required for higher binder saturation (S), larger surface area (A) and powders with poor thermal conductivity (k). Figure 17 illustrated two example of optimum and insufficient drying time. As illustrated in Figure 17a, as the liquid binder in the previously generated layers underneath the layer being printed is sufficiently dried, the penetration of the binder within the layer in the vertical direction is restricted by the layers beneath it, which causes enhanced saturation in the printed areas as well as more significant binder spreading toward the unsaturated area between the deposited droplets. Thus, parts with required dimension can be attained. In the situation that the drying time is not enough (see Figure 17b), then penetration rate of the liquid binder within the powder bed appears to be greater than the spreading rate. Thus, as the in-process heating parameter as drying time is not optimally chosen to sufficiently dry the binder, the deposited liquid binder in the top layer ends up supplying excessive binder to the underneath layers. Additionally, the residual binder will penetrate into the previous layers under the external pressure due to the weight accumulation of the printed structures leading to a decrease in the dimensional accuracy of the printed features.

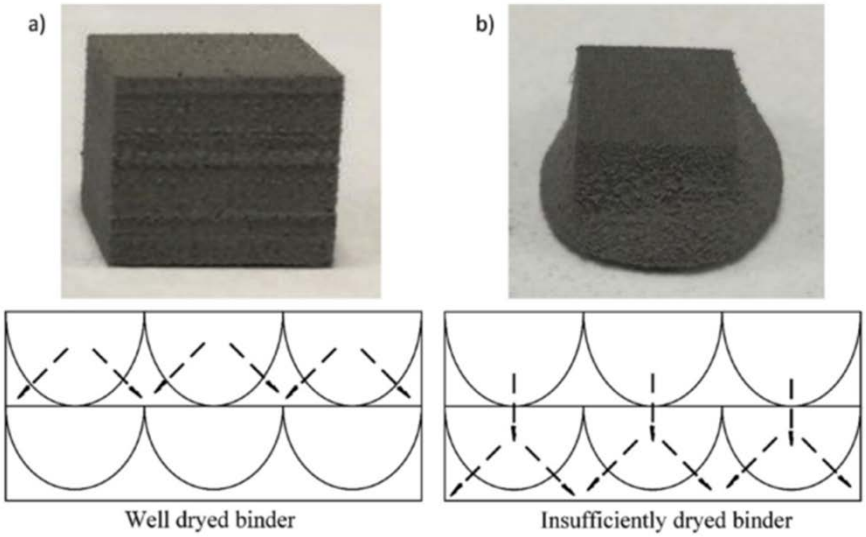

Figure 17. Schematic of parts printed with different in-process binder curing parameters (a) insufficient drying parameters (b) appropriate drying parameters (the dashed arrows indicate the potential binder migration paths inside the powder bed) [65].

2.2.9 Binder burnout, densification and shrinkage

In the case of using water and/or solvent based binders during BJ3DP technique, a glycerol based binder is the main component, which mainly occupies the interstitial spaces among the powder particles to hold the powder together in the desired shape. When the cured green parts are ready for densification, the post-processing step is subjecting BJ3DP components to a binder burnout process. Typically, burnout step happens prior sintering or infiltration process in the same furnace. To determine the binder burnout temperature, differential thermal analysis (DTA) can be conducted on the used binder. Generally, finer powder particles are processed using higher binder saturation levels. In the binder jetting, carbon content may vary due to the carbon rich residue after binder burnout and therefore the microstructure and phase formation would be affected. During

sintering step, Binder jetted parts experience shrinkage to remove part porosity caused during printing. Examples of CAD model, green parts and then sintered are shown in Figure 18.

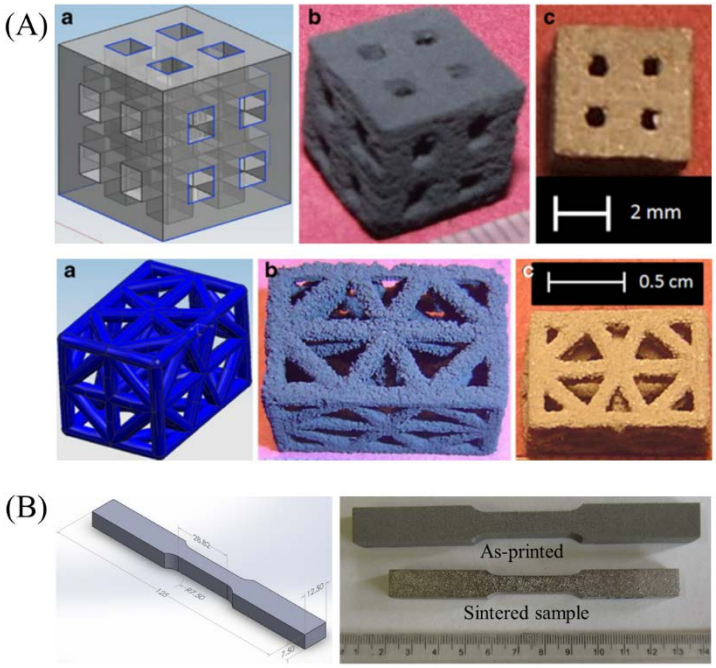

Figure 18. (A) Cellular material sample in its various representations during the manufacturing process chain: (a) CAD model, (b) green part, and (c) part after sintering [91]. (B) CAD model, green part and sintered sample with dogbone shape [52].

Infiltration is a route of densification using a low melting point material such as bronze to remove residual porosity and obtain full density with negligible dimensional changes. In fact, capillarity force between infiltrant material and pores on the powder particle surface is the main driving force of the infiltration process. Since infiltration can remove pores for the binder jetted part to increase density, it may enhance the mechanical properties including hardness, elastic modulus, yield strength, etc. [92]. To attain final product with desired properties, it is important to

optimize the saturation of infiltrant liquid. In the case that the liquid infiltrant exceeds the saturation level, the migration of excess infiltrant can affect the dimensional accuracy. If the lack of infiltrant happens, it can cause weak bonding between particles affecting mechanical properties. Thus, it is necessary to have a precise estimation of infiltrant saturation for a BJ3DP parts [89].

The other densification method for the binder jetted parts is sintering. Sintering kinetics and densification depend on (1) the powder particle chemistry and surface impurities, (2) powder morphology, (3) particle size distribution and (4) sintering atmosphere. The sintering kinetics and shrinkage during sintering of the green part are two other aspects affected by PSD. Therefore, powder properties as well as sintering step are critical aspects in BJ3DP of metallic material in which powder size distribution, powder morphology and chemistry, heating and cooling rates, sintering temperature and holding time may affect shrinkage, microstructure, porosity and phase formation in the final product. In the following, these concerns will be elaborated in more details.

2.2.10 Sintering

2.2.10.1 Sintering Theory

The sintering process is a critical step in binder jet 3D printing technology (BJ3DP) since the densification of the green part happens through a diffusion process. As the strength of the green part is owed to the cross-linking of the polymeric binder during printing, various mechanical strengths (static and dynamic mechanical properties) can be achieved after applying sintering to attain different density and microstructure. As the binder jetted part is porous with density of ~40-50%, the driving force of the sintering is primarily based on the reduction of surface energy of the BJ3DP part. Different stages happen during sintering, which affect the microstructure and

shrinkage behavior of the green part. Figure 19 illustrates the general sintering process for a powder system and in the following, main steps are explained in detail:

Figure 19(a) shows the prior of sintering, in which the green part density of the BJ3DP specimen is ~40-50%. No sinter neck can be seen and the surface bonding among powder particles is due to the binder used during the printing process. The initial stage of sintering happens at lower temperatures where the surface diffusion is usually the dominant mass-transport mechanism during the early stages of neck growth [93,94]. Initially, particles are in contact to form grain boundaries at the contact point through the diffusion process (see Figure 19(b)). Necks begin to form at the contact points between the adjacent particles without any dimensional change or porosity reduction. Generally, as the sintering temperature increases, sinter necks form due to material shifts on the surface of the particles to contact points, causing a linear shrinkage (dimensional changes) of ~3% [93–95]. The intermediate stage begins when the ratio of particles diameter (D) to sinter necks (X) is ~3, where the relative density of the sintered part reaches to ~70%.

The intermediate stage happens at higher temperatures where the grain boundary and volume diffusions are dominant and the part experiences a significant amount of densification up to ~92% as shown in Figure 19(c). Additionally, the pores of the part are initially smoothed, becoming more tubular as opposed to spherical. During the intermediate stage, sinter necks grow from approximately 1/3 to 1/2 of the powder particle diameter and as the densification progresses, pore evolution happens where the long, tubular pores become closed [93–95]. Thus, the pores channel closure takes place in which the interconnected pores are closed off isolating porosity due to sinter neck growth and/or the creation of new contact points as pore shrinkage happens. Consequently, materials migrate from inside of the particles to the surface, resulting in contact flattening and densification.

As the density increases to ~92% with closed pores and sintered necks of half the powder particle diameter, the part has entered the final stage of sintering process (see Figure 19(d)). The final sinter stage happens at the same or slightly higher temperatures as the intermediate stage. This stage is much slower than the initial and intermediate stages. During this stage, elimination of the closed pores takes place to achieve maximum density. Throughout the final sintering stage, grain coarsening happens in which pore coarsening may occur if the maximum density over 99% cannot be achieved [95,96]. During this stage, solids must by transported into the pores and a means needs to exist by which the gas in the pores/voids can escape to the surface.

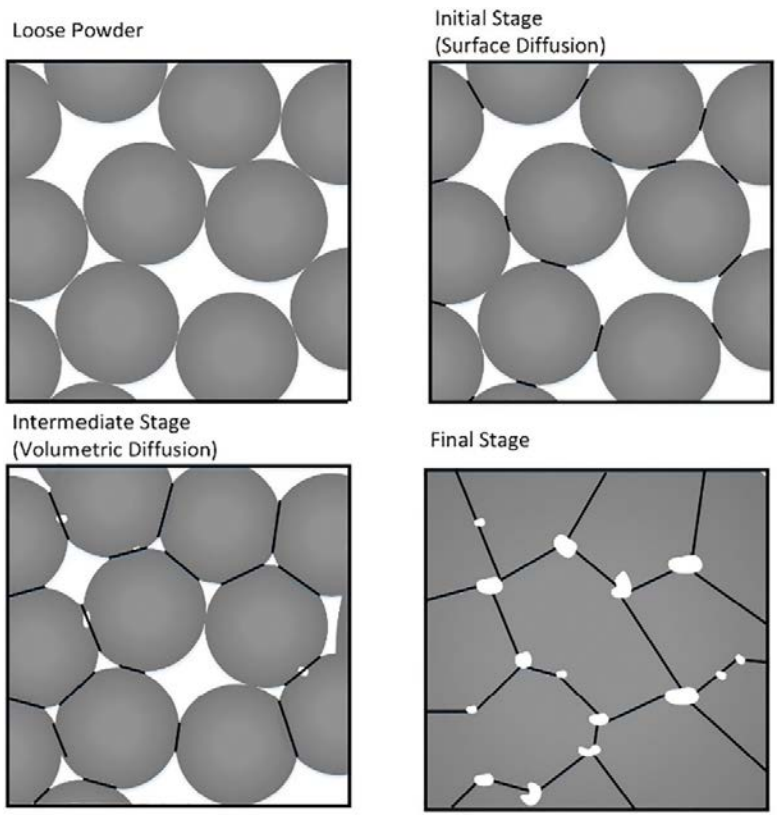

Figure 19. Schematic showing the general sintering process for a powder system, (a) un-sintered powder, (b) initial stage of sintering where sinter necks form, (c) intermediate sintering stage where the density increases due to shrinkage and pores closure, and (d) final stage where the grain coarsening may happen [97].

2.2.10.2 Sintering Thermodynamics

The thermodynamic or driving force of the sintering process is the reduction of Gibbs free energy of the system depending on the powder characteristics regardless of sintering temperature. In powder metallurgy and binder jetted parts, the energy of the system is based on the incomplete bonds of the weak joints among powder particles. Thus, the energy reduction of the system happens by reducing the number of atoms in a higher energy state. Sintering continues if the total energy in the system is decreased and finally, it stops once that is no longer possible.

Necks formation happens between the adjacent particles in the initial stage of sintering. Due to the effects of surface curvature on the powder particles, there is a huge driving force to generate necks [93,98]. There is an uneven distribution of forces on the atoms of a surface with curvature in which the surface tends to be in tension if it is concave and compression if it is convex [99,100]. With the formation of the sinter necks, the total curvature of the surface is reduced, resulting in the reduction of the total system energy where material moves from the convex surfaces (particles) to the concave surfaces (necks). Based on the surface stress values, the surface will have a higher vacancy (under tension stress) and lower vacancy (under compression stress) concentration, causing a source-sink relationship, in which material from the particles preferentially moves to the necks [96-98]. German [100] showed that with smaller radii, particles will have a higher curvature and driving force for sintering. In other words, smaller particles have a significantly higher stress and driving force for sintering where densification may happen at lower sintering temperatures compared to coarse powder particles. Besides reducing surface curvature, the sinter neck formation also reduces the surface area to volume ratio of the powder system, which is directly proportional to the inverse of the particle radii. By increasing the particle size, the total surface area of the powder system decreases, leading to the reduction of the system

energy. It contributes to the lower energy required for sintering of smaller powder particles as the comparatively high surface area to volume ratio gives the system a higher driving force for sintering. The other driving force in sintering is the grain boundary interfaces where the particles will undergo a stress relief and subsequently, a recrystallization process happens. Although the new boundaries have a lower energy than a surface-pore interface, they increase the total energy of the system and, as sintering progresses, the grains will coarsen to reduce system energy.

2.2.10.3 Sintering Kinetics

Generally, there are two major categories of sintering mechanisms, all of which can be active in some combination during the sintering process and the relative impact of each mechanism depends on the material and sintering conditions. The alloy chemistry is an important factor in selecting the optimized process temperature. It is vital to determine a correct sintering set temperature to attain full density and, therefore, sufficient mechanical properties. The main categories for sintering kinetics or mechanisms are solid-state and liquid-phase sintering. Solid-state sintering happens with the material in its solid form, and diffusion-controlled mechanisms dominate the process. In liquid-phase sintering, some volume of liquid is present, typically in small amounts to facilitate the sintering process. Both mechanisms can occur at the same time and the prevalence of each one depends on the sintering temperature. Particle size distribution and alloy chemistry have a direct impact on sintering kinetics. In the following, each mechanism is elaborated in detail.

2.2.10.4 Solid-State Sintering

Solid-state sintering happens when applied temperature is below the solidus temperature and, therefore, the material is in a solid state. In solid-state sintering, powder particle diameter is

the main governing factor. Based on the temperature and holding time, there are two distinct types of sintering mechanisms that contribute in different ways to the sintering process.

The first type is the coarsening or non-densifying sintering that happens at lower temperatures and includes surface effects where no movement happens on the powder particles centers to get closer together [101]. Here, materials are redistributed along the powder particle surfaces from convex (particle surface) to concave areas (neck). There is no material transportation from the core of the particle and, therefore, shrinkage is negligible (maximum 2-3%). Evaporation and condensation is another mechanism causing coarsening in the powder particles where the materials evaporate at convex areas and condense at concave areas, allowing materials to be transferred across pores rather than simply on or through the particles themselves (mechanism #1 in Figure 20). The tendency for material evaporation at convex and condensation at concave areas can be attributed to the slightly higher and lower vapor pressure at those areas, respectively [98,102]. It is worth noting that the effect of evaporation/condensation is negligible for most materials since the vapor pressure is low at any realistic sintering temperature [101,103]. Surface diffusion is present at the lowest temperatures of any of the mechanisms due to the comparatively high energy of particles on the surface and lower activation energy [93]. Thus, the structure is smoothed (or coarsened) to reduce surface curvature and surface area (mechanism #2 in Figure 20). If the temperature is slightly higher, in which the lattice diffusion from surface can happen, atoms may have a chance to move from the layer beneath the surface to the neck (mechanism #3 in Figure 20).

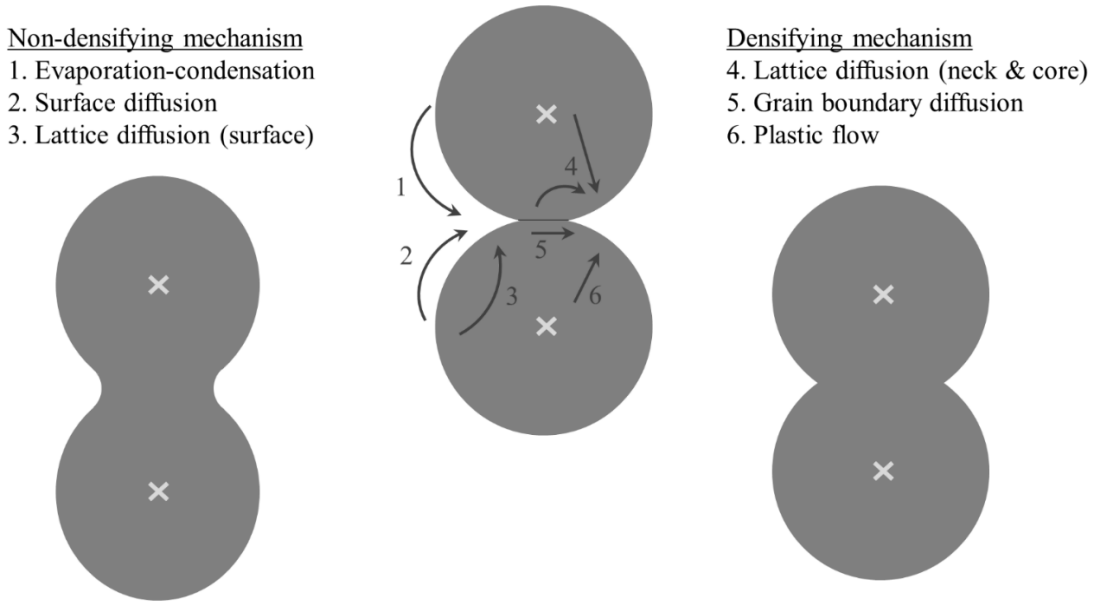

Figure 20. Two-particle geometry for possible transport mechanisms during solid-state sintering (detailed explanation can be found in [98,101]).

The second type is volumetric or densification sintering, which happens at higher temperatures and causes the shrinkage in parts to increase the density of the part [101]. In densifying sintering, mass transfer occurs from the core of the particles to the necks and, consequently, will cause the center of the particles to move closer together, leading to the shrinkage. Lattice or volumetric diffusion may happen in which the process is caused by vacancies in the lattice structure (mechanism #4 in Figure 20). This mechanism is active at temperatures close to the solidus temperature due to the requirement of a large number of vacancies to provide any meaningful mass flow [94,95]. Another densifying mechanism, grain boundary diffusion, occurs at lower temperatures compared to the volumetric diffusion since it does not depend on the creation of vacancies, with atoms being able to take advantage of the space provided by the grain boundary interfaces. Atoms can diffuse from the grain boundaries inside the powder particle to the surface of the particle to form sinter necks (mechanism #5 in Figure 20). Grain boundary diffusion

relies on the quantity of grain boundaries as well as temperature [94,95]. Plastic flow (mechanism #6 in Figure 20) happens when the movement of dislocations in the lattice structure occurs. These dislocation movements must happen at the surface and move inwards to either a grain boundary or isolated pore. This mechanism can only happen at lower temperatures since at elevated temperatures, the part is weak enough such that dislocations will not form.

2.3 BINDER JET 3D PRINTING OF NICKEL-BASED ALLOYS

Nickel-based super alloys are broadly used in aerospace, chemical and petrochemical applications as a high temperature structural material due to their high temperature mechanical and corrosion resistance properties. Traditional manufacturing such as casting [104] and metal injection molding [105–109] are the most common production methods for production of parts made from nickel alloys. Casting as a major conventional fabrication method for Ni-based alloys has difficulties to produce large ingot without facing issues such as elemental segregation, shrinkage defects and formation of undesirable phases [104]. Reducing these defects is a time consuming and expensive process, and forming and machining of the cast parts are difficult due to high hardness, mechanical strength ductility and work hardening [110]. The potential advantages of the production of superalloys by powder metallurgy or injection molding can be fabrication of a finer grain structure material. Additionally, a homogeneous chemical composition throughout of the product is achievable since the parts produced by PM methods consist of small sized particles, and therefore the biggest segregation distance is limited by particles size. Although injection molding could solve difficulties of producing complex shaped parts that was not practical

by traditional manufacturing methods, there is still limitation of production parts with internal and external complexity and porosity.

Alloy 718, also known as Inconel 718, is a solid-solution or precipitation strengthened nickel-based austenite superalloy, displaying remarkable combination of superior mechanical properties and good workability in highly aggressive working environments such as nuclear reactors [111], turbine blades and turbocharger rotors [26,112], aircraft turbine components, and various formed sheet metal parts for aircraft [113]. Alloy 718 has good processing characteristics, such as castability and hot-workability, as well as good weldability. However, precipitates and/or segregation may affect post processing. This alloy has been used in cast and wrought forms in which the microstructure in castings contains interdendritic regions with elemental segregation of niobium (Nb), molybdenum (Mo), and titanium (Ti). Even if the alloy has high Nb concentration, Laves phases such as $(Cr, Fe, Ni)_2(Ti, Nb)$ and $Ni_2(Cr, Mo)$ may form at the grain boundaries that have detrimental effect on mechanical properties. Hence, post heat-treatments including multiple homogenization steps are required to dissolve the Laves phase to create face centered cubic (FCC) gamma phase. Similarly, wrought alloy 718 needs post processing to reduce undesirable phases in the microstructure before thermomechanical processing. The exceptional mechanical properties of alloy 718 is due to a precipitation-hardened microstructure which is predominantly strengthened by γ''-phase precipitates $[Ni_3(Nb, Al, Ti)]$. These post processing steps as well as scrap generation during machining drive the cost of parts fabricated via traditional route and therefore, additive manufacturing can be an alternative to control microstructure and properties. Recently, researchers have successfully printed and characterized the alloy 718 at high relative density using BJ3DP.

In a research conducted by Turker et al. [113], effects of layer thickness and sintering temperature were studied on densification of alloy 718. Parts with were produced from gas

atomized powders (<53 µm) with layer thicknesses of 100 µm, 125 µm, 150 µm, 175 µm and 200 µm. After printing the individual layer by binder, the applied drying time was about 20 s. Green parts were then preheated at 80 °C for 2 h, then followed by depowdering and finally sintered at 1260 °C, 1280 °C and 1300 °C for 4 h in vacuum atmosphere. Based on the production parameters, different density ranging from 88% to 98.5% was attained. It was seen that the sintering at 1260 °C resulted in densities of 88–92% depending on layer thickness in which lower layer thicknesses led to achieving higher densities. Optical micrographs of the sintered samples at 1260 °C with various layer thickness showed considerable amount of porosity irrespective of layer thickness (Figure 21a), it was shown that samples produced at lower layer thickness (100 µm, 125 µm) had slightly lower porosity volume fraction. With increasing the sintering temperature to 1280 °C and 1300 °C, parts with density of ~99% was attained indicating that layer thickness had less effect on the final density. Generally, solidus and liquidus temperatures of wrought alloy 718 are designated as 1260 °C and 1335 °C and in a study conducted by Ozgun et al. [105], they reported these two values as ~1250 °C and 1305 °C. This difference can be attributed to the specific surface energy of the powder particle which is higher than the bulk alloy, thus, the measured solidus and liquidus temperatures are lower than the solidus and liquidus temperatures of a bulk material. Other aspects such as surface oxide layers on powder and chemical composition may affect these two temperatures. Shrinkage of the 3D printed parts after sintering at 1260 °C, 1280 °C and 1300 °C was shown in Figure 21b. samples sintered at 1260 °C experienced ~16.5% shrinkage while increasing sintering temperature to 1280 °C and 1300 °C resulted in a shrinkage of 19.5% and 21.5%, respectively. These values were the average number for different directions however, it is known that shrinkage in z direction is higher than two other axes. An inset in Figure 21b is an example of the printed (top) and sintered sample (bottom) indicating shrinkage in the 3D sample.

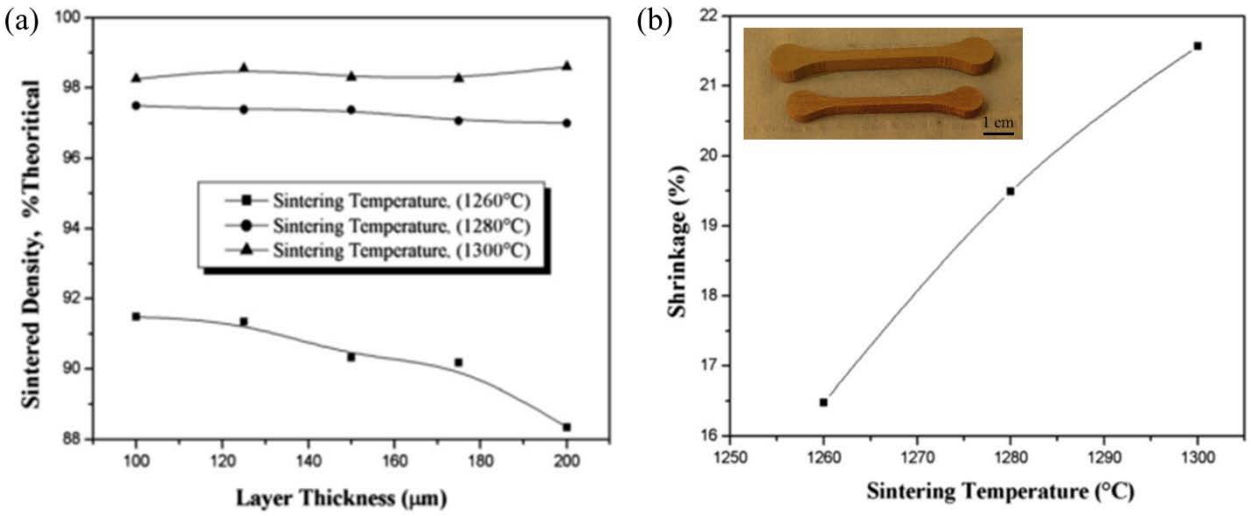

Figure 21. (a) Effect of layer thickness and sintering temperature on the density of alloy 718 parts produced by binder jetting and (b) shrinkage percentage of the alloy 718 depending on sintering temperature [113].

Optical micrographs (Figure 22) taken from the printed samples with layer thickness of 100 µm and 125 µm and sintered at 1260 °C, 1280 °C or 1300 °C showed that higher sintering temperature can lead to the high density; however, a small amount of grain coarsening took place, particularly at 1300 °C. In case of 1280 °C or 1300 °C, precipitates formed at the grain boundaries (dark areas). Besides, nano-size precipitates may form during sintering and are temperature sensitive. As shown in Figure 23, formed precipitates at 1280 °C disappeared in the sample sintered at 1300 °C. It was believed that these precipitates dissolve at around 1300 °C and leave the pits behind (Figure 22).

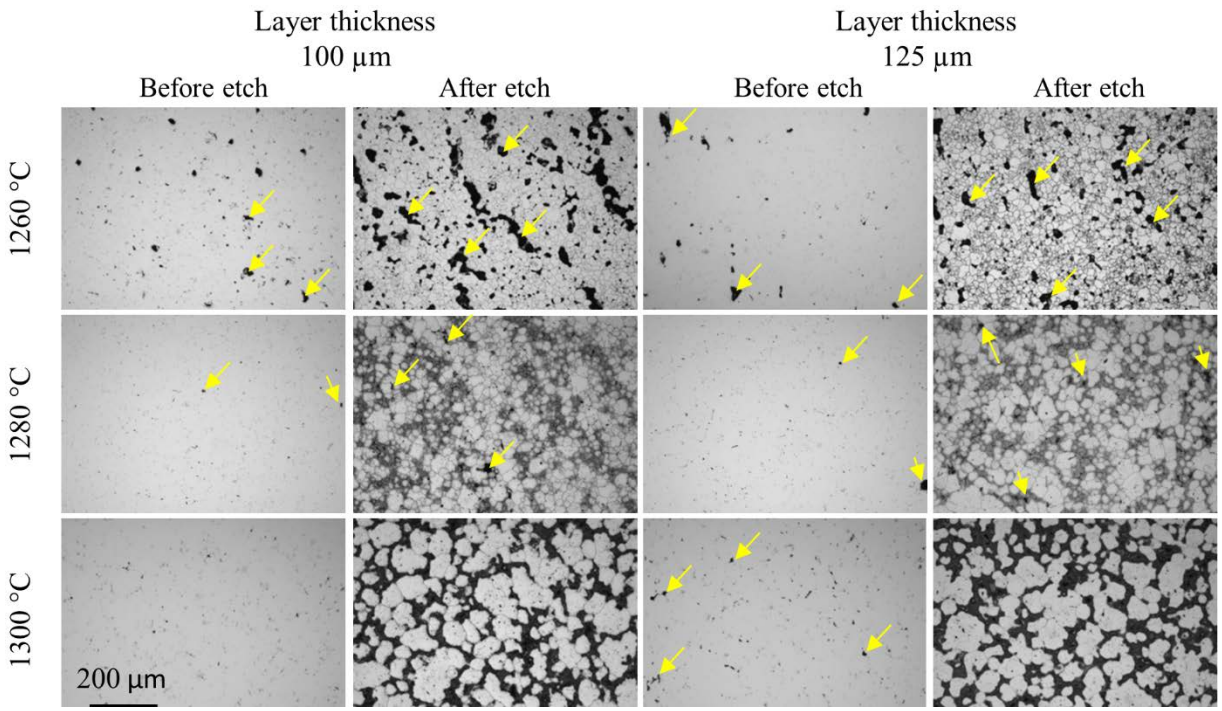

Figure 22. Optical micrographs taken from the BJ3DP alloy 718 printed with the layer thickness of 100 µm and 125 µm and sintered at different temperatures for 4 h [113]. Yellow arrows indicate porosity.

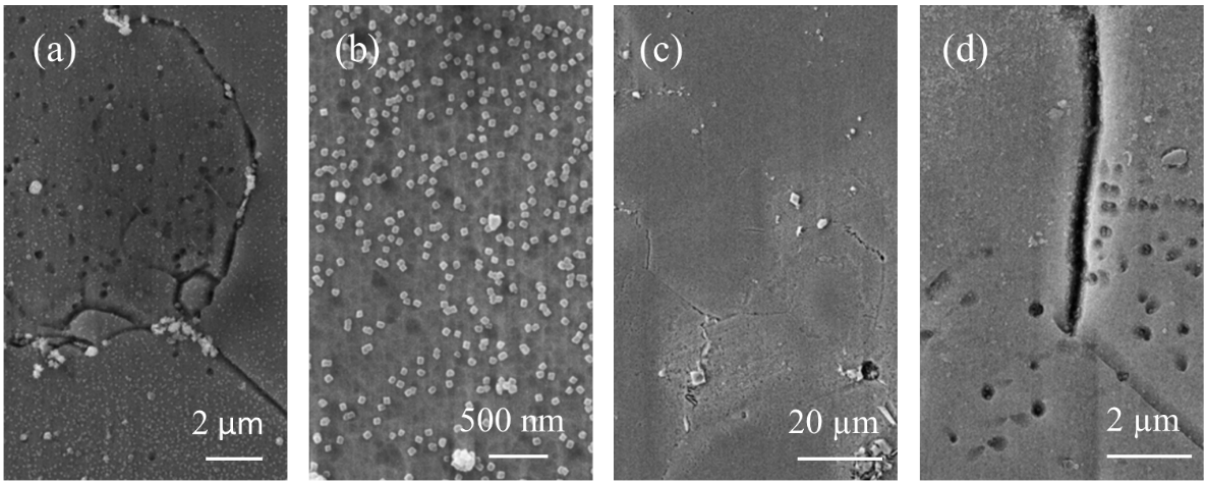

Figure 23. Scanning electron micrographs taken from sintered sample at (a,b) 1280 °C showing precipitate formation and (c,d) 1300 °C showing the partially dissolved precipitates [113].

Nandwana et al. [17,37] reported powder characteristics and well as binder jetting from different powder size distribution from alloy 718 (shown in Figure 24), and studied various shrinkage and densification in which smaller powder particles experience higher linear shrinkage compared to the larger powder particles sintered at the same sintering temperature. Powder size distribution of fine, medium and large powder particles was shown in Figure 24a. The plot comparing the apparent, tapped and powder bed densities for three powder size distribution was illustrated in Figure 24b. It was seen that different density measurements were higher for the 21 μm suggesting that it was possible to get a binder jetted part with higher green density compared to two other powder types. Typically, the powder bed density was between the loose and tapped density values. The finer the powders, the poorer they pack due to high inter-particle frictional forces which was the case for 7 μm powders. It was seen that the 21 μm powders had the highest tapped and powder bed densities due to the fact that wider powder size distributions skewed towards the finer particle diameters result in higher bed densities as seen for 70 μm and 21 μm powder particles [75]. Powder morphology is shown in Figure 24c-e.

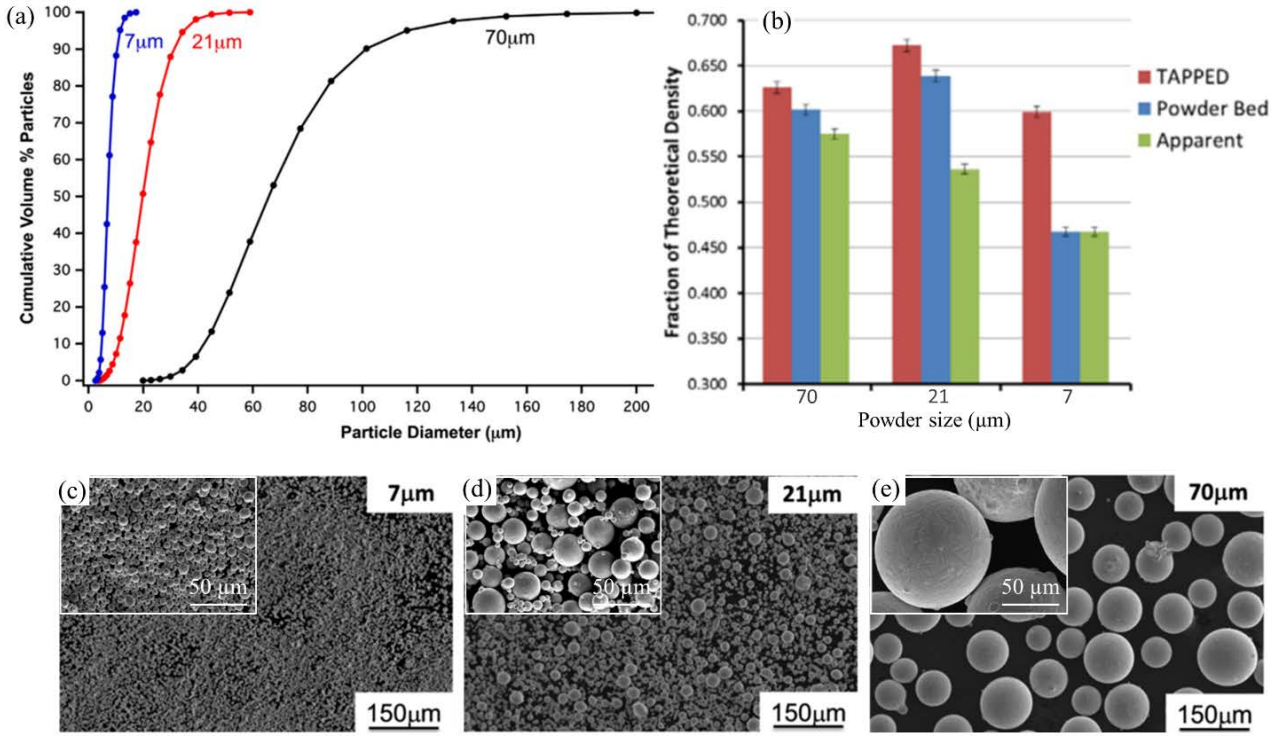

Figure 24. (a) Powder size distribution from gas atomized alloy 718. (b) Scanning electron micrographs with two magnification for (c) 7 µm, (d) 21 µm, and (e) 70 µm powder particles [17,37].

Linear shrinkage can be defined as $\delta L/L$ in which L_o and L are dimensions of the green part and sintered parts, respectively. In the work by Nandwana et al. [26], shrinkage of different powder size was studies experience solid-state and supersolidus liquid phase sintering (SLPS) and results are given in Figure 25a. It was seen that the finest powder showed the maximum shrinkage at all sintering temperatures. Two other powders, 21 µm and 70 µm, showed a cross-over point at ~1250 °C indicative of a change in the sintering mechanism from solid-state sintering to SLPS. Liquid volume fractions for three powders was shown in Figure 25b and it was found that 21 µm feedstock had a liquidus temperature that was about 30 °C and 40 °C higher than the 7 µm and 70 µm feedstock, respectively. During SLPS, one should know that the shape loss happens in the

compacts if the liquid volume fraction increases beyond 40% [114]. As the main purpose of authors was to study the liquid phase during SLPS, therefore the linear shrinkage was an unbiased parameter compared to change in sample heights. However, one should keep in mind that in BJ3DP of metallic powder, shrinkage in X and Y directions are mostly similar while it can be higher in Z direction (built direction). For one thing, if the compaction during rolling powder is not high enough, then it may be one reason of why shrinkage in Z direction would be higher than X and Y directions. Gravity could be another reason however as the sample size was small and sintering was done bellow solidus temperature, then it might be due to the fact that the binder filled space between each layer and therefore, part would have experienced higher linear shrinkage in Z direction. Finally, knowledge of feedstock chemistry and printing process are necessary to determine suitable sintering processing for solid-state sintering, liquid phase sintering or Supersolidus liquid-phase sintering of metallic powder resulting desired density, microstructures and properties.

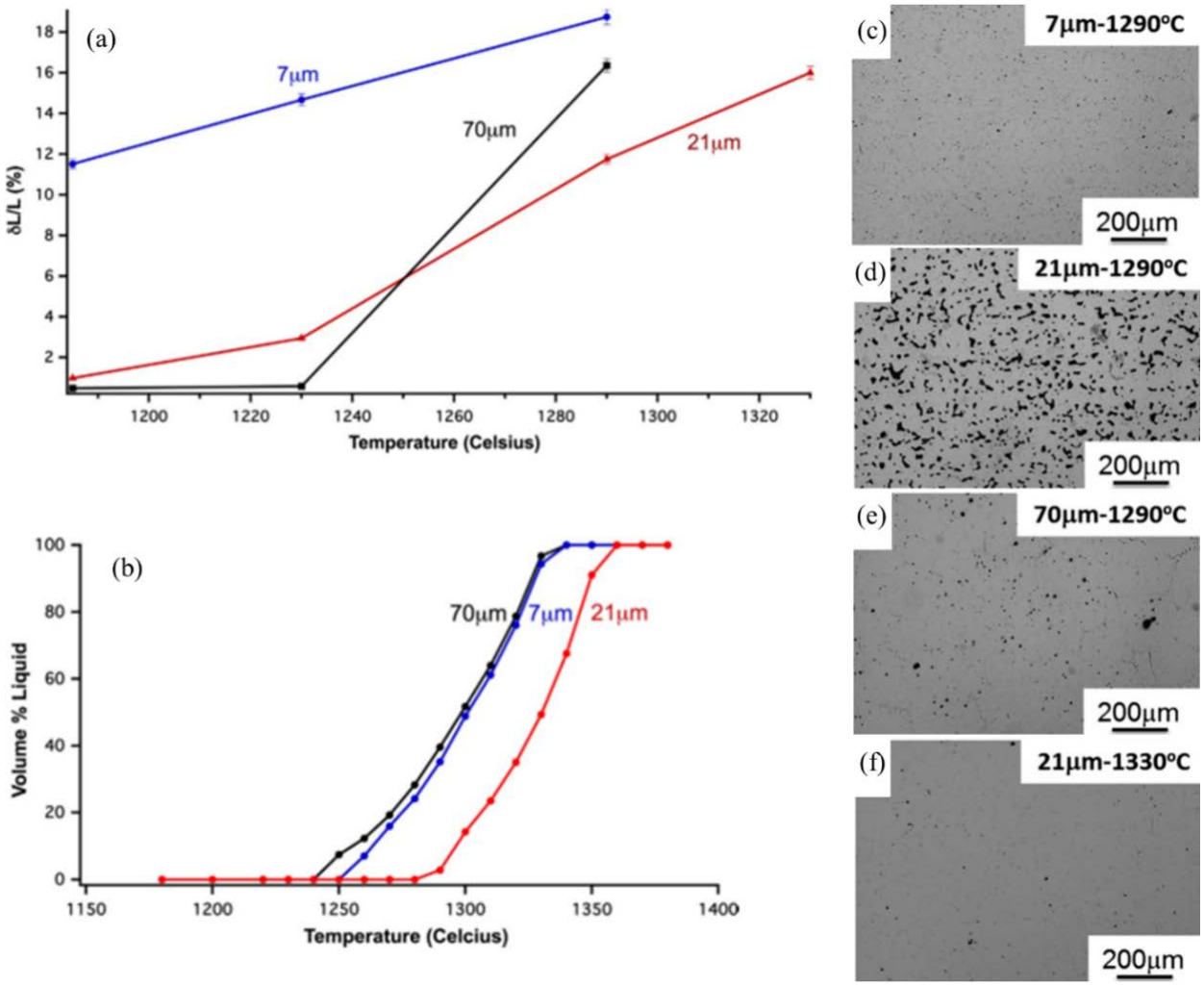

Figure 25. (a) Shrinkage for the three different powder sizes as a function of temperature, (b) Temperature dependence of liquid volume fraction for the three different powder samples based on Thermocalc calculations, (c-f) Optical micrographs comparing porosity in 7 µm, 21 µm, and 70 µm samples sintered at 1290 °C and the reduction in porosity of 21 lm sintered at 1330 °C [26].

It is seen in Figure 26 that the smaller powder particles (7 μm and 21 μm powders particle size) exhibited nodule like structure on individual powder particles while it was not the case for large power size distribution (70 μm powder particle size). Generally, as the mean particle size increases, the lower binder saturation level is needed during binder jet printing thus it can be one reason why large powder particle does not show any visible neck formation or the presence of nodules. Besides, it might be associated to the higher surface area of the small powder particles indicative of a change in the sintering mechanism. On the other hand, solid-state sintering is driven by reduction in surface energy per unit volume and thus, smaller size particles densify at a higher rate. Solid-state sintering usually happens in three stages including (1) initial stage involving necking and grain growth, (2) intermediate stage resulting in shrinkage and densification, and (3) final stage by elimination of close pores and dense microstructure formation.

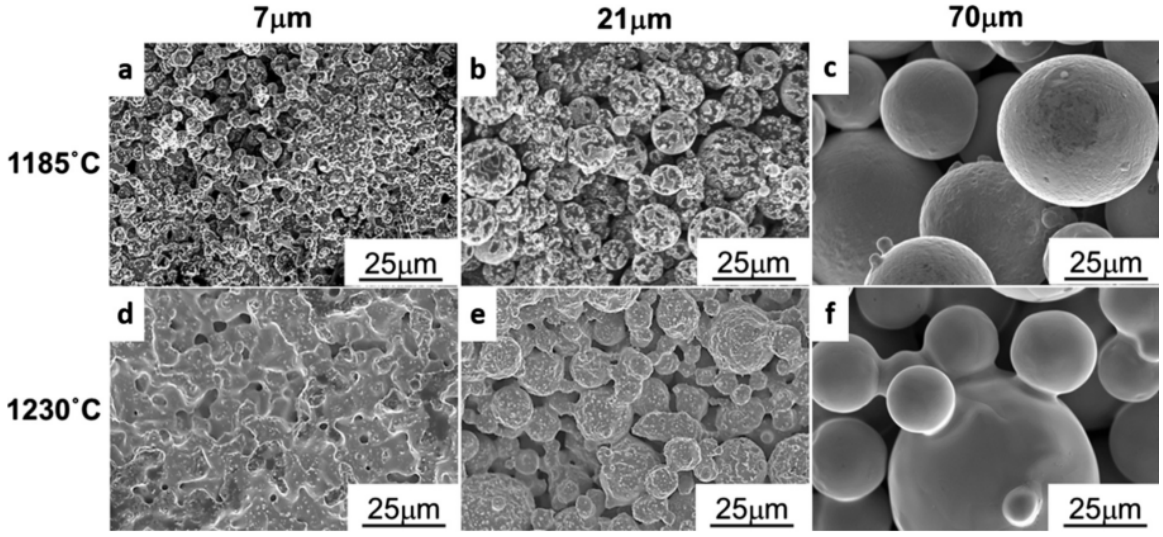

Figure 26. SEM micrographs taken from BJ3DP alloy 718 with three different powder sizes and sintered at two temperatures. Here, dependence of neck size on particle size and sintering temperature in solid-state sintering regime is illustrated [26]. Binder saturation level was reported as 80%, 80% and 70% for sample printed from powder size of 7 μm, 21 μm and 70 μm, respectively.

To develop a relationship between powder size and shrinkage, it is vital to comprehend the kinetics of mass transport across powder particles. Kuczynski [95] and Rockland [94] determined the mechanism of sintering in metallic particles based on whether grain boundary or volume diffusion dominates on the material transport mechanism. It is worth noting that both grain boundary and volume diffusion may occur simultaneously in the complex materials. By using Rockland's equations Rockland [94] in conjunction with Rahman's evaluation [103], we can define the following manner to express the dependence of bulk shrinkage ($\delta L = L_o$) for isothermal sintering rate:

$$\frac{\delta L}{L} \alpha\, t^m a^n \qquad (2\text{-}2)$$

where t is time, a is particle diameter, and m and n are exponents for time and particle size, respectively.

If the Supersolidus liquid-phase sintering mechanism is present during sintering process, meaning that materials are heated above the solidus temperature to enhance the diffusion within liquid in contrast to solid-state sintering in which the boundary and volume diffusivity are dominate. Figure 25c-e illustrated the optical micrographs of the three powders sintered at 1290 °C. Image analysis results showed that the closed pore density was below 1% for 7 μm and 70 μm powders while 21 μm powder had about 10% open pores. These results agreed with Archimedes method. As shown in Figure 25b, the 21 μm powder had lower liquid volume fraction (~3%) while it was ~35% or more for two other powders. Kingery [96] described quantitative aspects of liquid phase sintering and Liu et al. [115,116] expanded it for the SLPS, thus the main factors influencing shrinkage during isothermal SLPS can be expressed as follows:

$$\frac{\delta L}{L} \alpha\, t^m a^n F^p \qquad (2\text{-}3)$$

where $F = f_l/(1\text{-}f_l)^{2/3}$ with f_l being the liquid volume fraction and p being the exponential.

As presented in section 2.2, printing parameters and sintering condition as well as powder characteristics affect the microstructural evolution during densification. Microstructural evolution during SLPS of alloy 718 was studies by Nandwana et al. [26] as shown in Figure 27. Scanning electron micrographs taken from the 7 μm and 21 μm samples showed homogeneous equiaxed fine-grained austenite phase with average grain size of 25 μm in which carbides were distributed at the grain boundaries as well as within the grains. In contrast, the 70 μm sample exhibited multiple phases in the microstructure such as (Nb,Ti)C, Laves, and delta phase (δ) revealing of strong Nb partitioning to the liquid phase during sintering at 1290 °C. These phases were detected in channels between the coarse equiaxed grains. Electron microscopy observation at higher magnifications confirmed presence of gamma double-prime phase (γ", [Ni_3(Nb,Al)]) with dis-shape morphology in which γ" size changed from hundreds of nanometer in the vicinity of the Laves phase at the grain boundary to a few nanometers closer to the center of the grains [26]. Elemental analysis results confirmed that the precipitated in 7 μm and 21 μm samples (see Figure 27 a-b or original images with elemental map micrographs in [26]) are enriched C, Ti, Nb element while being depleted from other elements. In case of the 70 μm sample, the carbide and the Laves mutually exist in which the carbide phase is rich in C, Nb and Ti while being depleted in Ni and the Laves phase is richer in Nb and Ni. On the other hand, the presence of higher amounts of residual C from the binder resulted in the precipitation of metal carbides in small powders.

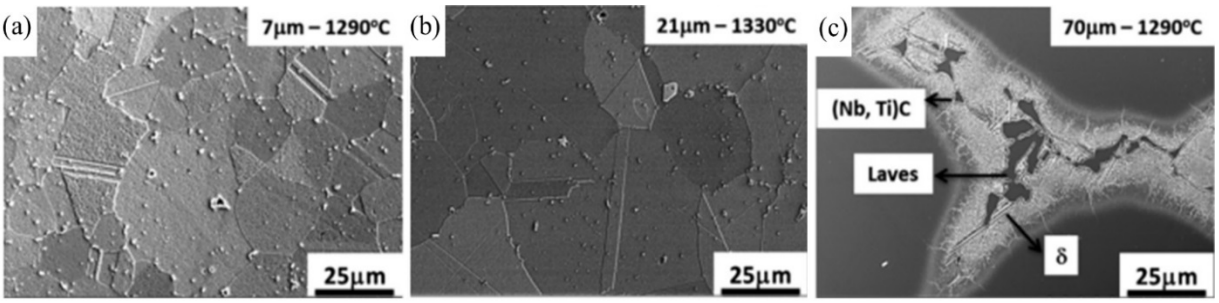

Figure 27. Scanning electron micrographs comparing microstructures of alloy 718 samples printed from three different powder particle size and then sintered to attain maximum density of 99.9% [26].

Alloy 625, also known as Inconel 625, is a nickel-based superalloy which is used in various engineering applications such as jet engines, pipelines, and structural materials [108]. The main difference between alloy 625 and 718 is the absence of aluminum element and, therefore, γ' [Ni_3(Al, Ti)] does not form. The main superior properties of alloy 625 compared to alloy 718 are better general corrosion resistance and long-term high-temperature stability. The main strengthening mechanism in alloy 625 is solution hardening; however, precipitation hardening also plays an important role in hardness, tensile strength and creep strength by formation of gamma double prime phase, γ'', [Ni_3Nb]. Additionally, intermetallic and carbide precipitates can form after an aging process between 550 and 750 °C. Since the precipitates of γ'' and Laves phases such as Ni_2(Cr,Mo) are generally between 10 and 50 nm in size and coherent with the matrix, a major source of strengthening in the alloy 625 is coherency strain [117,118]. The lattice mismatch between precipitates and the matrix plays a crucial role in the process of co-precipitation [119].

Mostafaei et al. [52] studied the effect of sintering temperature and post-heat-treatment processes on the binder jetting of vacuum-melted argon atomized alloy 625 powder. Detailed analyses on the powder size, morphology, size distribution, and phase and thermal behavior were conducted, as illustrated in Figure 28. Spherical powders with size distribution from 14 to 65 µm

and average of ~32 μm were binder jetted using an M-Flex printer (ExOne Company) into a part with a layer thickness of 100 μm and a water-based binder. The solidus and liquidus temperatures were reported as 1304 °C and 1334 °C, respectively. The applied sintering experiment was ranging from 1200 °C to 1300 °C with holding time of 4 h. Optical and electron microscopy observations showed that density was increased from ~70% for the sintering temperature of 1200 °C to 99.6% for the sintering temperature of 1280 °C. As density increased, shrinkage and shape change can occur in binder jetted parts. The green part density in the BJ3DP part is between 40% and 50% and the measured green density of the cured part was 53%. Linear and volume shrinkage measurements confirmed that as the sintering temperatures increased, shrinkage happened in the printed parts in which the maximum dimension and volume changes of ~19% and ~46% were seen for the sintering temperature of 1280 °C. It was noted that the sintering temperature higher than 1280 °C resulted in the liquid phase formation at the grain boundary, which might have a detrimental effect on the mechanical properties. Sintering at higher temperature (up to 1300 °C) led to the pore coarsening and its effect on density during final-stage sintering is a well-established phenomenon. The average pore diameter for the sintering temperature of 1280 °C was <4 μm, while sintering at 1300 °C resulted in pore coarsening to a diameter of 10 μm. Besides, grain coarsening has happened where the grain size of 55 ± 15 μm (sintered at 1280 °C) was increased to 182 ± 31 μm (sintered at 1300 °C). As expected, microhardness values were increased from ~110 $HV_{0.1}$ to 240 $HV_{0.1}$ as the density of the sintered part increased from 70% to 99.6% (sintered samples at 1200 °C and 1280 °C, respectively). Mechanical testing showed that the highest ultimate tensile strength (UTS) of 612 MPa, yield strength of 327 MPa, and fracture strain of 40.9% were achieved for the sintered part at 1280 °C, which was comparable to traditionally cast alloy 625 parts. Higher sintering temperature led to a reduction in the microhardness due to grain

coarsening and elemental segregation at the grain boundaries. After finding the optimum sintering temperature for the BJ3DP Ar-atomized alloy 625, post-heat-treatments including solutionizing and aging were conducted and followed by phase analysis, electron microscopy observation, and mechanical testing. Electron microscopy observation indicated that different phases appeared resulting from various heat treatment conditions. Carbides and topologically close packed phases (TCP) phases precipitate intergranularly with the nano- and micro-sized phases formed both inter- and intragranularly. XRD peaks and SEM observation on the sintered, solutionized, and aged samples indicated γ-Ni matrix with the carbides contained Nb and Mo elements. TCP phase as well as Cr_2O_3 were formed at the grain boundaries as well as in the grains. Microhardness testing results revealed that the post-treatment can increase hardness value up to ~330 $HV_{0.1}$ after the aging procedure. The solution-treated and aged samples were tensile tested, showing a UTS of ~590 MPa and ~700 MPa, respectively. Additionally, the highest ductility of 45% was gained from the solution-treated sample and it dropped to 30% after aging treatment. Microstructure studies on the sintered and aged samples showed that unlike the solution-treated sample, precipitates such as carbide and TCP phases may form in the microstructure, resulting in the differences in the elongation, yield stress, and strength values, as well as microhardness values as given in Figure 28. Ozgun et al. [108] showed that powder injection molded (PIM) alloy 625 (with size distribution of 4-27 μm and sintered at 1290 °C) had equiaxial grains with an average grain size of 100–150 μm in which the yield strength, tensile strength, elongation, and hardness values were 351 MPa, 650 MPa, 45% and 208 $HV_{0.1}$, respectively, and they changed to 385 MPa, 650 MPa, 40% and 313 $HV_{0.1}$ after the aging treatment.

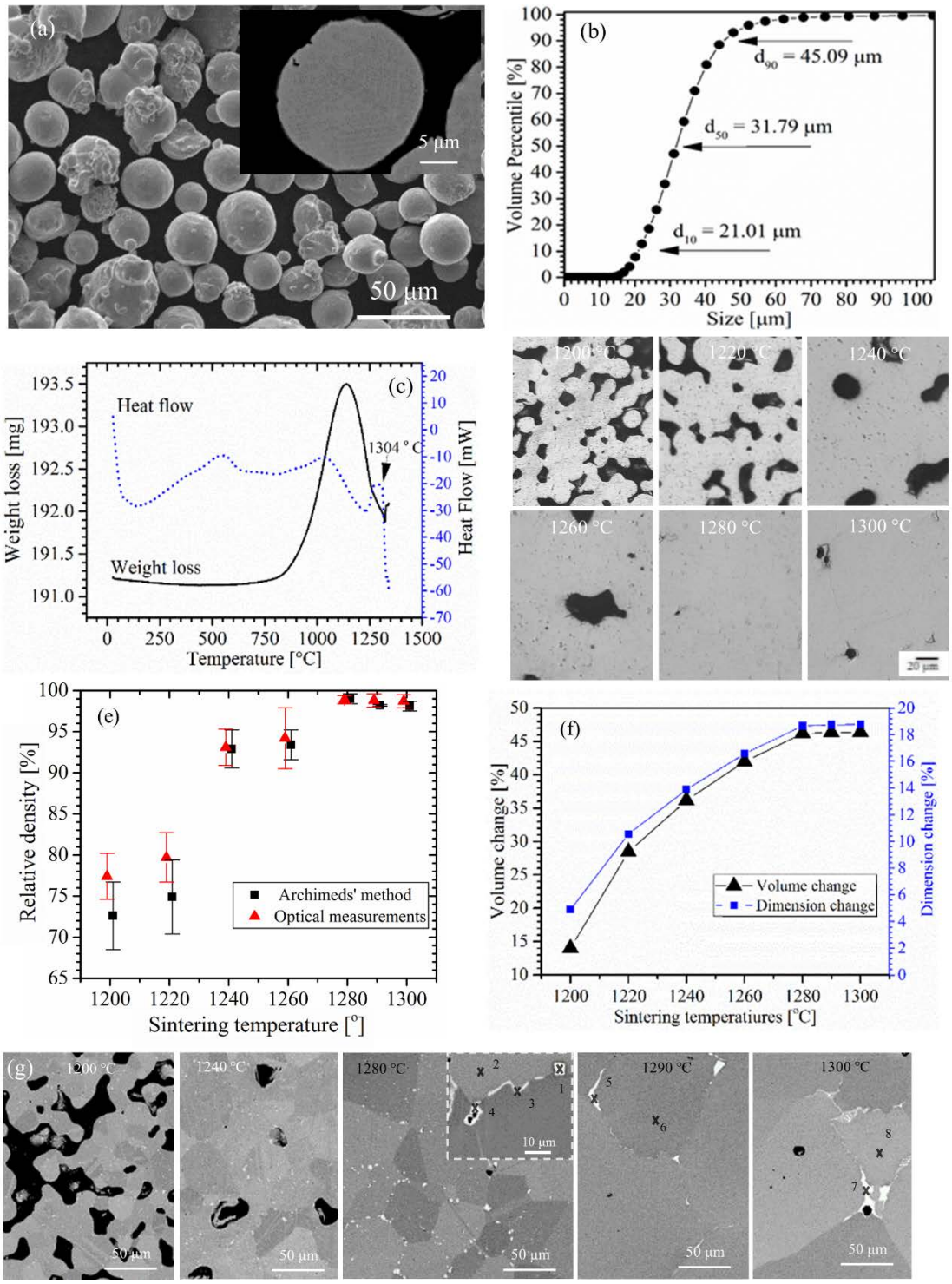

Figure 28. (a) SEM micrographs of the alloys 625 powder, (b) powder size distribution, (c) DSC-TGA curves of the alloy 625 powder, (d) optical micrographs of the sintered parts, (e) relative density of samples sintered at different temperatures ranging from 1200 to 1300 °C, (f) dimension and volume variations of the sintered samples depending on sintering temperature, (g) SEM micrographs taken from the sintered samples,

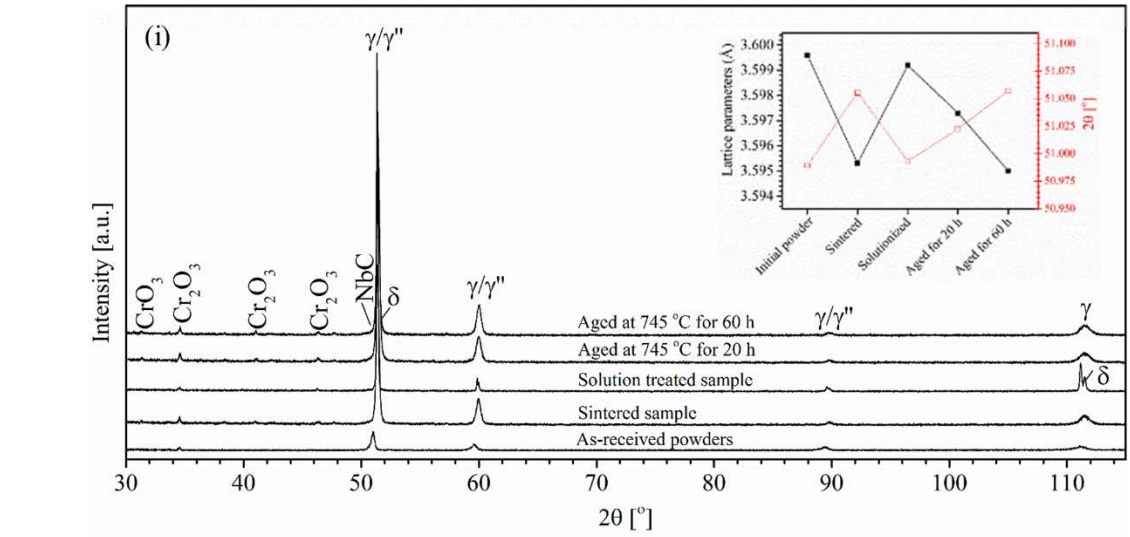

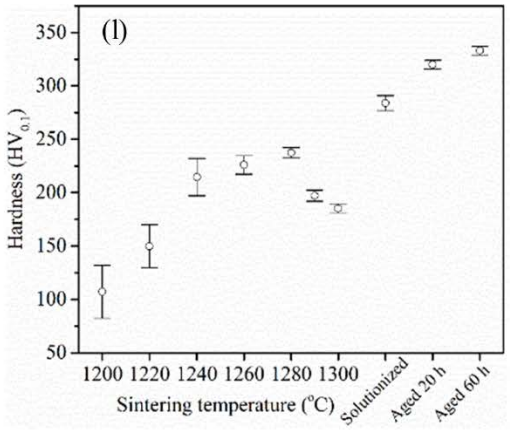

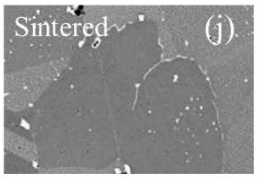

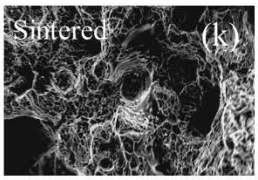

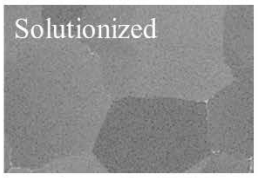

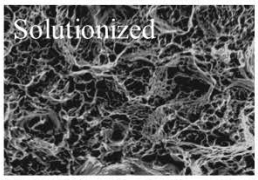

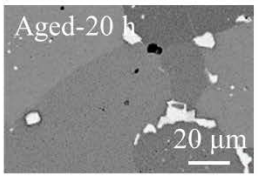

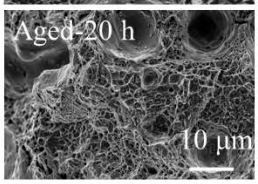

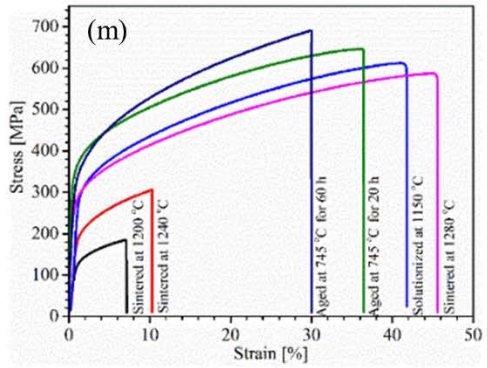

(n)

Sintering temperature °C	YS [MPa]	UTS [MPa]	Elongation [%]
Binder jet printed alloy 625			
Sintered (1280 °C, 4 h)	327 ± 11	612 ± 19	40.9 ± 3.1
Solutioned (1150 °C, 2 h)	311 ± 23	587 ± 57	45.1 ± 3.3
Aged (745 °C, 20 h)	373 ± 14	647 ± 27	35.8 ± 5.9
Aged (745 °C, 60 h)	392 ± 18	697 ± 29	30.1 ± 6.7
Injection molded alloy 625 [10]			
Sintered (1300 °C, 3 h)	351 ± 14	650 ± 16	44.7 ± 2.4
Solutioned (1150 °C, 2 h)	306 ± 29	505 ± 105	46.2 ± 2.5
Aged (745 °C, 22 h)	385 ± 12	647 ± 39	40.06
Cast alloy 625 [19]	350	710	48

Figure 28 (continued) (i) XRD patterns of the binder jetted parts experiences different heat treatment conditions, (j) SEM micrographs of the differently heat treated parts, (k) SEM micrographs taken from the fracture surface of the differently heat treated parts, (l) microhardness results, (m) typical tensile results of the sintered, solution-treated, and aged samples, and (n) mechanical testing results compared with injected molded and cast alloy 625 [52,120].

3.0 HYPOTHESIS

Binder jet 3D printing with controlled post-print heat treatments is capable of producing parts with controlled density, desirable microstructure and mechanical properties. As mentioned earlier, there is no heat input during printing process therefore the problem of residual stress is negligible in binder jetting compared to beam-based additive manufacturing techniques. Depending on the powder mean size, morphology and distribution span, parts with complex geometry and designed porosity can be binder jetted and then consolidation can be conducted by sintering process. Based on the application, fairly porous to near full density parts with controlled microstructure can be achieved by applying proper sintering and post heat treatment conditions.

Recently, researchers have printed and qualified the Ni-based superalloys at 99% relative density using BJP with a binder, which no longer needs infiltration of another element [26]. Without any thermal residual stress/distortion in BJP-printed parts, this streamlined manufacturing process makes BJP much more attractive for manufacturing complex parts out of Ni-based superalloys. To enable wide adoption of this BJP technology by the manufacturing industry, the porosity and mechanical properties of the Ni-based superalloys parts fabricated by this technology needs further improvement. It is well-known that the most important microstructure characteristic affecting mechanical properties is porosity [113]. This is because pores suffer from high stress concentrations, which promote the initiation and growth of cracks. As such, reducing porosity in printed parts made by BJP is currently the top priority. The reduction of porosity can be achieved

by studying the effects of powder properties, process parameters, and post-processing parameters. While the ability of AM to manufacture complex parts is a demand in various industries, it is important to better understand the processing microstructure property before widely adopting the technology and the main hypothesis here is the possibility of producing BJ3DP parts from alloy 625 with the same or even better properties as cast alloy material.

Kinetic models of sintering use simple geometries to model the microstructure evolution during densification in a series of stages including initial, intermediate and final steps. The initial stage of sintering involves densification by growth of isolated necks at particle contacts and is usually employed to model a limited range of densification [93,94]. When neck begin to overlap intermediate stage sintering models are employed. The pores remain open and are approximated as cylindrical pores channels until the pores begin to pinch off at bulk densities above ~92%. In final stage sintering pores are represented as relatively small spheres at grain corners. Throughout final sintering stage, grain growth accelerates causing rapid increase in the diffusion length and consequent decrease in densification rate which can limit the final density [95,96].

The alloy chemistry is also an important factor in selecting the optimized process temperature. It is vital to determine the correct sintering temperatures for attaining full density and, therefore, optimum mechanical properties. Along with the alloy chemistry, the particle size distribution has a direct impact on sintering kinetics. Yan et al. reported that the addition of small powder particle enhances surface area and reduces sintering temperature [121]. Green part density and flowability of powder mixtures are characteristics of these materials which depend on partic1e morphology, powder size particle size distribution [122]. The green density of a powder mixture increases with the addition of large particles to a small particle matrix. Typically, porosity (in terms of percentage, distribution and size) of powder metallurgy (P/M) compacts is affected by initial powder size.

Small powder particles produce a high quantity of small pores distributed through the entire part; while large particle size produces a small number of big pores, heterogeneously distributed in the sample. Randall German [76,80,122] showed that how the particle size distribution might be used to improve the pore size distribution and final properties. Generally, mono-sized and bimodal particles can produce wide pore size distributions in the microstructure of the green part. Besides, use of broad particle size distributions is an alternative to enhance green part density and attain high density of the sintered part with improved properties. It is necessary to point out if the composition of small and large powders are different, it may affect densification behavior due to chemical reaction at boundaries. Further grain growth, pore-grain boundary interactions, and pore coarsening may postpone densification.

The main hypotheses of this research are:

1. Powder characteristics such as morphology and size distribution affect densification behavior of BJ3DP alloy 625 parts.

2. Microstructure and mechanical properties of BJ3DB alloy 625 samples are comparable with cast and/or powder injected molded samples, if samples have 99% or more relative density.

3. The fatigue life of BJ3DB alloy 625 parts is affected by surface treatment if parts have a density of 99% or higher.

4. The dominating densification mechanism during isothermal sintering depends on powder size distribution, average particle size, and sintering temperature.

By varying the sintering temperature of different samples and measuring density at multiple time periods during sintering, the densification rates and effectivity can be analyzed. When this resulting data is paired with grain measurements received through quantitative stereology, the sintering kinetics of the metal are evaluated. By having the database developed,

significant value will be added to the knowledgebase of Ni-based alloy 625 fabricated by the BJ3DP process. For instance, the materials data can be employed by designers to feed computational models to predict part performance with confidence. Ultimately, the availability of materials data will provide significant time and cost savings for industry to adopt BJP for their alloy 625.

4.0 OBJECTIVES

Alloy 625 (or Inconel 625) is a nickel-based superalloy which is used in various engineering applications such as jet engines, pipelines and structural materials [108]. The main difference between alloy 625 and 718 is the absence of aluminum element and therefore γ' [Ni_3(Al, Ti)] do not form. The main superior properties of alloy 625 compare to alloy 718 can be better general corrosion resistance and long-term high temperature stability. The main strengthening mechanism in alloy 625 is solution hardening; however, precipitation hardening also plays an important role in hardness, tensile strength and creep strength by formation of gamma double prime phase, γ'', [Ni_3Nb]. Additionally, intermetallic and carbide precipitates can form after an aging process between 550 and 750 °C. Since the precipitates of γ'' and Laves phases such as Ni_2(Cr,Mo) are generally between 10 and 50 nm in size and coherent with the matrix, a major source of strengthening in the alloy 625 is coherency strain [117,118]. The lattice mismatch between precipitates and the matrix plays a crucial role in the process of co-precipitation [119]. It is apparent that the required microstructure can be gained by applying various heat treatment processes. In fact, the mechanical properties at elevated temperature strongly depend on the microstructure of the printed part. It is even more important in the presence of other precipitates such as carbides, σ and δ precipitates. Thus, formation and distribution of these phase should be precisely investigated in the microstructure and their influence on the long-term performance would be important.

Generally, two common techniques are used to produce nickel-based alloy powders: (1) gas atomization (GA), leading to spherical particles that pack to higher density, and (2) water atomization (WA), leading to irregular particles with better shape retention ability and lower cost [47]. Although GA powder is most commonly used for manufacturing of Ni superalloy components, higher costs are a consideration. To achieve required material characteristics such as ductility, strength and corrosion resistance, microstructural evolution during sintering is crucial. For injection molded WA and GA stainless steel powder, sintering results in 97% density for WA powder samples, while GA powder parts sintered to near-full density due to particle morphology, initial green density and particle chemistry [47]. For WA and GA Ni-based alloy powder, a denser microstructure was reported for GA samples than WA samples because of lower oxygen content and higher packing density of GA powder [49].

It is well-established that the final microstructure of a sintered body depends on the powder properties (e.g. powder size, particle size distribution and morphology), the green microstructure and sintering processing parameters (e.g. temperature and holding time) [93,121,123,124]. The main categories of sintering are solid-state and liquid-phase sintering [93,100]. Solid-state sintering occurs by solid state diffusion mechanisms that result in densification. In liquid-phase sintering, some volume of liquid is present, typically in small amounts to facilitate the sintering process. The prevalence of each depends on the sintering temperature.

Mechanical surface treatments play an important role in improving surface roughness and fatigue resistance by producing a compressive residual stress in the surface region of metallic parts. The compressive stress results in a delayed crack initiation and retarded crack propagation. There has been only limited investigation into the fatigue life, crack propagation, and fracture toughness of additively manufactured alloy 625 [125,126]. It was reported that the fatigue life of the cast and

additively manufactured parts is significantly lower compared to the wrought material [127]. While this report did not demonstrate the root cause of the lower performance, a different investigation into Ti-6Al-4V [128] demonstrated four key factors for fatigue performance: (1) residual stress, (2) microstructure, (3) porosity, and (4) surface finish. These four factors will be investigated as possible factors influencing fatigue performance.

In recent decades, substantial progress has been made in the understanding, development and utilization of additive manufacturing processes. Binder jet 3D printing (BJ3DP), a non-beam based, additive manufacturing (AM) method, refers to the technology in which powdered material is deposited layer-by-layer and selectively joined in each layer with binder and then densified through sintering. Binder jetting holds distinctive advantages among additive manufacturing technologies due to its fast, low-cost manufacturing; stress-free structures with complex internal and external geometries; and the isotropic properties of the final printed parts. Many studies have been carried out on the densification of the BJ3DP parts from nickel-based alloys [25,26,33–35,113,129,130], titanium [131–133], iron-based and stainless steels [134–139], copper alloys [37,140], cobalt-based alloys [141,142], and magnetic shape memory alloys [143,19,144]. However, there is much less literature on the kinetics of sintering, evolution in microstructure and the mechanical properties of the binder jetted parts. Consequently, following challenges are the ***objectives*** of this project and results are compared with cast alloy and/or powder injection molded alloy 625:

- Studying the powder morphology (resulted from different atomization methods) and sintering condition effect on the densification, microstructural evolution and mechanical properties of the gas and water atomized powders. Effect of differently heat treatment such as solutionizing and aging treatments on the microstructural evolution, phase formation

and mechanical properties of the BJ3DP alloy 625 parts. It is predicted to attain relative bulk density of ~99% with equiaxed microstructure and mechanical properties such as hardness and tensile strength similar to cast alloy and or P/M parts made from alloy 625.

- Surface finish effect (e.g. as-sintered and mechanically ground surface) on the fatigue behavior of the BJ3DP part from GA alloy 625. The fatigue behavior of cast alloy 625 has been summarized in Refs. [126,127]. Despite some investigation into the fusion processes of metallic materials, there is little information on the fatigue behavior of BJP parts made from metallic materials. While earlier BJP studies [19,24–26,33,145–151] pertain to densification, microstructural analysis, hardness and a few investigations into tensile property characterization, we aim to evaluate the fatigue properties of alloy 625 created with BJP. Specifically, samples in their as-sintered and polished state will be characterized, and tested in fatigue. An improved understanding of fatigue performance will guide the printing and post-processing of alloy 625 in real-world applications. It is expected to reach a fatigue life of 100,000 cycles as the applied stress is ~300 MPa.

- Influence of powder size and particle size distribution on densification and linear shrinkage of differently sintered binder jetted parts was studied with particular emphasis on microstructural evolution. In particular, the correlation of the kinetics of densification with grain/pore intercept length, pore separation, surface area per unit volume, volume strain rate and number of pore sections per unit area were evaluated for binder jetted alloy 625 for powders of different particle size distributions at sintering temperatures below the solidus. It will be studied how powder mean sized and particle size distribution affect densification kinetic and final microstructure, if printing parameters such as layer thickness, binder saturation and drying time are similar.

5.0 MATERIALS AND METHODS

5.1 BINDER JET 3D PRINTING OF ALLOY 625

Differently atomized alloy 625 powder including air melted nitrogen atomized (NA) and air melted water atomized (WA) powders were supplied by Carpenter Technology Corporation (for gas atomized powders) and HAI Advanced Material Specialists, Inc. (for water atomized powder). The nominal, provided and measured chemical compositions are given in Table 1.

Table 1. EDS composition of WA and GA nickel-based alloy 625 powders and oxygen and carbon content of as-received powders and printed/sintered samples [wt.-%].

	Composition in atomic weight percent [wt.-%]													
Elements	Ni	Cr	Fe	Nb	Mo	Al	Ti	Co	Mn	Si	O	C	O	C
Nominal composition [18]	>58	20-23	<5	3.1-4.1	8-10	<0.4	<0.4	<1.0	<0.5	<0.5	as-received powder		printed and sintered	
WA powder (provided)	Bal.	21.8	3.6	3.5	9.3	<0.4	<0.4	<1.0	0.4	-				
WA powder (EDS)	Bal.	16.9	3.7	3.7	8.7	0.05	0.16	0.62	0.8	0.7				
NA powder (provided)	Bal.	21.5	4.2	3.3	8.9	-	-	-	0.4	0.4				
NA powder (EDS)	Bal.	21.8	4.4	3.6	8.0	0.02	0.02	0.22	0.4	0.5				
WA											1.90	0.09	1.43	0.65
NA											0.04	0.01	0.28	0.44

Powder morphology and elemental composition analyses were conducted with a JEOL (JSM 6510) scanning electron microscope (SEM) equipped with energy dispersive X-ray spectroscopy (EDS). X-ray diffraction (XRD) was performed on a PANanalytical EMPYREAN diffractometer with a Co K_α radiation source (λ = 1.79 Å, 40 kV, 40 mA) and 2θ scans from 35° to 120°. The particle size distribution (1 g each suspended in isopropyl alcohol to prevent agglomeration) by volume and number was analyzed with a Microtrac S3500 tri-laser diffraction particle analyzer via spherical and non-spherical particle algorithms. Phase transformation temperatures (solidus, solvus) were measured with a TA Instruments Q 600 differential scanning calorimeter (DSC) by heating powder samples to 1350 °C at 10 °C/min in ultra-high purity Ar (100 mL/min).

General morphology and internal porosity of powder particles and as-printed samples were visualized with a Bruker SkyScan1272 micro-computed tomography scanner (μCT) at 100 kV and 100 μA and a 0.11 mm Cu filter, averaging of 10 frames, and angular range of 0°–180° with 0.2°-0.3° steps. Powder samples were filled into a low absorbance 1.5 mm plastic straw, compacted to reduce particle movement and scanned without random movement.

To manufacture parts, an M-Flex ExOne binder jet printer (BJP) was used as detailed in [15]. The water based binder was provided by ExOne Company with the compositions of ethylene glycol monobutyl ether (10 volume percent, CAS # 111-76-2) and ethylene glycol (20 volume percent, CAS# 107-21-1). Binder saturation level was 70% during print. After printing, the fragile GA and WA parts (“green parts”) were cured at 175 °C in a JPW Design & Manufacturing furnace and then sintered in a Lindberg tube furnace in an alumina powder bed under vacuum with the following heating profile: heating at 5 °C/min from room temperature to 600 °C, 3.2 °C/min to 1000 °C, 2.8 °C/min to the holding temperature ranging from 1200 °C to 1300 °C, holding for 4 h

and then cooling at 1 °C/min to 1200 °C, 3.1 °C/min to 500 °C and finally cooling down to room temperature. Five samples for each combination of sintering temperature and powder type were prepared. After sintering, samples with highest density were solution treated at 1150 °C for 2 h and aged at 745 °C for 20 h.

Density and volume changes (shrinkage) of the as-printed and sintered samples were measured via the Archimedes principle with an OHAUS AX324 precision balance (0.1 mg resolution). Density of the sintered samples was also determined from sample cross-sectional optical micrographs with the ImageJ image analysis software [152]. For microstructural examination of the sintered coupons, cross sections were cut from the specimens, mounted, ground and polished using a Struers Tegramin-25 automatic system according to [153]. After surface preparations, samples were etched with a Kalling solution (ASTM E407, # 94) and micrographs were taken with a Keyence digital optical microscope (OM) (dark field Z20 lens and multi-diffused adapter). Microstructural characterizations, compositional analysis and fractography were conducted with a JEOL JSM 6510 SEM equipped with EDS. The *d*-spacing values and lattice parameters were determined with the same XRD and scan parameters used for as-received powder. Carbon and oxygen contaminations were detected with LECO TC600 Oxygen/Nitrogen and CS844 Carbon/Surfur Analyzers.

Vickers microhardness tests were performed on the cross sections of samples with a Leco LM 800 microhardness tester (100 gf for 10 s). Rate controlled tensile tests at 5 mm/min were performed using an MTS 880. Dimensions of the as printed sample were 125 mm long, 12.5 mm wide, 7.5 mm thick, and gage length of 29 mm. For the mechanical testing, an ASTM standard test method for tension testing of metallic materials (ASTM Standards, vol. 03.01. Designation E8-04) was used.

5.2 FATIGUE LIFE STUDIES

The sample geometry for fatigue study was designed according to ASTM E466-07 [154] and 60 samples were printed using an M-Flex ExOne binder jet printer with processing parameters as presented in Refs. [52]. The green parts were cured to improve strength of the printed samples at 175 °C in a JPW Design & Manufacturing furnace and then sintered in a Lindberg tube furnace in an alumina powder bed under vacuum at 1285 °C for 4 h. A sintering temperature above the liquidus line for this composition was chosen to ensure liquid-phase sintering. The curved surface of the sintered samples was mechanically ground manually using a rotary tool (Dremel 4000, Dremel, Racine, Wisconsin, USA).

The samples were fatigue tested in air using a hydraulically driven load-frame (MTS 880, MTS, Eden Prairie, Minnesota, USA) under a stress-controlled, sinusoidal waveform with a tension-compression condition at R = -1 with 5 Hz and 7 Hz frequency (for the as-sintered and mechanically ground samples, respectively) where $R = \sigma_{min}/\sigma_{max}$ and σ_{min} and σ_{max} are the applied minimum and maximum stresses, respectively. The run-out limit was set to 10^7 cycles. Engineering stress values were selected between 175 MPa and 375 MPa with 25 MPa intervals. As presented in our earlier study [33], yield strength of the BJ3DP alloy 625 is 376 ± 14 MPa. For each specimen, the central diameter of the curved surface was measured in order to calculate the required force for each test condition. Before fatigue testing, some samples were sectioned for metallographic examination using SEM. SEM was used to observe the fracture surfaces.

Surface roughness profiles were measured using a stylus profilometer (Alpha-Step IQ, KLA-Tencor, Milpitas, California, USA). A 5-µm radius tip was used with a 16.5 mg load. Measurements were performed with a scan length of 5 mm, a scan rate of 10 µm/s, and a data sampling rate of 100 Hz. This yields points every 100 nm in lateral position. Scans were conducted

parallel to the long axis of the sample at 10 different radial positions along the circumference. In all cases, the data is tilt-compensated by subtracting out the mean line, and also parabola-compensated to remove the contribution of overall sample geometry from the measurement of surface topography.

The surface morphology and roughness of the specimens were also analyzed by an optical profilometer (ContourGT, Bruker, Billerica, MA, USA). The print direction was determined by observing the horizontal print lines on the end of each sample. The flat sample end was then marked perpendicular and parallel to the print direction with the perpendicular direction being north (N) and south (S) and the parallel direction being east (E) and west (W). Each of these quadrants was bisected and respectively marked NE, NW, SE, SW for a total of 8 measurement directions. For each direction, a scan was performed with an objective lens with magnification of 5X, resulting in sample sizes of approximately 1 by 0.75 μm.

To evaluate the extent of sub-surface deformation and stress, microhardness testing was performed on cross-sections of the samples. Square coupons of material were printed and sintered under identical conditions as the fatigue samples, and subjected to identical mechanical grinding. The samples were then sectioned using a low-speed diamond saw (Allied TechCut 4). The cross-section was ground (240-1200 grit SiC grinding paper) and polished (using first 1.0 μm and then 0.5 μm alumina particles). Then, the cross-section surfaces were subjected to Vickers microhardness testing using a Leco LM 800 Microhardness Tester under 25 and 50 gf loads with a dwell time of 10 s. The lines of testing were performed at angles of 5° and 15° with respect to the original surface in order to improve depth resolution. Crystallography parameters were identified using an x-ray diffractometer with Cu–Kα radiation (λ = 1.54 Å, 40 kV, 40 mA) with a step of 0.02°, a scan speed of 0.5 s/step and 2θ ranging from 35° to 95° at room temperature.

5.3 KINETIC STUDIES

Nitrogen gas-atomized alloy 625 powder was supplied by Carpenter Technology Corporation with the chemical compositions as given in [33]. Powder was sieved using a WS Tyler Ro-Tap shaker (model RX-29). A series of USA Standard Test Sieves (ASTM E-11 standard) Fisher brand were used to sieve the powders with the following meshes: 250 (63 μm), 270 (53 μm), 325 (45 μm), 400 (38 μm), 450 (32 μm), 500 (25 μm) and bottom pan (<25 μm) [54]. 10 kg of powder was sieved and then the powder caught by 53 μm sieve (powder size distribution between 53 μm and 63 μm) and the bottom pan (powder particle size below 25 μm) as well as the original powder (with size distribution of 16-63 μm) were binder jet 3D printed for study. The particle size distribution was analyzed using a Microtrac S3500 tri-laser diffraction particle analysis system via algorithms for spherical particles.

Parts were grouped according to their powder particle size distribution (PSD) in three sets including (a) between 16 and 63 μm (full range original powder), (b) below 25 μm, and (c) between 53 and 63 μm. Coupons from each set were then binder jet 3D printed using an X1-Lab printer (from ExOne Company) with the following parameters: a 100 μm layer thickness, binder saturation of 60%, spread speed of 15 mm/s, feed powder to layer thickness ratio of 2, heater power control dial set to 70% and drying time of 40 s. After printing, the green parts were cured at 200 °C in a Carbolite oven (model PF30) followed by a depowderizing step. The measured relative densities of 51.5 ± 1.1%, 45 ± 1.2% and 47.5 ± 0.7% were attained for the 16-63 μm, 16-25 μm and 53-63 μm powders, respectively.

To study densification behavior, three samples from each set were sintered in a Lindberg tube furnace under vacuum with the following heating profile: heating at 5 °C/min from room temperature to 600 °C, 3.2 °C/min to 1000 °C, 2.8 °C/min to the holding temperature (1225, 1240,

1255, 1270, 1285 or 1300 °C), holding for 4 h and then cooling at 1 °C/min to 1200 °C, 3.1 °C/min to 500 °C and finally cooling down to room temperature [52]. Additionally, a kinetic study was performed at three chosen temperatures (i.e. 1240 °C, 1270 °C and 1285 °C) over each set. Holding times varied from 0 to 12 h for each combination of conditions (PDS and temperature).

The bulk density of the differently sintered samples was measured via the Archimedes principle with an OHAUS AX324 precision balance (0.1 mg resolution). In addition, the bulk density of the sintered samples was also determined from sample cross sectional optical micrographs with ImageJ (image analysis software) [152]. For microstructural examination of the sintered coupons, cross sections were cut from the specimens, mounted, ground and polished using a Struers Tegramin-25 automatic system according to [153]. After surface preparation, samples were etched with a $HCl:HNO_3$ solution (ratio of 3) and micrographs were taken with a Keyence digital optical microscope (OM).

The parameters needed to represent the kinetics of densification and microstructure evolution of differently sintered BJ3DP gas-atomized alloy 625 samples included bulk density, apparent density (volume of solid and closed pores only), densification rate, linear shrinkage, grain size, pore size, pore separation, and the number of pores per unit area. The procedures to obtain these parameters are described as follows:

Bulk density and apparent density were measured using the Archimedes method. The mass of each sample was measured while the sample was dry (M_d). Afterwards, they were immersed in distilled water under vacuum condition for 24 h and then the mass of every sample was measured again under two different settings. The suspended weight (M_S) was measured while the sample was still immersed in distilled water while suspended and the other mass (M_i) was measured immediately after sample was taken out of distilled water (at this time, the sample was still

saturated with water but outer surfaces were quickly dried by Kim wipe to remove only the excess water). Bulk density (ρ_{bulk}) and apparent density (ρ_{app}) were expressed as follows:

$$\rho_{bulk} = \frac{M_d\,\rho_{water}}{(M_i - M_s)\rho_{theo}} \quad (5\text{-}1)$$

$$\rho_{app} = \frac{M_d\,\rho_{water}}{(M_d - M_s)\,\rho_{theo}} \quad (5\text{-}2)$$

where (ρ_{theo}) was the theoretical density of alloy 625 (here the value 8.44 g/cm^3), (ρ_{water}) was theoretical density of water (1 g/cm^3).

Another property of interest is the densification rate $\left(\frac{d\rho}{dt}\right)$ during sintering. Generally, a logarithmic function properly fits the densification data, on the relative density versus time plot, and the densification rate can be obtained using the following equation:

$$\frac{d\rho}{dt} = a\,exp\left(\frac{\rho_1 - \rho}{a}\right) \quad (5\text{-}3)$$

where ρ is the relative density (g/cm^3), a is the slope of the relative density versus log time in hour, t is time (h), and ρ_1 is the relative density at time equal to 1 h.

Linear shrinkage $\left(\frac{\delta L}{L}\right)$ in each direction was calculated based on the dimensional variation after each sintering experiment. Average pore separation, pore intercept and grain size were measured from the optical micrographs. Parallel test lines were drawn horizontally on each image taken at five randomly picked locations from each sample. The number of two kinds of intersection points were counted, i.e. solid-vapor interface and solid-solid interface. The fractional length of test line through the pore phase L_L^P was measured, and then, Solid length fraction L_L^S was calculated according to the following equation:

$$L_L^S = 1 - \frac{\sum L_L^P}{L.N} \quad (5\text{-}4)$$

where L was the whole length of each line and N was the number of lines on each image.

Then, it is assumed that the optical micrographs are representative of the whole sample, $V_V^P \approx L_L^P$ [155]. The number of solid-vapor interface intersection points per unit length on each line was defined as P_L^{SV} and the number of solid-solid interface intersection points per unit length was defined as P_L^{SS}. Thus, the surface area per unit volume of pore perimeter (S_V^{SV}) and grain boundary (S_V^{SS}) can be calculated as follow:

$$S_v = 2P_L \tag{5-5}$$

where P_L is the number of intercepts per unit length of test line. Here, it is assumed that all pores are located on grain boundaries. The average grain intercept length (λ_G, the average distance in the solid phase between any types of boundary), average pore separation (λ_{PS}, the average distance in the solid between pore boundaries) and pore intercept size (λ_P) can be calculated from the following relations [156,157]:

$$\lambda_G = \frac{4\,L_L^S}{S_V^{SV}+2\,S_V^{SS}} \tag{5-6}$$

$$\lambda_{PS} = \frac{4\,L_L^S}{S_V^{SV}} \tag{5-7}$$

$$\lambda_P = \frac{4\,(1-L_L^S)}{S_V^{SV}} \tag{5-8}$$

Three dimensionless microstructural parameters including the intercept ratio (Λ, the mean grain intercept length to mean pore intercept length ratio), surface area ratio (ψ, the ratio of the surface areas of solid/solid to solid/vapor boundaries) and the mean pore spacing to mean grain intercept length ratio (Σ) are calculated from the following relations [157,158]:

$$\Lambda = \frac{\lambda_G}{\lambda_P} \tag{5-9}$$

$$\Psi = \frac{S_V^{SS}}{S_V^{SV}} \tag{5-10}$$

$$\Sigma = \frac{\lambda_{PS}}{\lambda_G} \tag{5-11}$$

Finally, solid volume fraction and the number of pores per unit area are measured by using a digital micrographs software named ImageJ to create binary (black and white) images. To measure the number of pores per unit area, 2D images are used and number of pores are counted. It is necessary to point out that it is possible that on a 3D image, few pores are connected to each other while they are counted separately on 2D micrograph. Thus the reported number of pore per unit area represent number of pore sections on 2D images.

6.0 RESULTS AND DISCUSSION

6.1 BJ3DP OF WATER AND GAS ATOMIZED ALLOY 625

6.1.1 Powder feedstock characterizations

Powder particle micrographs showed irregular WA and spherical GA powder particles (Figure 29). Both types of particles had a dendritic microstructure typical for rapid solidification. µCT scans of as-received powders shown in Figure 29c and 1f confirm the SEM-observed powder particle morphology (irregular WA, spherical GA particles) and, additionally, revealed porosity within powder particles. Internal porosity that forms during rapid solidification in the powder atomization process was also seen in cross-sectional SEM micrographs (Figure 29b and 15e).

Chemical compositions (as provided by manufacturer and as measured with EDS, Table 1) are all close to nominal alloy 625 composition. The main differences between the powder types were morphology, carbon and oxygen impurity content which was higher in WA (1.90 and 0.09 wt.%) vs GA powder (0.04 and 0.01 wt.%, Table 1), and the average powder size and particle size distribution – GA (32.0 µm, 18.6 - 44.2 µm) and WA (34.5 µm, 17.6 - 53.6 µm), Figure 30a.

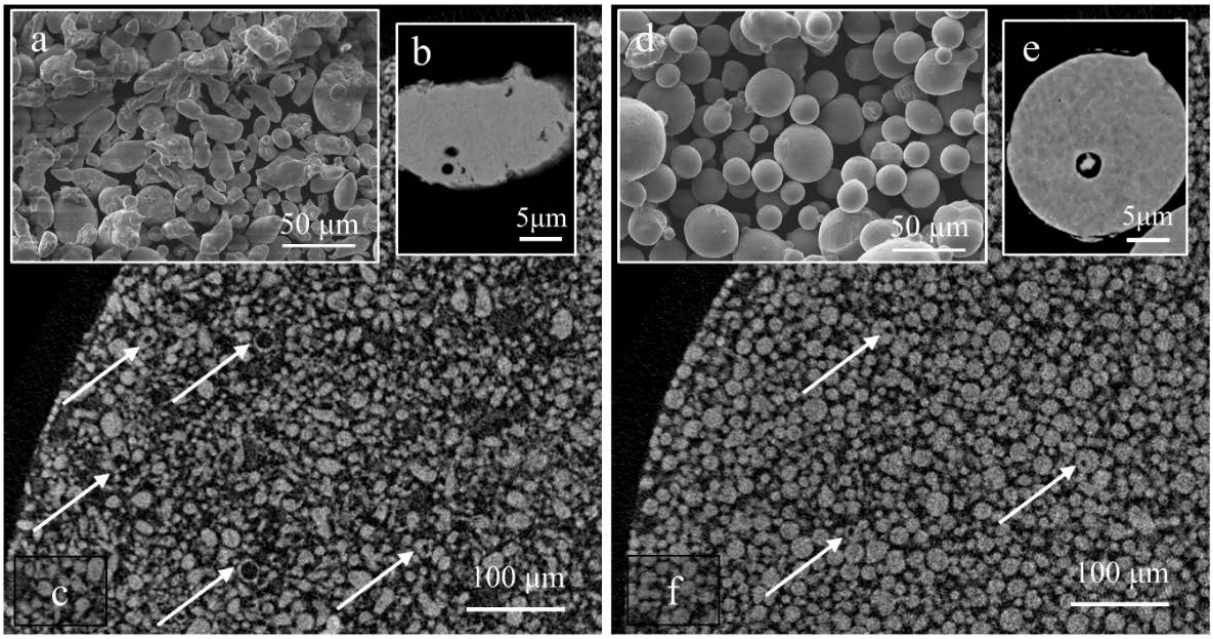

Figure 29. Powders characterization: SEM micrographs of nickel-based alloy 625 powders: (a) WA powder and (d) GA powder. SEM cross sectional micrographs taken from the (b) WA and (e) GA powders showing pores inside the atomized powders. µCT scans of the as-received nickel-based alloy 625 powders contained in a plastic straw (c) WA and (f) GA.

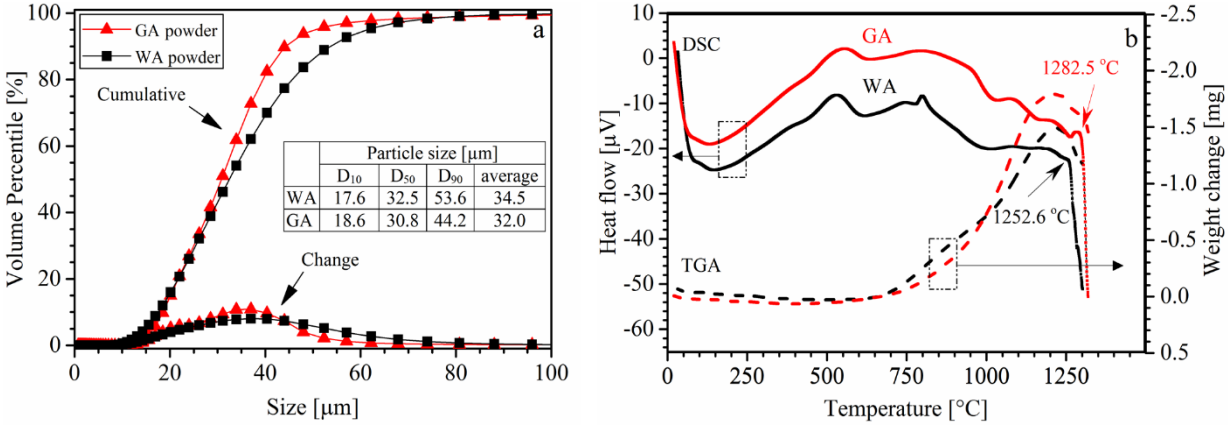

Figure 30. (a) Particle size distribution and (b) DSC and TGA curves of WA and GA alloy 625 powders.

DSC analysis of phase transformations of the powders (Figure 30b) identified the WA and GA powder solidus temperatures at 1253 °C and 1283 °C, respectively. The melting of WA powder began at 1253 °C and ended at 1305 °C, which was lower than the range of reported values of cast alloy 625 materials between 1290 and 1350 °C [159]. However, melting of the GA powder began at 1283 °C and ended at 1323 °C, which was within the reported range [159] and close to the solidus of 1294 °C for alloy 625 powder [160]. The differences between reported and measured solidus and liquidus temperatures were due to: (1) difference in chemical composition (including oxygen and carbon), (2) difference in median particle size [49] and (3) lower specific surface energy of bulk samples resulting in higher solidus and liquidus temperatures of cast material [105]. Considering the measured transformation temperatures, the sintering temperature range was selected to be 1225-1300 °C, covering low density to liquid phase sintering. Subtle peaks in the TGA heating curves of the WA and GA powders can indicate dissolution of γ'' phase and carbides during the heating process, as reported by Zhang et al. [49]. Since no peaks were observed for as-received GA powder, γ'' phase and carbide precipitates were small or non-existent; however, there was a small peak on the TGA curve of the WA powder at about 1100 °C suggesting dissolution of carbides/Laves or even thin oxide layer on the outer surface of the WA powder in the matrix and consequently a eutectic reaction.

6.1.2 Shrinkage and relative density measurements

Figure 31 shows µCT cross sectional images of WA and GA green parts with densities of ~50% and 60%, respectively. Lower density in the parallel lines indicate an irregular powder distribution in printing direction. Immersion tests of green samples showed 42% (WA) and 55% (GA) overall densities, similar to the µCT results.

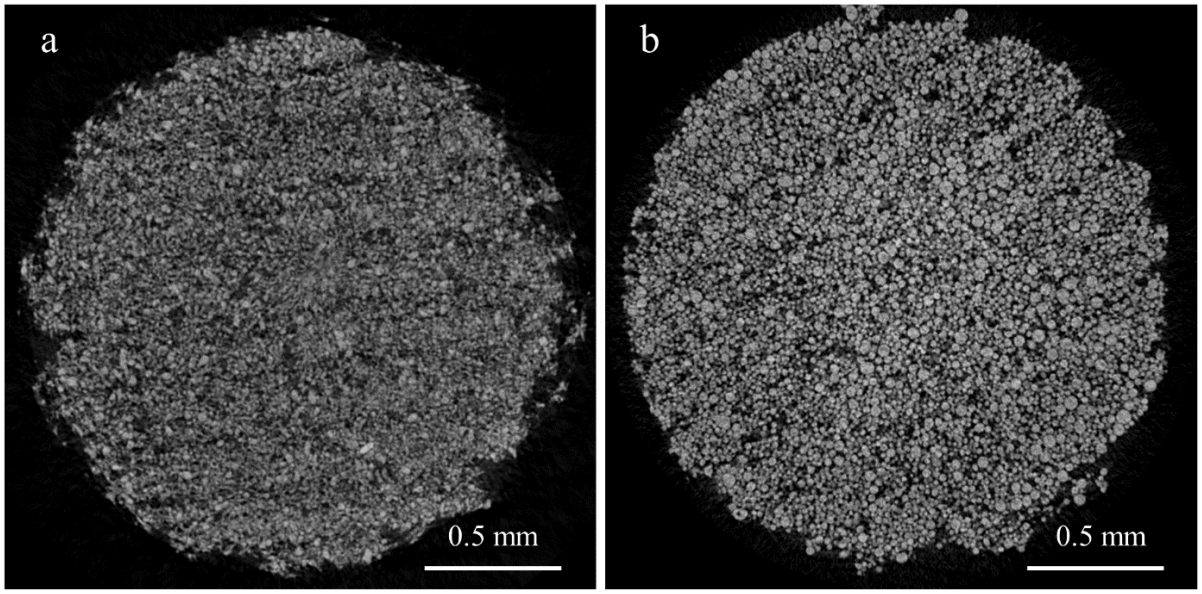

Figure 31. µCT images of the as-printed, alloy 625 powder sample (a) WA powders and (b) GA powder.

The volume changes for different sintering temperatures showed that WA samples shrunk more than GA samples sintered at the same temperature (Figure 32a). Sintered at 1225 °C, WA samples shrunk 47%, GA samples 27%. Maximum shrinkage was reached at 1285 °C and above, resulting in 46% (GA) and 57% (WA) shrinkage, which is similar to the reported ~46% (or 18% dimensional reduction) for BJP argon GA alloy 625 sintered to 99.0 ± 0.6 % density [52] and 20% dimensional reduction for BJP alloy 718 for optimum sintering to 98.5% density [113]. The main reason for the difference between WA and GA samples is the difference in powder morphology which results in 10% higher as-printed (green) densities of GA vs. WA parts.

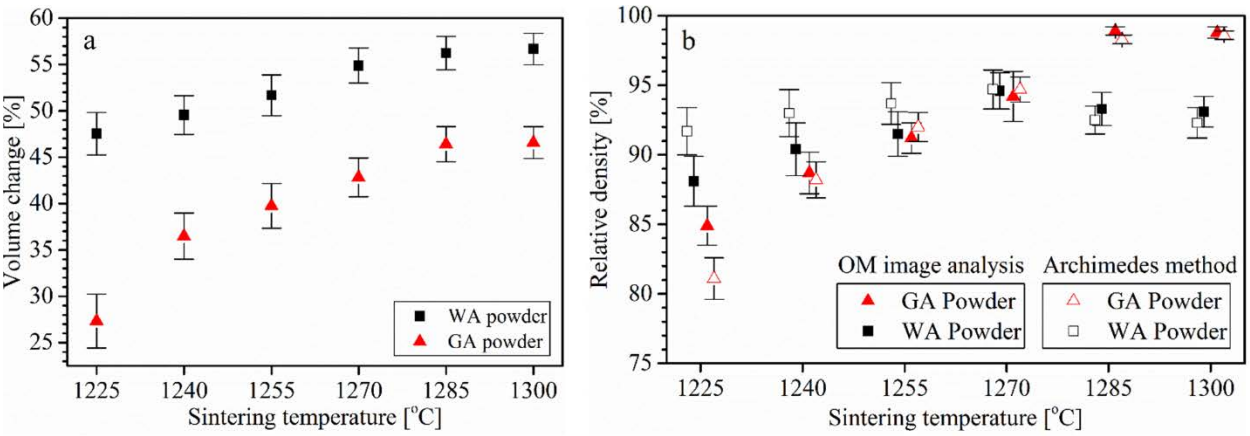

Figure 32. (a) Average shrinkage values of the WA and GA nickel-based alloy 625 sintered samples depending on sintering temperature. (b) Relative density of the GA and WA nickel-based alloy 625 samples based on the optical micrograph analysis using ImageJ software and Archimedes method. Data points are staggered at each temperature for better readability even though sample sets were sintered at the indicated temperatures (e.g. 1225 °C).

Figure 32b shows densification curves of WA and GA sintered samples analyzed with OM ImageJ image analysis and Archimedes' water displacement methods [152]. WA samples sintered at 1270 °C reached a maximum relative density of 95%, GA samples sintered at ≥ 1285 °C achieved > 99%. Between 1225 and 1270 °C, the density for both WA and GA samples increased, with WA samples denser than GA by 0.04-0.25 g/cm^3 (Figure 32b). The same trend was seen in OM image analysis results (Figure 32b). WA powder particles have more contact area which facilitates their sintering behavior compared to spherical powder particles (e.g. GA powder). Additionally, the higher density in WA samples was probably partially due to the lower solidus temperature of WA compared to GA powder (see Figure 30b). There was also a slope change on the TGA curve of the WA powder (Figure 2b) at temperatures between 750 °C and 1100 °C suggesting a dissolution of carbides/Laves (or probably oxide) in the matrix and consequently a eutectic reaction which would lower the melting temperature as well [1,9]. Therefore, liquid phase

sintering was active for WA samples sintered at 1255 °C and 1270 °C. After sintering at 1270 °C, the relative density of WA and GA samples was close to 95%. With sintering > 1270 °C, GA powder samples densified more while WA sample density dropped slightly. The WA density decrease was caused by surface melting, causing low density alumina to adhere to the powder surface, as seen in Figure 3b. Since the solidus temperature of GA powder was 1283 °C, liquid phase sintering was active during sintering > 1283 °C with a maximum GA sample density of 99.2%.

Particle sizes and size distributions were similar for WA and GA powders, as were the BJP, curing and sintering processes of the WA and GA samples. Therefore, differences in the densification are attributed to powder chemistry and powder morphology. µCT scans of as-printed samples revealed that parts printed with the irregular-shaped WA powder resulted in a ~10% lower green density parts than parts printed with spherical-shaped GA powder. Powder injection molded alloy 625 parts with an average powder particle size of 11.1 µm sintered at 1300 °C/3 h resulted in 98% density [8, 20]. In a previous study [52] on vacuum-melted argon atomized powder (compared to nitrogen atomized powder in this study), we found that although the average particle size was 33.2 µm, high relative density of about 99.0 ± 0.6 % was reached in sintered (1280 °C/4 h) BJP samples. That high density may be attributed to better density in the green part and an optimized sintering temperature. Moreover, the oxygen concentration in WA powder was higher than in GA powder (see Table 1), likely due to the H_2O used during powder atomization. Oxides formed within and on powder particles and inhibited full densification of WA samples, similarly to sintering of WA alloy 316L stainless steel [47]. Oxygen concentration of the WA powder (1.43 wt.-%) was considerably higher than in GA powders (0.28 wt.-%) (Table 1). It is thought that the trapped water molecules within the closed pores in the WA powder as well as the presence of a

thin layer of contamination (such as oxides) on the surface of the WA powder influence the densification behavior which leads to lower relative density. Besides, one may consider lower relative density in WA samples sintered at 1285 °C and 1300 °C due to the formation of higher liquid content compared to GA samples at the same sintering temperatures. The higher amount of liquid in WA samples results in a larger expansion in WA samples due to the lower density of liquid compared to solid powder. During cooling, more shrinkage takes place in the samples with a higher amount of liquid which leads to the formation of voids at boundaries. SEM and μCT micrographs taken from powder particles (Figure 1) revealed that the WA sample possessed higher residual porosity and larger pore sizes than the GA sample. To conclude, the lower packing density, the thin oxide layer on the outer surface of the powder, higher liquid phase formation during sintering of WA powder and the broader pore size distribution result in weak bonding of powder particles and in the lower relative density of the sintered WA powder BJP samples [47,49,162].

6.1.3 Microstructural observations

OM micrographs of shape, size, and distribution of grains and porosity of differently sintered samples (Figure 33 (WA) and Figure 34 (GA), Table 2) show that pores were present in WA BJP samples at all sintering temperatures. Since the solidus temperature of WA powder was 1253 °C, sintering at ≥ 1255 °C led to higher segregation of alloying elements at grain boundaries (see Figure 33 d-f) since super-solidus liquid phase sintering was active. The variation in grain and pore sizes are given in Table 2. Samples sintered at 1225 °C had grain sizes of 80 ± 25 μm, and at sintering temperature of 1300 °C, grain sizes were 94 ± 27 μm. The pore size/area increased slightly for WA samples with increasing temperature, while porosity was reduced.

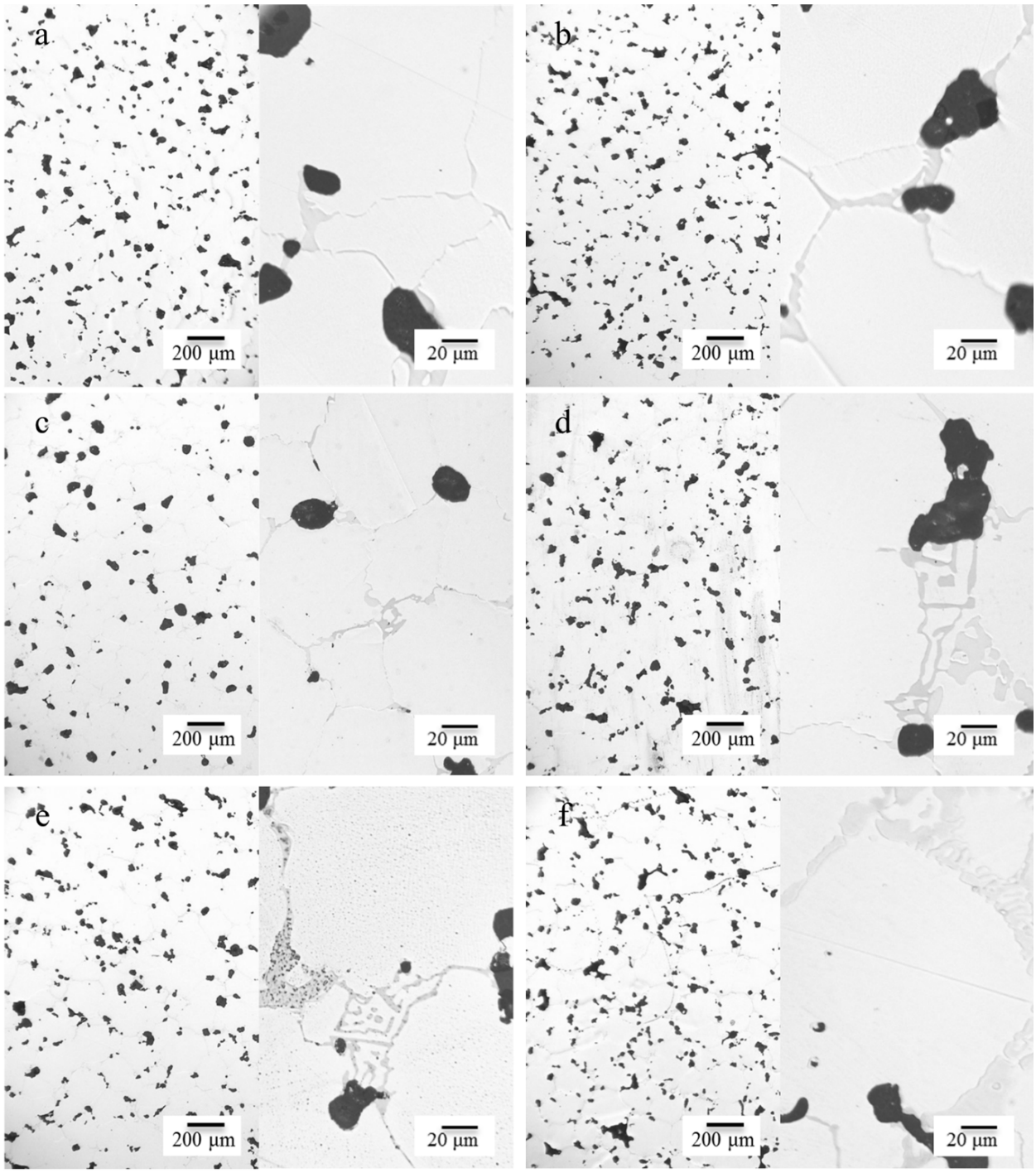

Figure 33. Optical microstructure of the WA nickel-based alloy 625 samples sintered at (a) 1225 °C, (b) 1240 °C, (c) 1255°C, (d) 1270 °C, (e) 1285 °C, and (f) 1300 °C for 4 h.

Table 2. Grain and pore size analysis and microhardness values of the WA and GA powder alloy 625 sintered samples depending on sintering temperature.

Sintering temperature [°C]	Grain size [μm]				Pore size [μm]		Microhardness [$HV_{0.1}$]	
	GA		WA					
	ImageJ analysis	ASTM E-112-13	ImageJ analysis	ASTM E-112-13	GA	WA	GA	WA
1225	39 ± 4	5.5-6.5	80 ± 25	3.5-5.5	41 ± 18	20 ± 7	160 ± 15	149 ± 12
1240	45 ± 11	5.0-6.5	83 ± 25	3.5-5.0	36 ± 10	20 ± 6	184 ± 13	163 ± 11
1255	62 ± 20	4.5-6.0	86 ± 25	3.0-5.0	27 ± 13	20 ± 7	192 ± 7	183 ± 7
1270	69 ± 23	4.0-5.5	88 ± 26	3.0-5.0	20 ± 4	21 ± 9	197 ± 8	191 ± 7
1285	89 ± 21	3.5-4.5	91 ± 26	3.0-4.5	4.5 ± 1.2	22 ± 11	213 ± 6	174 ± 9
1300	106 ± 27	2.5-3.5	94 ± 27	3.0-4.5	2.6 ± 0.4	23 ± 10	201 ± 6	170 ± 7

The microstructure of sintered GA samples (Figure 34) revealed a progression from irregular pores along particle boundaries to spherical pores within grains and at grain boundaries, as well as an increase in grain size. GA samples sintered at 1225 °C were porous and partially connected, indicating sub-optimal sintering temperature. Two pore types were present: large pores at grain boundaries and small pores within grains. The latter probably originated from pores within powder particles that were unable to annihilate or join larger pores. Increasing the sintering temperature resulted in pore reduction and an increase in sample density. Additionally, pores were no longer connected, which may have led to the improved mechanical properties [13,20]. Since the solidus temperature of the GA powder was 1283 °C, sintering at ≥ 1285 °C activates super solidus liquid phase sintering. OM micrographs of samples sintered at 1285 °C and 1300 °C for 4 h (producing the two highest relative densities), showed decreased pore size and number. The GA sample sintered at 1300 °C displayed consolidation and elemental segregation at grain boundaries due to liquid phase sintering. Sintering at ≥ 1270 °C resulted in equiaxed grains similar to previous reports [10]. Average grain and pore sizes are given in Table 2, with the highest density GA grain size of 89 ± 21 μm and average pore size of 5 ± 2 μm.

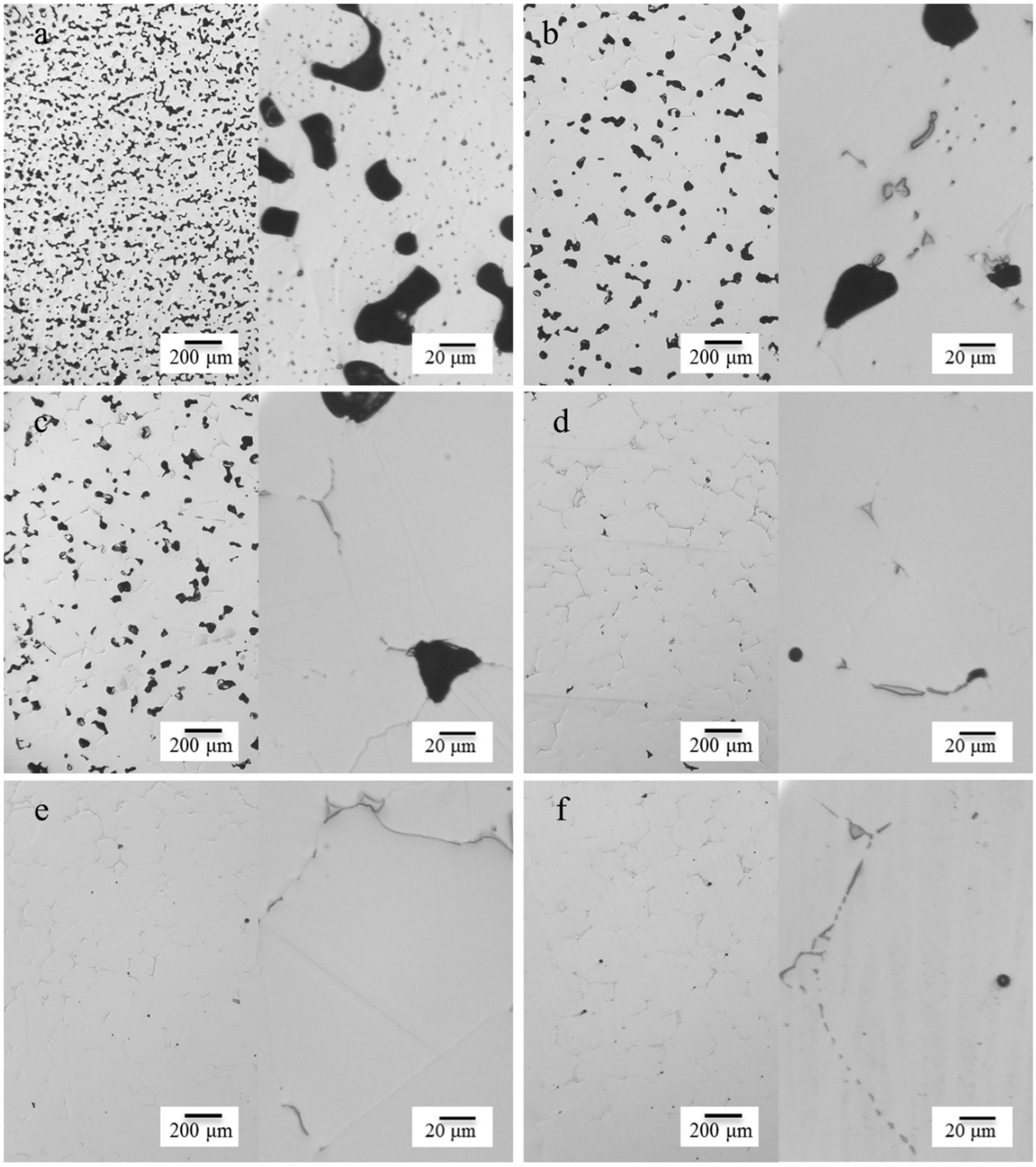

Figure 34. Optical microstructure of the GA nickel-based alloy 625 samples sintered at (a) 1225 °C, (b) 1240 °C, (c) 1255°C, (d) 1270 °C, (e) 1285 °C, and (f) 1300 °C for 4 h.

SEM micrographs of sintered WA samples for microstructural and morphological evolutions are shown in Figure 35a-d. Sintered at 1225 °C, many pores was observed (Figure 35a). Bright precipitates at grain boundaries were identified as carbide precipitates mainly along grain boundaries, which proved the formation of a liquid phase during sintering. As the sintering temperature increased to 1300 °C, pores were still present and precipitates increased along grain boundaries. SEM micrograph (Figure 36a) and EDS results (Table 3) of the 1300 °C WA samples revealed that the bright areas (point 2) were mainly composed of Nb, Mo and C, suggesting MC carbide formation. Elemental segregation and a relatively high level of absorbed oxygen resulted in the formation of surface oxides and preferential precipitation at prior particle boundaries along grain boundaries, inhibiting densification of the WA samples - since solid-state element diffusion and grain boundary migration were hindered by surface oxides [4,49]. The carbon segregation at grain boundaries also provided nucleation sites for film-like MC and M_6C.

SEM micrographs of GA samples sintered at various temperatures are shown in Figure 35e-h. As sintering temperature was increased from 1225 °C to 1300 °C, porosity and pore sizes of GA samples decreased and density increased from 85.0% to 99.2%. The pores were removed through diffusion and capillary bonds between particles in contact. EDS analysis of the GA sample sintered at 1300 °C (Figure 36b, summarized in Table 3) indicated the concentration of Mo, Nb, Ni and C is higher in lighter areas (mostly at grain boundaries) compared to the matrix. The carbides formed in the sintered specimens were primary MC carbides [52], with a complex chemical composition including C, Cr, Mo, Nb and Ni. These carbides originate from the liquid phase. Due to the relatively high content of C, Cr, Mo and Nb in alloy 625, there is a high tendency of these elements to segregate to grain boundaries, facilitating the preferential formation of liquid phase. An increase in C and Nb besides Mo, Ni and Cr at points 4 and 5 suggests carbides such as

MC and $M_{23}C_6$. The higher concentration of Mo at point 6 suggests Mo segregation at grain boundary triple points and that these points may be a target for carbide formation (M_6C). Point 3 in Figure 36b showed a composition close to that of alloy 625, representing the matrix.

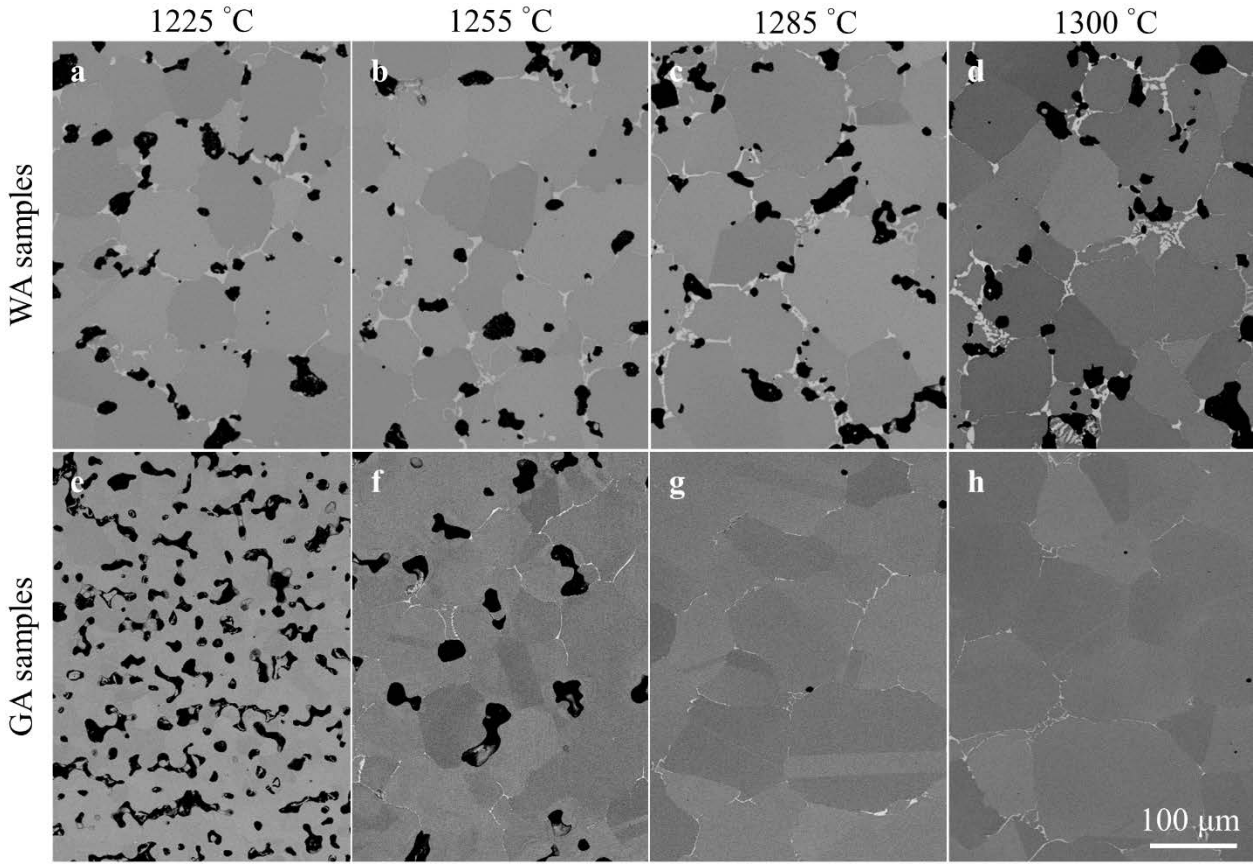

Figure 35. SEM micrographs of the WA nickel-based alloy 625 samples sintered at (a) 1225 °C, (b) 1255°C, (c) 1285 °C, and (d) 1300 °C for 4 h. SEM micrographs of the GA nickel-based alloy 625 samples sintered at (e) 1225 °C, (f) 1255°C, (g) 1285 °C, and (h) 1300 °C for 4 h.

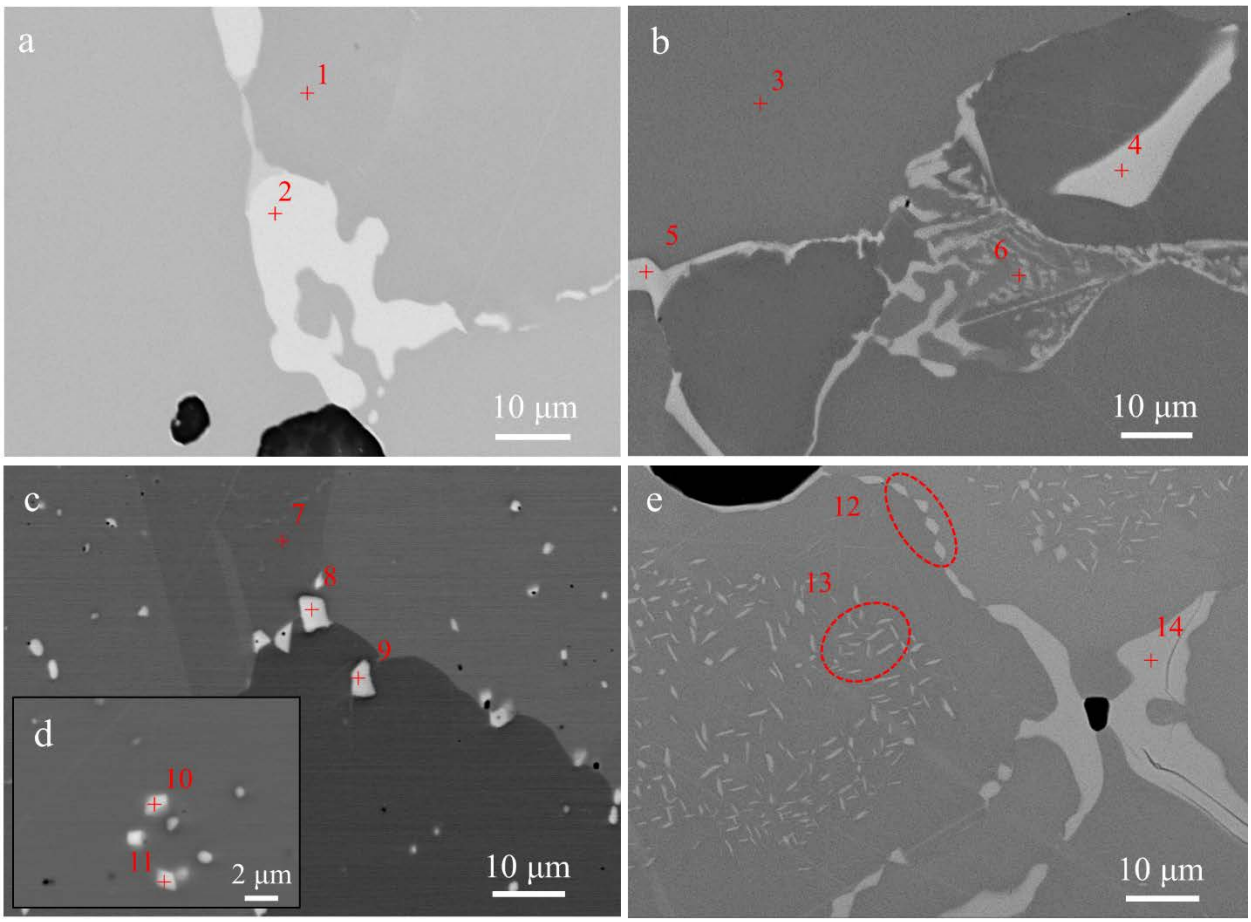

Figure 36. SEM micrographs with corresponding EDS point analysis taken from the (a) WA and (b) GA samples sintered at 1300 °C. (c,d) SEM micrographs of a GA sample sintered at 1285 °C for 4 h and then aged at 745 °C for 20 h. (e) SEM micrographs of a WA sample sintered at 1270 °C for 4 h and then aged at 745 °C for 20 h.

Figure 36c shows ***SEM micrographs of sintered and aged GA samples*** with light-grey precipitates within grains and at grain boundaries (Figure 36d, EDS results summarized in Table 3). EDS results showed that point 7 has nearly nominal alloy 625 composition, representing the matrix. Higher concentration of C, Mn and Nb in bright areas suggests carbide formation. The refractory elements Nb and Mo in alloy 625 have important roles in the development of improved strength by solid solution and precipitation formation. Therefore, small composition changes

influence the precipitation kinetics and stability of the different phases in the matrix [25,108]. Ni_3Nb precipitation in alloy 625 during aging also results in higher strength [25]. In this study, aged samples formed two kinds of precipitates: at the grain boundaries, mainly composed of Mo, Nb and C and 2.5-4.0 µm in size (points 8 and 9 in Figure 36c); within grains, mainly composed of C, Nb, Mo, Cr and Ni and 0.5-1.0 µm in size (points 10 and 11 in Figure 36d). These precipitates were identified as MC and $M_{23}C_6$ carbides based on morphology and chemistry. Elemental mapping revealed an increased amount of oxygen in the carbide precipitates, agreeing with the reported preferential oxidation of MC and $M_{23}C_6$ type carbides at high temperature [163]. An ***SEM micrograph of a sintered and aged WA*** sample shows various precipitates (Figure 36e): (1) white precipitates at grains boundaries (point 14) mainly composed of Ni, Mo, Cr and C and a high amount of strong carbide forming elements (Ni, Mo, Cr) in the MC type carbide (as high as 87.6%); (2) area 12 with oval shaped precipitates at the grain boundary with Ni, Mo, Cr elements indicating $M_6C/MC/M_{23}C_6$ carbides or Laves; (3) precipitates within grains (area 13) with mainly Ni, Mo and Cr elements suggesting $M_6C/MC/M_{23}C_6$ carbides or Laves.

Table 3. Chemical composition in wt.-% of the selected points on SEM micrographs in Figure 36.

	Selected area for EDS point analysis													
	1	2	3	4	5	6	7	8	9	10	11	12	13	14
C	0	11.7	0	2.3	1.4	0.1	0	27.6	31.4	39.1	33.5	12.9	13.1	12.4
O	0	3.4	0	0.9	0.7	0.1	0	2.6	1.5	1.0	1.8	1.7	2.9	3.2
Mo	8.2	32.1	10.5	38.4	36.1	17.3	0.8	35.3	32.8	14.6	11.7	35.2	20.7	31.4
Nb	3.1	5.4	3.6	31.6	4.8	2.3	3.2	25.9	28.7	37.7	34.0	5.2	2.8	4.7
Ni	64.2	37.9	61.7	2.7	32.9	55.7	65.4	4.3	3.2	3.0	6.2	35.9	50.6	40.3
Cr	21.4	7.4	21.5	23.0	22.6	22.2	20.1	2.8	1.5	3.1	11.8	7.8	7.7	6.9
Mn	0.4	0.4	0	0.1	0.1	0.1	0.3	1.0	0.4	0.2	0.3	0.2	0.7	0.3
Fe	2.7	1.7	2.7	1.0	1.4	2.2	0.3	0.9	0.5	1.3	0.7	1.1	1.5	0.8

6.1.4 XRD analyses and phase formation

XRD of as-received, sintered and aged WA and GA powders (Figure 37) show major (51°, 60°, 90°, 111°), and minor peaks (34.6°, 42. 4°, 46.5°, 48.5°, 51°, 56.5°). At all processing stages, the main peaks were γ-Ni phase peaks (fcc, [52]) and small peaks were chromium oxides and carbides. Due to the small number of intermetallic phases, e.g. γ'' (Ni_3Nb, bct) and δ (Ni_3Nb, orthorhombic), and peaks partially overlapping with γ-Ni peaks, peak shift and breadth of the γ-Ni peaks were used to indirectly identify the presence of intermetallic phases [118,119]. Peak positions, resulting *d*-spacings and lattice parameters are given in Table 4. A peak shift and therefore lattice parameter shift of about 0.24% (WA) and 0.50% (GA) in the atomized powders compared to the standard alloys 625 fcc γ-Ni phase (Reference code: 98-011-6293) indicates potentially elemental Ni and Nb as well as intermetallic phases such as γ' [Ni_3(Al, Ti)], γ'' [Ni_3(Nb,)] and δ [Ni_3Nb] as well as carbides or oxides in the γ-Ni matrix precipitated during powder production. Differences might have arisen from the atomization method resulting in slightly different amounts of formed phases due to solidification speed and contamination.

In this study, furnace cooling to room temperature followed sintering. XRD patterns of samples sintered at 1225 °C indicate that carbides had enough time to form during the cooling process. In WA and GA samples, double XRD peaks were detected at around 51.5° with the left peak identified as γ-Ni phase and the right as δ [Ni_3Nb] phase. Sintering at 1300 °C, the amount of δ phase increased and resulted in an overlap of peaks. Although the sintering process was conducted in vacuum, chromium oxide (Cr_2O_3) precipitates were identified in the XRD pattern due to the high oxidation rate of alloy 625 at high temperatures [52]. However, the amount of Cr_2O_3 decreased in the samples sintered at 1300 °C. This is due to evaporation of Cr_2O_3 as CrO_3 gas above 1000 °C, with solid Cr left behind to dissolve into the matrix [6,20,26].

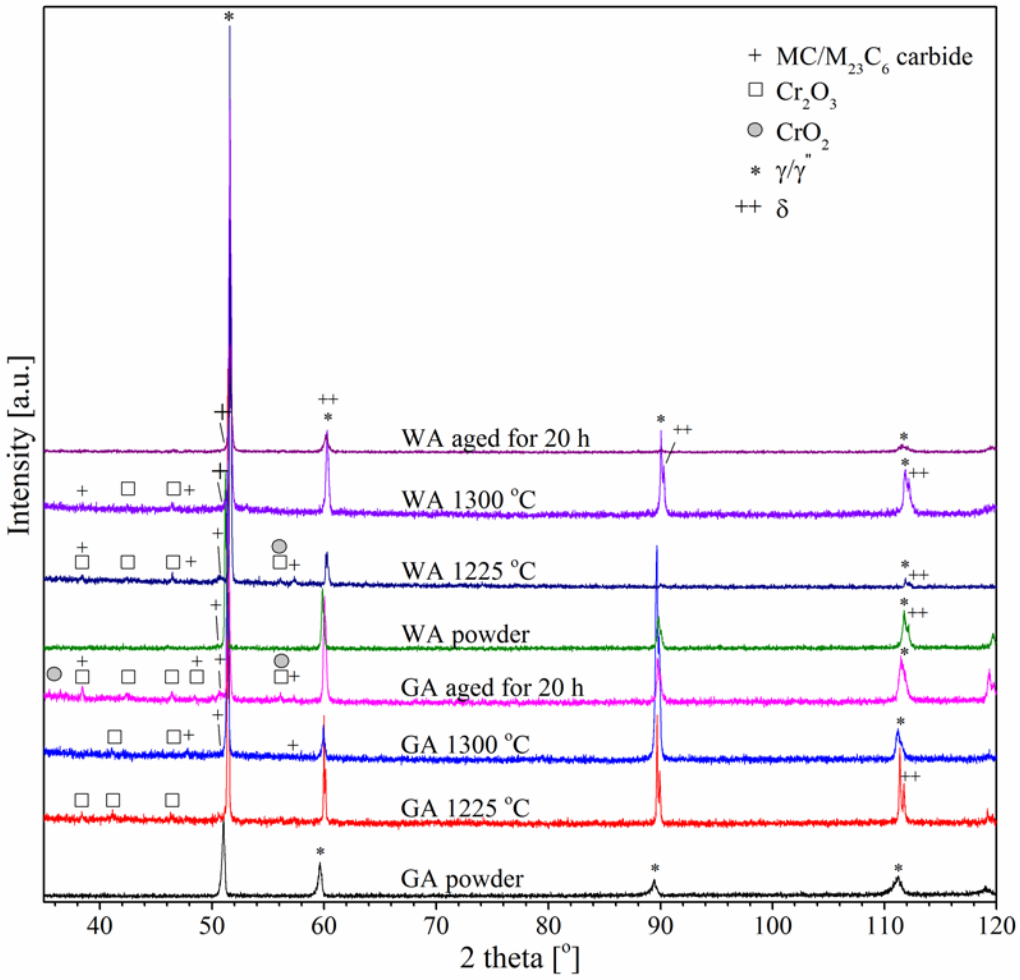

Figure 37. XRD patterns of the as-received powders and sintered WA and GA nickel-based alloy 625 samples: (a) GA powder, (b) GA sintered at 1225 °C, (c) GA sintered at 1300 °C, (d) GA aged for 20 h, (e) WA powder, (f) WA sintered at 1225 °C, (g) WA sintered at 1300 °C, (h) WA aged for 20 h.

Lattice parameters of the as-received WA and GA powders were 3.5897 Å and 3.5990 Å, and decreased after sintering to 3.5639 Å and 3.5758 Å, respectively (Table 4). As reported in [52], this decrease is attributed to the depletion of Nb, Cr and Mo in the γ-matrix, since these elements participate in the formation of carbides and intermetallic phases. Increasing sintering temperature to 1300 °C led to the disappearance of Laves/carbide and chromium oxide peaks since

at this temperature, Nb, Mo and Cr elements which participate in the formation of carbides and intermetallic compounds can dissolve in the γ-matrix. This also results in increased *d*-spacing values. The sintered and aged GA samples showed increased 2θ and, thus, smaller lattice parameters due to the depletion of alloying elements from the matrix to form precipitates. The XRD pattern of the aged samples clearly showed that the peak intensity and volume from the precipitates increased compared to only sintered samples. These results were similar to our previous study on BJP Ar gas atomized alloy 625 powders [52].

Table 4. Crystallographic parameters of the WA and GA nickel-based alloy 625 samples compared to a γ-Ni reference (ICSD Reference code: 98-011-6293).

Powder type	Samples	Peak position for crystallographic planes				*d*-spacing for (111) plane [Å]	Lattice parameter [Å]
		111	200	220	311		
WA	As-received powder	51.170	59.836	89.812	111.753	2.0725	3.5897
	Sintered at 1225 °C	51.567	60.285	89.973	111.887	2.0576	3.5639
	Sintered at 1300 °C	51.593	60.272	90.038	111.900	2.0566	3.5621
	Sintered at 1270 °C and aged at 745 °C for 20 h	51.622	60.301	90.094	111.929	2.0544	3.5583
GA	As-received powder	51.026	59.626	89.445	111.228	2.0779	3.5990
	Sintered at 1225 °C	51.382	59.983	89.684	111.362	2.0645	3.5758
	Sintered at 1300 °C	51.343	59.944	89.671	111.192	2.0660	3.5784
	Sintered at 1285 °C and aged at 745 °C for 20 h	51.409	60.022	89.736	111.467	2.0635	3.5741
γ-Ni reference		51.272	59.945	89.905	---	2.0675	3.581

6.1.5 Phase and microstructure evolution

Combining all results of differently heat-treated samples printed from gas- and water-atomized powder, we propose the following phase and microstructure evolution model, which is graphically summarized in Figure 38: At low sintering temperatures, e.g. 1225 °C/4 h, there are pores present in both GA and WA samples. GA samples have a larger density of finer pores at grain boundaries and within grains but no visible precipitation of oxides or carbides; WA samples have a smaller density of larger pores at grain boundaries, smaller pores within grains and carbide/oxide precipitates. With increasing sintering temperature, e.g. 1270 °C, there is grain growth in both WA and GA samples. Most pores within grains disappear. WA samples show some pore consolidation, but large pores remain and the carbides and oxides increase. For GA samples, all pores nearly disappear and some carbides and oxides form. After solution treatment (1150 °C/2 h) and aging (745 °C/20 h) there is no density change. WA samples have a large amount of carbides and oxides at the grain boundaries resulting in a Cr, Nb, Mo depleted zone around the grain boundaries. If grains are large enough, a large amount of small carbide particles forms in the center of the grain. GA samples on the other hand form only small carbide and oxide particles during aging within grains and at grain boundaries.

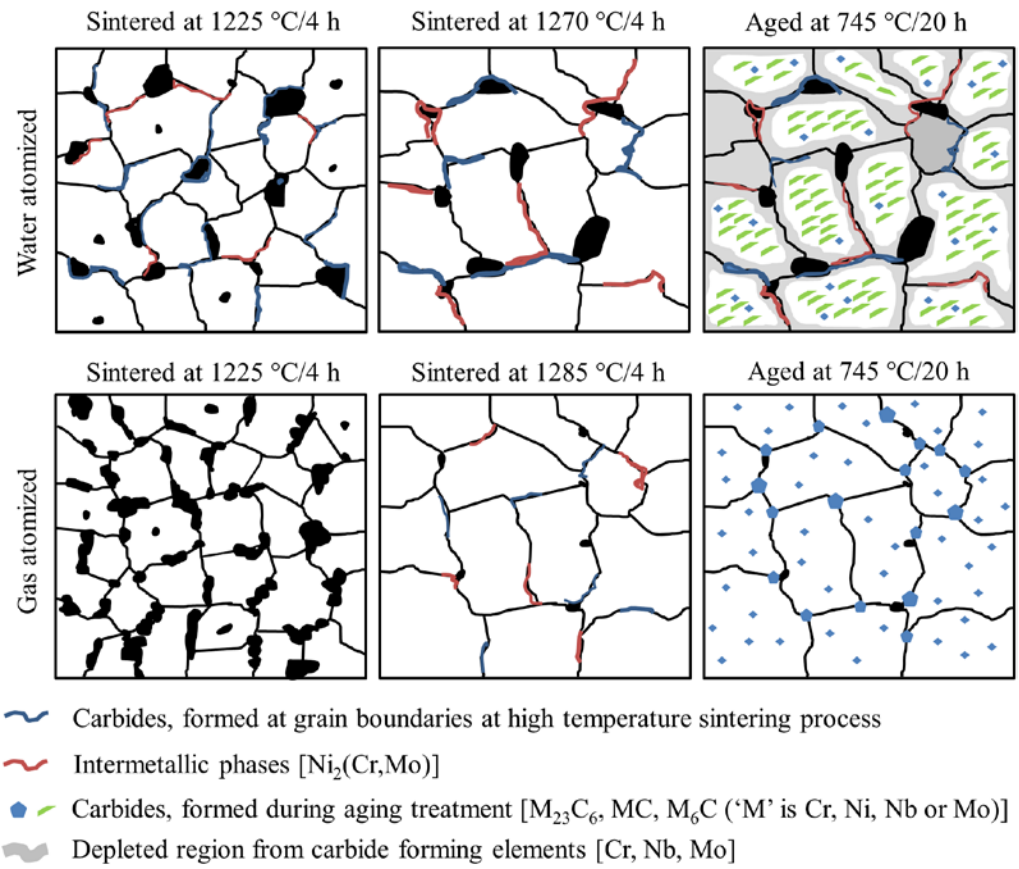

Figure 38. Schematic showing phase and microstructure evolution model for differently heat-treated BJP alloy 625 samples from gas- ad water-atomized powder.

6.1.6 Mechanical properties

Microhardness results of sintered WA samples showed that hardness increased from 149 ± 12 to 191 ± 7 $HV_{0.1}$ with sintering temperature (1225 to 1270 °C) and then decreased to 170 ± 7 $HV_{0.1}$ upon further temperature increase (Figure 39a, Table 2). In GA samples, hardness increased (similar to density) with sintering temperature to 213 ± 6 $HV_{0.1}$, up to 1285 °C. For WA and GA samples, similarly to Ar gas atomized powder samples [52], relative density and microhardness

show corresponding trends. Additionally, with increasing temperature, grain growth, coarsening and, especially at higher temperatures, segregation of alloying elements to grain boundaries occurs, resulting in decreased hardness [107,108]. A post sintering aging treatment of highest density WA and GA samples (WA: 1270 °C, GA: 1285 °C) increased hardness further to 225 ± 6 $HV_{0.1}$ (WA) and 327 ± 7 $HV_{0.1}$ (GA), most likely due to precipitate formation (Table 5).

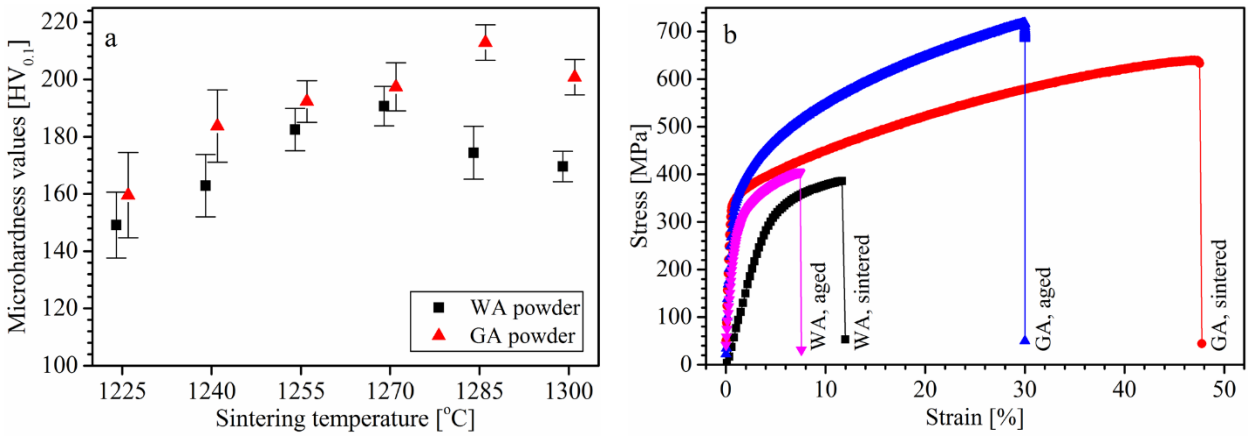

Figure 39. (a) Average microhardness values and (b) Engineering stress–strain curves of the WA and GA nickel-based alloy 625 samples sintered at different temperatures for 4 h. Data points are staggered at each temperature for better readability even though sample sets were sintered at the indicated temperatures (e.g. 1225 °C).

Tensile tests were carried out on highest density and hardness WA and GA samples sintered at 1270 °C and 1285 °C and on additionally aged samples (see (Figure 39b, Table 5). Tensile strength (386 ± 15 MPa) and ductility (~12%) of only sintered WA samples (1270 °C) were relatively low. However, only sintered GA samples (1285 °C) had higher tensile strength (644 ± 16 MPa) and ductility (~47%). The improvement in mechanical properties is mostly caused by porosity differences, and therefore, the low (GA) or high (WA) number of present pores.

Table 5. Average values of UTS, $YS_{0.2\%}$ and elongation of the BJP WA and GA nickel-based alloy 625 samples.

Samples	Yield stress [MPa]	UTS [MPa]	Elongation [%]	Microhardness [$HV_{0.1}$]
WA sample sintered at 1270 °C	287 ± 11	386 ± 15	11.6 ± 2.2	191 ± 7
GA sample sintered at 1285 °C	376 ± 14	644 ± 16	47.0 ± 2.7	213 ± 6
WA sample sintered at 1270 °C and aged at 745 °C for 20 h	298 ± 13	405 ± 14	7.5 ± 1.9	225 ± 6
GA sample sintered at 1285 °C and aged at 745 °C for 20 h	394 ± 15	718 ± 14	29.1 ± 3.1	327 ± 7
Cast alloy 625 [108]	350	710	48	200

Aging (745 °C, 20 h) on optimally sintered samples further improved mechanical properties. For WA samples, tensile strength increased 5% to 405 ± 14 MPa, yield strength to 298 ± 13 MPa, while elongation decreased to 7%. However, for GA samples, tensile strength increased 11.5% to 718 ± 14 MPa, yield strength to 394 ± 15 MPa, while elongation decreased to 29%. Based on the TTT diagram of alloy 625 [108], various phases (e.g. $M_{23}C_6$, MC, M_6C, γ', γ'', δ, Laves) form during aging between 550 and 750 °C. The advantageous phases formed during aging hinder crack growth and, thus, improve mechanical properties [108]. In general, (not applicable here, but of note) these phases also hinder grain boundary sliding at high temperature. SEM fractography showed that sintered GA samples (Figure 40a) had mostly ductile fracture dimples, with almost no micro-cracks and pores. However, the fracture surface of sintered and aged GA samples showed dimples, particle facets of precipitates (identified with EDS as carbides) and some micro-cracks that might initiate macroscopic cracks (Figure 40b). This suggests that failure of sintered GA sample had a mostly ductile character (see Figure 40a), while sintered and aged GA samples failed in a mixed mode, primarily intergranular with ductile dimple fracture in fully dense regions and

some non-ductile failure at micro-pores and precipitates. Fracture surface studies of WA samples showed mostly brittle-ductile failure. Only sintered WA samples (Figure 40c) showed small precipitates and micro-cracks, while additionally aged samples (Figure 40d) showed more precipitates (identified with EDS as carbides and probably also intermetallic phases) on the fracture surface representing crack initiation sites.

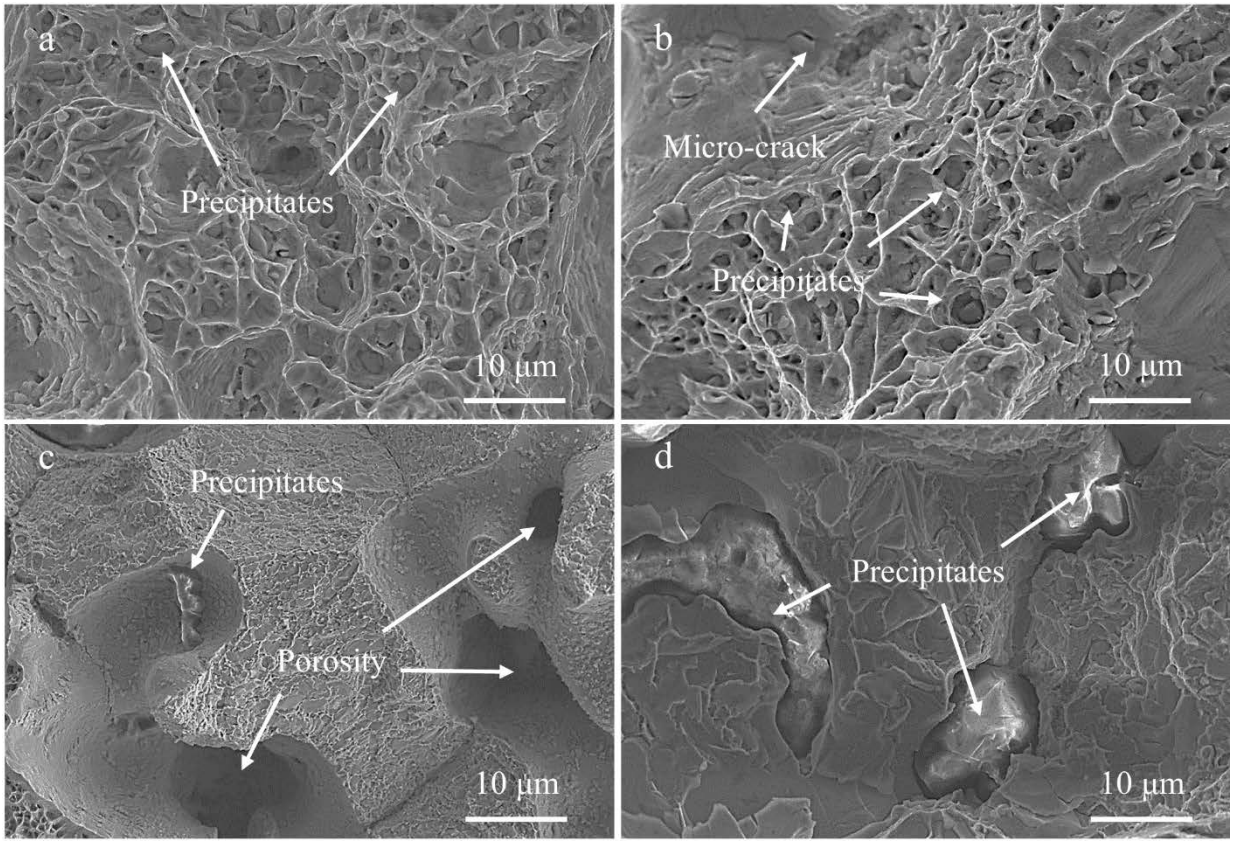

Figure 40. SEM micrograph of the fracture surface after tensile test taken from the GA sample (a) sintered at 1285 °C and then (b) aged at 745 °C for 20 h; and WA sample (c) sintered at 1270 °C and then (d) aged at 745 °C for 20 h.

6.1.7 Summary

A detailed comparative investigation was conducted on the relationship between microstructure and mechanical properties of sintered and additionally aged alloy 625 binder jet printed samples produced from water atomized (WA) and gas atomized (GA) powders with these main findings:

1. As-printed parts had green densities of 50% and 60% for WA and GA samples, respectively, due to different particle morphologies: spherical for GA, irregular-shaped for WA powder.
2. Sintering was performed on WA and GA samples from 1225 to 1300 °C for 4 h. GA samples were denser than WA samples, due to higher green density and lower oxygen content, with the highest density (99.2%) reached after sintering at 1285 °C.
3. Phase and microstructural evolution of BJP samples produced from WA and GA powder was very different. WA samples did not fully densify and formed large amounts of carbide and oxide precipitates with large Cr, Nb, and Mo depleted zones, while GA samples fully densified, showed no depletion zones and formed small amounts of fine precipitates.
4. Tensile strength, yield strength, and hardness of near-fully densified GA samples reached 644 MPa, 376 MPa, 213 $HV_{0.1}$ and increased to 718 MPa, 394 MPa, 327 $HV_{0.1}$ respectively, after aging and ductility decreased from 47% to 29%. These values are similar to those seen for cast alloy 625, while WA samples had significantly lower values. The superior GA sample values, with a good balance between tensile strength and ductility, are related to the presence of fine and equiaxed grains, near-full density, and a homogeneous distribution of composition and precipitate phases.

6.2 CHARACTERIZING SURFACE FINISH AND FATIGUE BEHAVIOR

6.2.1 Fatigue testing

Figure 41 illustrates the results of the fatigue tests for the as-printed and mechanically ground samples and compared with the cast alloy 625 (specimens were surface treated using wire electrical discharge machining (EDM) and milled to final shape) [165]. The yield strength of the cast alloy 625 was reported as 350 MPa [165] and 351 MPa for the injection molded alloy 625 [108]. In our previous study on the binder jet printed parts made from nitrogen gas atomized alloy 625 powder, the yield strength value was found to be similar at 376 MPa [33]. Therefore, the limit of 375 MPa was selected for the maximum applied stress in this study. It was seen that the as-sintered samples failed far earlier than the cast samples [165], with up to one order of magnitude fewer cycles to failure. By contrast, the mechanically ground samples had superior fatigue life compared to both the cast alloy and as-sintered samples, again by up to one order of magnitude. Further, the mechanically ground samples that were tested below 300 MPa met the runout condition (10^7 cycles) and the testing was stopped. This indicates that the performance improvement at low stresses may be even larger than is reflected in Figure 41. Further, the stress ratio (R) in the present study was -1, while the fatigue study of alloy 625 by Theriault [165] was conducted at R = 0.1. It is well known that tests performed at lower R values, and particularly negative values, result in lower fatigue life than those performed at higher R values [166]. Therefore, the performance of the present samples is even further superior to the cast alloy than is apparent in Figure 41.

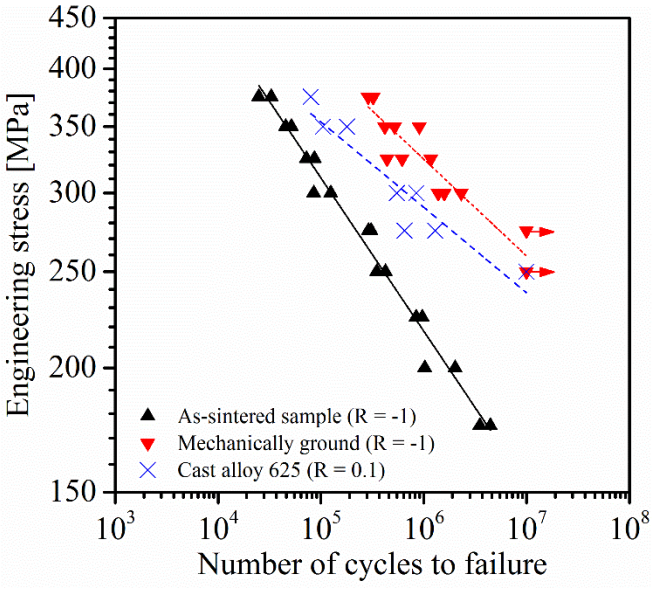

Figure 41. Fatigue life data of the BJ3DP alloy 625 for the as-printed condition (black points) and after mechanical ground (red). The horizontal arrows indicate that the runout condition of 10^7 cycles has been met and the test was stopped. For comparison, fatigue data is included from Ref. [165] for cast samples of alloy 625.

The experimental data were fit using the Basquin equation [167]:

$$\sigma_a = \sigma_f'(2N_f)^b \qquad (6\text{-}1)$$

where σ_a is the stress amplitude (which is equal to the max stress in fully-reversed loading), N_f is the number of cycles to failure, and σ_f' and b are the fatigue strength coefficient and fatigue strength exponent, respectively. All datasets are reasonably well fit ($R^2 > 0.85$) with this power-law form. The resulting fatigue strength coefficients were σ_f' = 781, 747, and 764 MPa for the as-sintered, mechanically ground, and cast materials. The resulting fatigue strength exponents are b = -0.15, -0.10, and -0.09 for the as-sintered, mechanically ground, and cast materials, respectively. For most metals, b is in the range of -0.05 to -0.12, with typical values around -0.1 [168]. For a given value of σ_f', values of b that are closer to zero indicate less dependent on stress and superior

fatigue performance. As noted, the mechanically ground samples experienced runout at low stresses and therefore were not tested to final failure. Larger values of N_f at low values of σ_a would further increase the best-fit exponent; therefore, the presently measured value of -0.10 represents lower bound on this value. Overall, Figure 41 demonstrates that the fatigue data are well fit by the Basquin equation and that the performance of the mechanically ground AM samples is superior to that of the cast and ball-milled parts.

Figure 42 illustrates SEM micrographs of the overall fracture surfaces for selected samples. Figure 42a shows the fracture surface of the as-sintered sample at the applied stress value of 175 MPa failed after 4.5×10^6 cycles with a transgranular surface area of 8.08 mm^2. By increasing the applied stress to 275 MPa, the fatigue life decreased to 3.1×10^5 cycles with the transgranular surface area of 5.48 mm^2 (Figure 42b). At 375 MPa applied stress, the fatigue life decreased further to 2.5×10^4 cycles with the transgranular surface area of 2.79 mm^2 (Figure 42c). The measured transgranular surface area clearly showed how the applied stress value affected the fracture surface as well as fracture mode. Finally, Figure 42d shows the fracture surface of a selected mechanically ground sample tested at 350 MPa, which experienced fatigue failure after 5.5×10^5 cycles and transgranular surface area of 9.50 mm^2. In all cases, the crack initiated on the surface of the samples and failure took place close to the area of the smallest diameter of the neck of the samples. No pore was seen on the micrographs indicating nearly full density of the BJ3DP parts. After crack initiation, the crack grew in a stage I crack growth mode as is indicated by the transgranular fracture surface. Stage I crack growth mainly progresses by slip plane cracking and was identified by the presence of facets at the initiation sites. Finally, the crack growth continued via intergranular fracture. The dash-line curves on the BSE-SEM micrographs show the approximate boundary between the fatigue crack initiation (transgranular crack growth) and intergranular fracture zones.

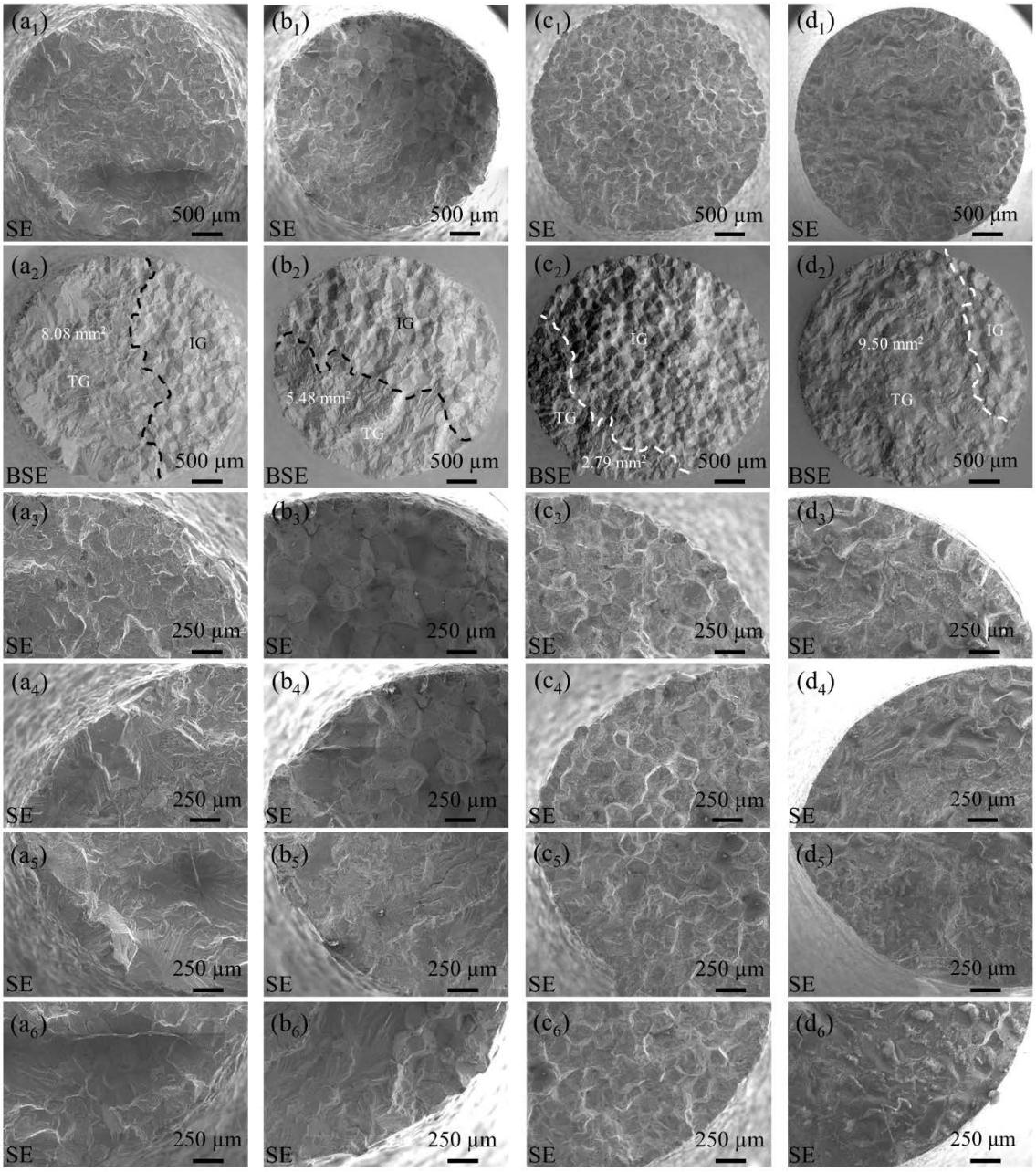

Figure 42. Fatigue fracture, crack initiation and crack growth micrographs taken from the as-sintered samples at the applied stress value of (a) 175 MPa, (b) 275 MPa and (c) 375 MPa. (d) Selected fracture surface of the mechanically ground sample at the applied stress value of 350 MPa. Two different fracture modes are shown in BSE micrographs as transgranular (TG) and intergranular (IG) fatigue fracture failures. Different magnifications indication regions with different features such as brittle and ductile fractures.

6.2.2 Materials characterization of the samples

Prior to fatigue testing, the samples were characterized using optical microscopy, stylus and optical profilometry for surface topography. Figure 43 shows optical micrographs of the external surface of the samples. In Figure 43a-a_1, printing layers (horizontal) and print direction (vertical) can be seen. After sintering (see Figure 43b-b_1), neighboring powders joined to form larger grains on the outer surface. It is seen that deep valleys are possibly present on the surface. Figure 43c-c_1 showed the sample surface after mechanical ground indicating that the surface was smoother than the as-sintered sample.

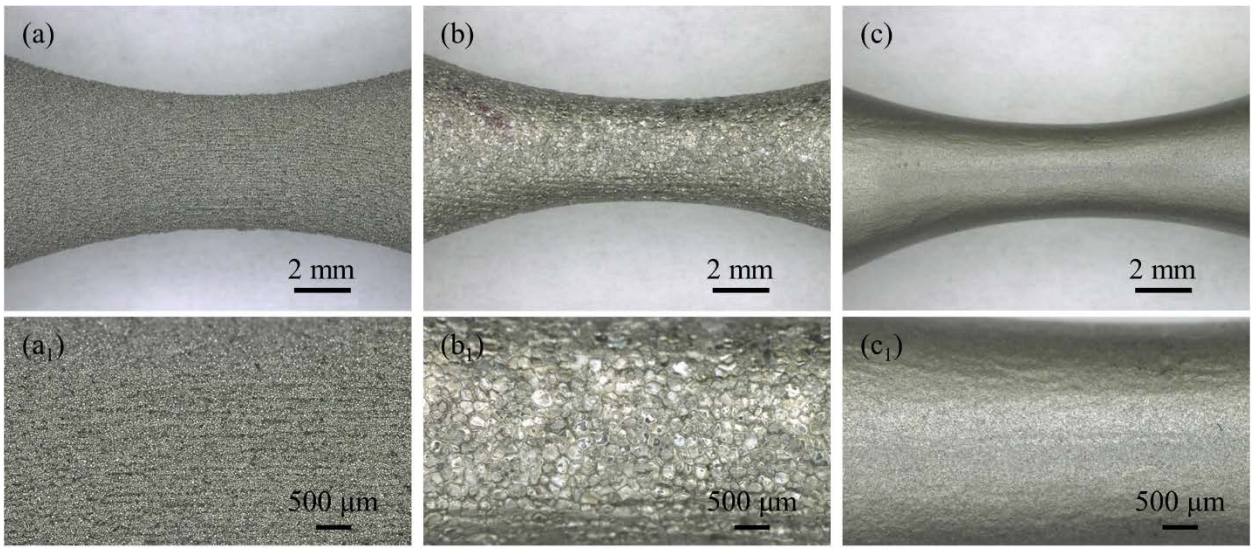

Figure 43. Optical micrographs of the external surface of the samples (a,a_1) as-printed part from gas atomized powder, (b,b_1) as-sintered, and (c,c_1) mechanically ground.

The surface topography of the as-sintered and mechanically ground samples was measured using stylus and optical profilometry, as shown in Figure 44. The extreme roughness of the as-sintered parts that was visually observable (Figure 43b) is quantified in the topography characterization. In order to quantify the variation in roughness between the different surface conditions, two different metrics were compared: the root-mean-square height variation (often called h_{rms}) and the root-mean-square roughness (often called R_q). Both are computed using the same equation, but the former is applied directly to the measured height data (after line- and parabola-compensation, see Methods) and the latter is applied to the height data after the application of a Gaussian filter to remove the larger-scale features:

$$h_{rms} = \sqrt{\frac{1}{L}\int_0^L \left(h_{unfiltered}(x)\right)^2 \, dx} \tag{6-2}$$

$$R_q = \sqrt{\frac{1}{L}\int_0^L \left(h_{filtered}(x)\right)^2 \, dx} \tag{6-3}$$

where h is the height measured at position x over a scan length of L. These are numerically implemented using the trapezoidal rule. For the filtering, a Gaussian filter with a cut-off of 80 μm was applied, in accordance with ISO 4288. Using stylus profilometry, the RMS height variation was measured as h_{rms} = 24.77 ± 5.13 μm for the as-sintered sample and was reduced to h_{rms} = 3.76 ± 1.07 μm upon mechanical grinding process. The measured values of RMS roughness were R_q = 1.39 ± 0.20 μm and R_q = 0.47 ± 0.02 μm, for the as-sintered and mechanically ground samples, respectively. Another metric used to quantify topography is average roughness (which typically scales with R_q), which was reduced upon grinding from R_a= 1.10 ± 0.16 μm to R_a = 0.38 ± 0.02 μm.

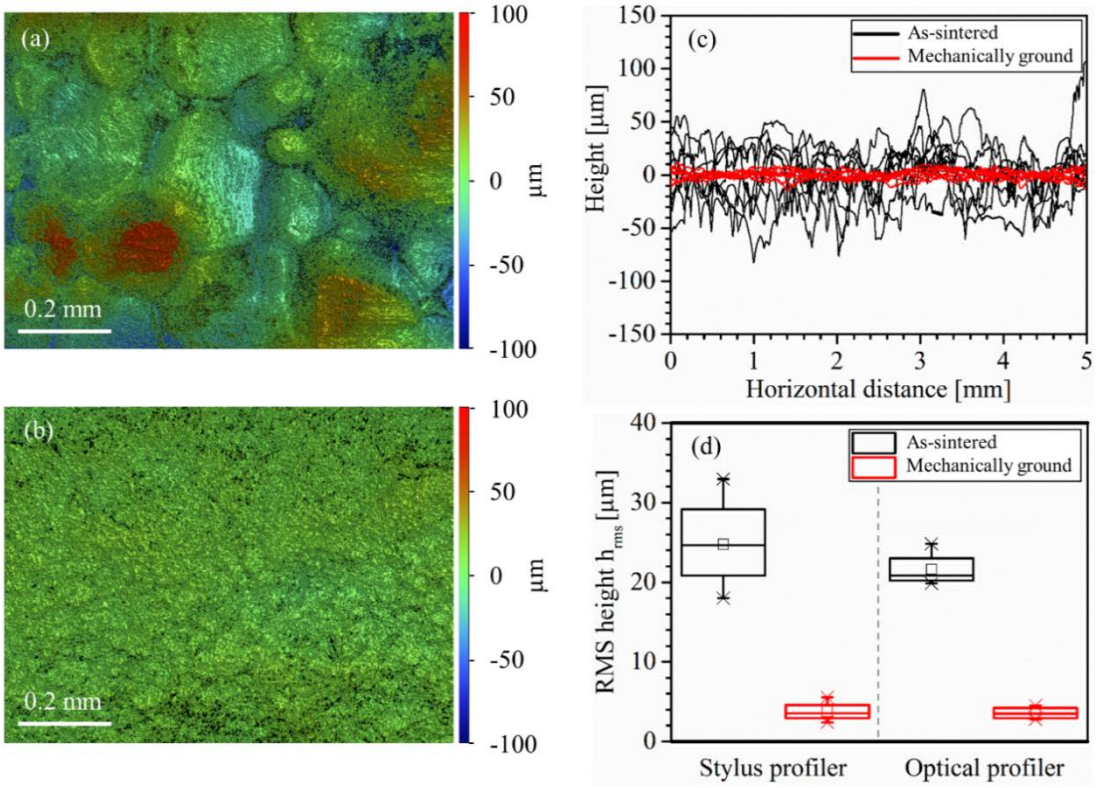

Figure 44. Optical profilometry was used to collect surface scans of the material in its (a) as-sintered and (b) and mechanically ground state. (c) Line scans of topography were collected using stylus profilometry. (d) The h_{rms} value is compared between conditions.

The same roughness parameters were computed from the optical profilometry data. The RMS height was reduced from h_{rms} = 21.61 ± 2.21 µm to 3.60 ± 0.78 µm upon mechanical grinding step. The filtered values for the as-sintered material were R_q = 12.01 ± 2.52 µm and R_a = 7.65 ± 1.58 µm; for the ground sample they were R_q = 2.78 ± 1.10 µm and R_a = 1.45 ± 0.49 µm. While these values are directly comparable between conditions using the same technique, they are not necessarily comparable between techniques. Not only does the measurement size vary between the techniques, which affects the measured values [169], but also the techniques are subject to different sources of artifacts and errors. The stylus profilometer is subject to tip-size artifacts,

which prevent sampling of deep crevices and small lateral-wavelength features. The optical profilometer is subject to interference effects, which are particularly problematic on rough samples such as these. To gain better insight on how the surface roughness may look at the curved surface for the fatigue samples, cross-sectional observations were carried out on the as-printed and mechanically ground samples and micrographs were shown in Figure 45. It was seen that the as-sintered sample has a rough surface with crevices while mechanical ground process assisted to smoothen the surface.

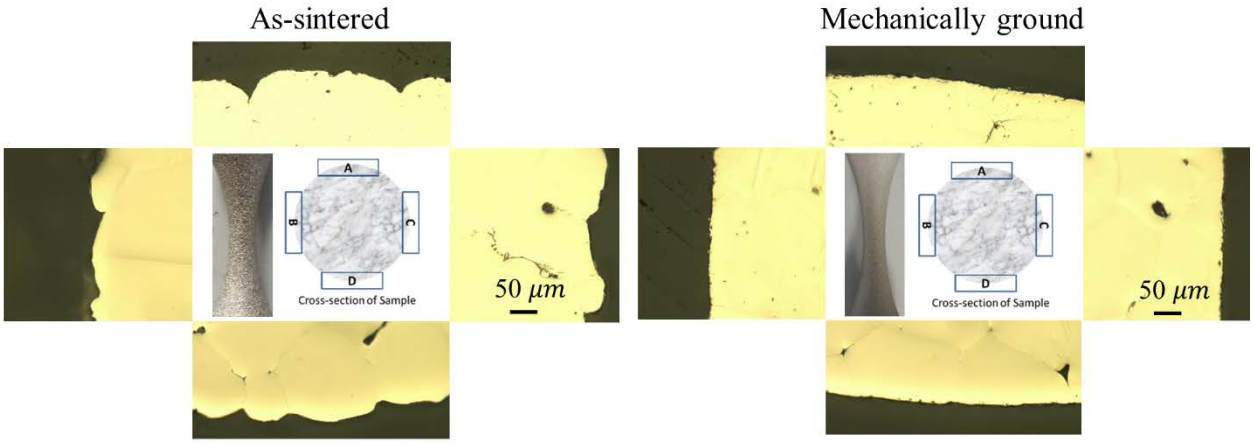

Figure 45. Optical micrographs taken from the cross-section of the central part of the fatigue sample in which failure may happen. Comparison shows that he as-printed sample has a rough surface while the mechanically ground sample shows smooth surface.

The hardness of all samples in the region well below the surface was 225 ± 30 for both samples. The two loads tested, 25 and 50 gf, displayed identical hardness values, therefore the data are averaged together and the typical units ($HV_{0.025}$ and $HV_{0.050}$) are omitted. As expected, the hardness was unaffected by depth for the as-sintered sample. However, the mechanically ground

sample displayed a significant increase in the near-surface hardness after polishing, as shown in Figure 46. Specifically, the hardness at the surface was 415 ± 70, and the increased hardness persisted to approximately 75 μm underneath the surface. This indicates the presence of extensive work hardening in the material from the mechanical grinding step, and likely indicates an increase in surface stress.

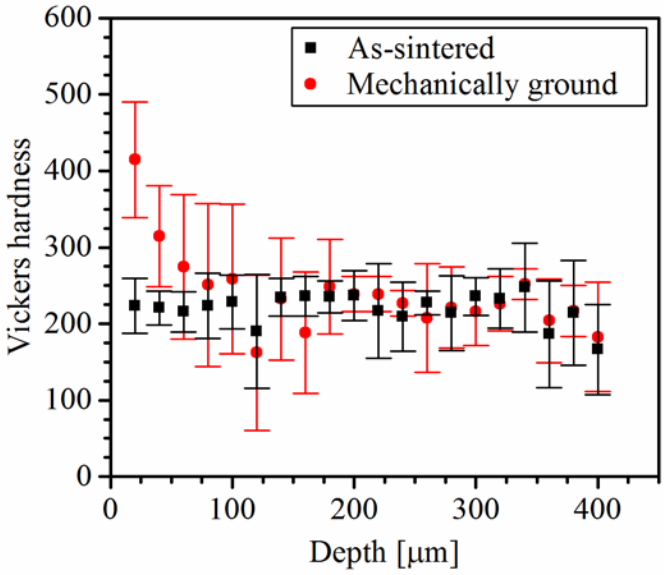

Figure 46. Hardness measurements on the as-sintered and mechanically ground fatigue samples.

To more quantitatively compute the surface stress, XRD of the surface of both as-sintered and mechanically ground samples was performed and results are illustrated in Figure 47. Comparing the XRD pattern of both surface conditions, two main differences from as-printed to ground conditions were observed: (1) all peaks shifts to the lower 2θ values and (2) peaks broadened. Lattice parameters given in Table 2 indicated that peak shift occurred in all peaks and the out-of-plane d-spacing values increased. On the example of the (111) lattice planes, a peak

shift from 43.554° to 43.404° was detected from the as-sintered to the mechanically ground condition, respectively. Using Bragg's law, this resulted in an out-of-plane d-spacing value change from 2.076 to 2.083, indicating elastic expansion out-of-plane and compression in-plane Peak broadening can be inferred as the occurrence of grain refinement and broader micro-strain variations.

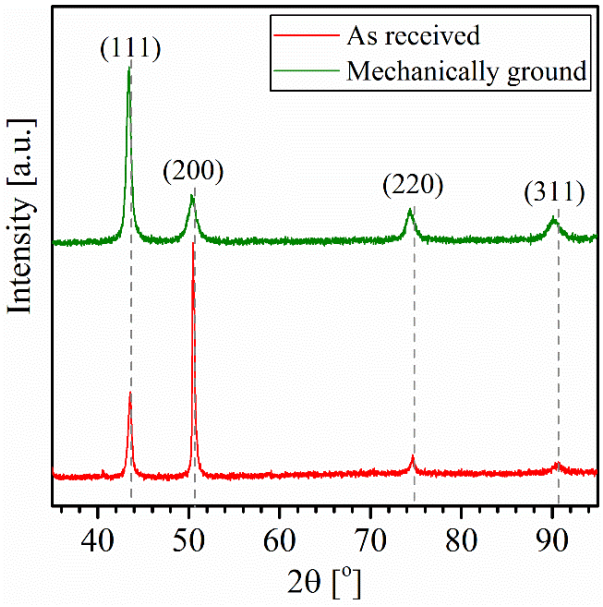

Figure 47. XRD patterns taken from the curved surface of the as-sintered and mechanically ground samples.

Table 6. Crystallographic parameters comparison between as sintered and mechanically ground BJ3DP alloy 625 after sintering process. Units for D-spacing, peak position and FWHM are [Å], [°] and [°], respectively.

Samples	Crystallography parameters											
	111			200			220			311		
	2θ	d-spacing	FWHM	2θ	d-spacing	FWHM	2θ	d-spacing	FWHM	2θ	d-spacing	FWHM
As-sintered	43.560	2.078	0.177	50.438	1.809	0.098	74.669	1.271	0.394	90.520	1.084	0.960
Mechanically ground	43.405	2.085	0.433	50.365	1.812	0.551	74.317	1.276	0.551	90.158	1.088	1.152

The grain size and micro-strain of the as-sintered and mechanically ground samples were calculated from line broadening of Bragg diffraction peaks by using the following equations [170]:

$$D = \frac{K\lambda}{\beta}\cos\theta \quad (6\text{-}4)$$

$$\varepsilon = \frac{\beta}{4}\tan\theta \quad (6\text{-}5)$$

where D is the grain/crystallite size, K is a constant, λ is the X-ray wavelength, β is the full width at half maximum (FWHM) of the peak, θ is the Bragg angle of the [h k l] reflection, and ε is the micro-strain. The calculated grain size and micro-strain was 483 Å and 0.193% for the as-sintered sample while they were 197 Å and 0.475% for the mechanically ground sample. In other words, a reduction in the grain/crystallite size and increase in the micro-strain was seen after mechanical grinding process, leading to the grain refinement, enhancement of the lattice distortion and increasing micro-strain and, therefore, further contributions to the improved fatigue life of the mechanically ground samples, similar to [171,172].

6.2.3 Combining characterization and fatigue results

The fatigue performance of the BJ3DP alloy 625 material is poorer in its as-sintered state as compared to the cast material. It is necessary to point out that a tension-compression condition at R = -1 was used in our study while it was 0.1 as reported in [165]. However, the performance is significantly improved, even beyond the cast material, upon mechanical polishing. Microscopy observations revealed differences in surface roughness between the surface material and bulk material. Hardness measurements showed an enhancement in the surface hardness of the mechanically ground sample. Additionally, XRD revealed crystallite refinement on the surface, in-plane compressive stress and higher micro-strain due to surface treatment in the mechanically

ground sample. These results compare favorably to prior reports on other AM techniques showing effects of surface treatment on fatigue performance in Ti-6Al-4V [173–176] and Ni-based alloys [177,178].

More specifically for surface topography, significant reductions in roughness were reflected in all measured roughness parameters, including larger-scale metrics (h_{rms}), smaller-scale metrics (R_q, R_a), and max-/min-height metrics (R_t, R_v). While it is well-known that surface finish affects fatigue performance [169], it is also known to depend on surface stress. For a given surface stress, some authors [179,180] have proposed phenomenological models linking roughness parameters to notch dimensions, which depend on combinations of metrics such as root-mean-square height, slope, and curvature. However, the values of RMS slope and curvature depend heavily on small-scale measurement [169] and so cannot be reliably obtained from stylus or optical profilometry.

Finally, the combination of improved surface roughness, microstructural refinement and increased, compressive in-plane stress and micro-strain increases caused by the mechanical surface treatment contributed to the fatigue life enhancement of the BJ3DP alloy 625 samples. Mechanical grinding would therefore be an appropriate tool for all binder jet printed samples to improve fatigue performance. Further investigation is required to distinguish among these various factors, but the most probable explanation for the significant increase in fatigue performance can be the creation of near-surface mechanical damage and the elimination of deep valleys which serve as stress concentrations.

6.2.4 Summary

The major aim of the present section was to evaluate binder jet 3D printing as a technique for creating parts using nickel-based superalloy 625, which maintain high fatigue resistance. Fatigue testing demonstrated poor performance of initially created parts after printing and sintering as compared to prior investigations on the cast material. However, with mechanical ground of the surface, the fatigue performance improved significantly, surpassing that of the cast alloy. Fracture surface investigation showed evidence of transgranular crack initiation, followed by intergranular crack growth. μCT and microstructural observations showed that the BJ3DP parts had a relative density of 98.9 ± 0.3 %, with equiaxed grains. The near-surface layer of the as-sintered parts was shown to have unmelted particles, and a layer of increased densification, these surface layers were removed with mechanical grinding process. Using optical and stylus profilometry, the as-sintered BJ3DP parts were shown to have large roughness, which was significantly reduced upon grinding. The stylus profilometry showed an RMS roughness of R_q = 1.39 ± 0.20 μm, which was reduced upon grinding to R_q = 0.47 ± 0.02 μm. The optical profilometry showed an RMS roughness of R_q = 12.01 ± 2.52 μm, which was reduced to R_q = 2.78 ± 1.10 μm. The differences in these values were attributed to differences in techniques and to measurement artifacts, but both show a significant reduction. The improvement in fatigue behavior likely arose from removing the rough surface, micro-strain enhancement, formation of a fine grain structured layer of 75 μm and/or in-plane compressive stress on the surface of the mechanically ground sample. Further work is on-going to distinguish which factor had the most significant effect on fatigue performance. Overall, the present results show that binder jetting, followed by proper sintering and surface treatment, is shown to be a promising alternative to the conventional manufacturing processes for alloy 625.

6.3 DENSIFICATION KINETICS OF BJ3DP ALLOY 625

The powder size distributions are presented in Figure 48. Based on the illustrated results in Figure 48a-c, the D_{50} values of the powders are 30.7 µm, 22.3 µm and 51.4 µm, respectively.

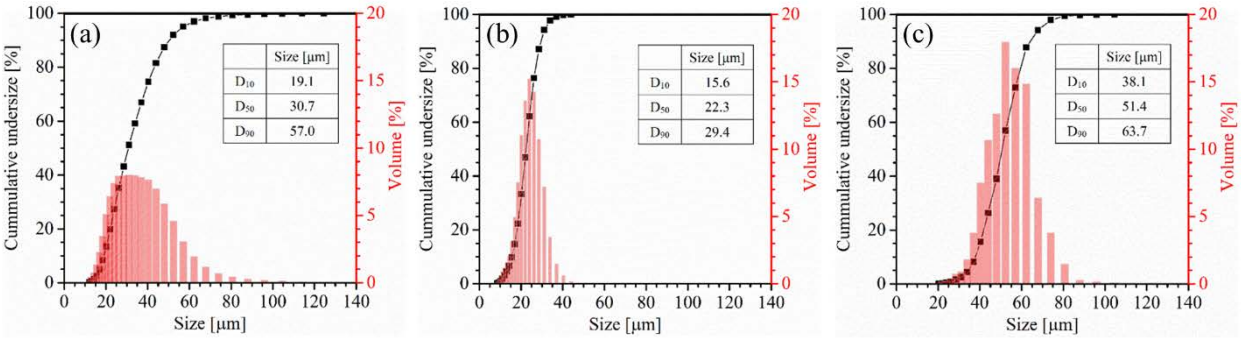

Figure 48. Cumulative and volume percentile results indicating powder size distribution for (a) original powder defined as 16-63 µm, (b) sieved powder with particle size below 25 µm, defined as 16-25 µm, and (c) sieved powder with particle size between 53 and 63µm, defined as 53-63 µm.

The cross-sectional optical micrographs in Figure 49 displays shape, size, and distribution of porosity as well as the microstructure of the BJ3DP samples from three different powder mean sizes sintered ranging from 1225 °C to 1300 °C for 4 h. Generally, a progression with increasing sintering temperature from irregular, interconnected pores to spherical pores within the grains or located at the grain boundaries was observed. Micrographs of all three powder types indicated that sintering between 1225 °C and 1255 °C resulted in highly porous samples with interconnected pores. An obvious evolution in microstructure was seen when the sintering temperature increased from 1255 °C to 1270 °C in which pore evolution in the microstructure was visible. As the sintering temperature increased to 1285 °C and 1300 °C, it was seen that the binder jetted parts from 16-63

μm powder resulted in the near-full density of 99.9% while parts printed from 16-25 μm and 53-63 μm powders showed density of 98.2% and 97.5%.

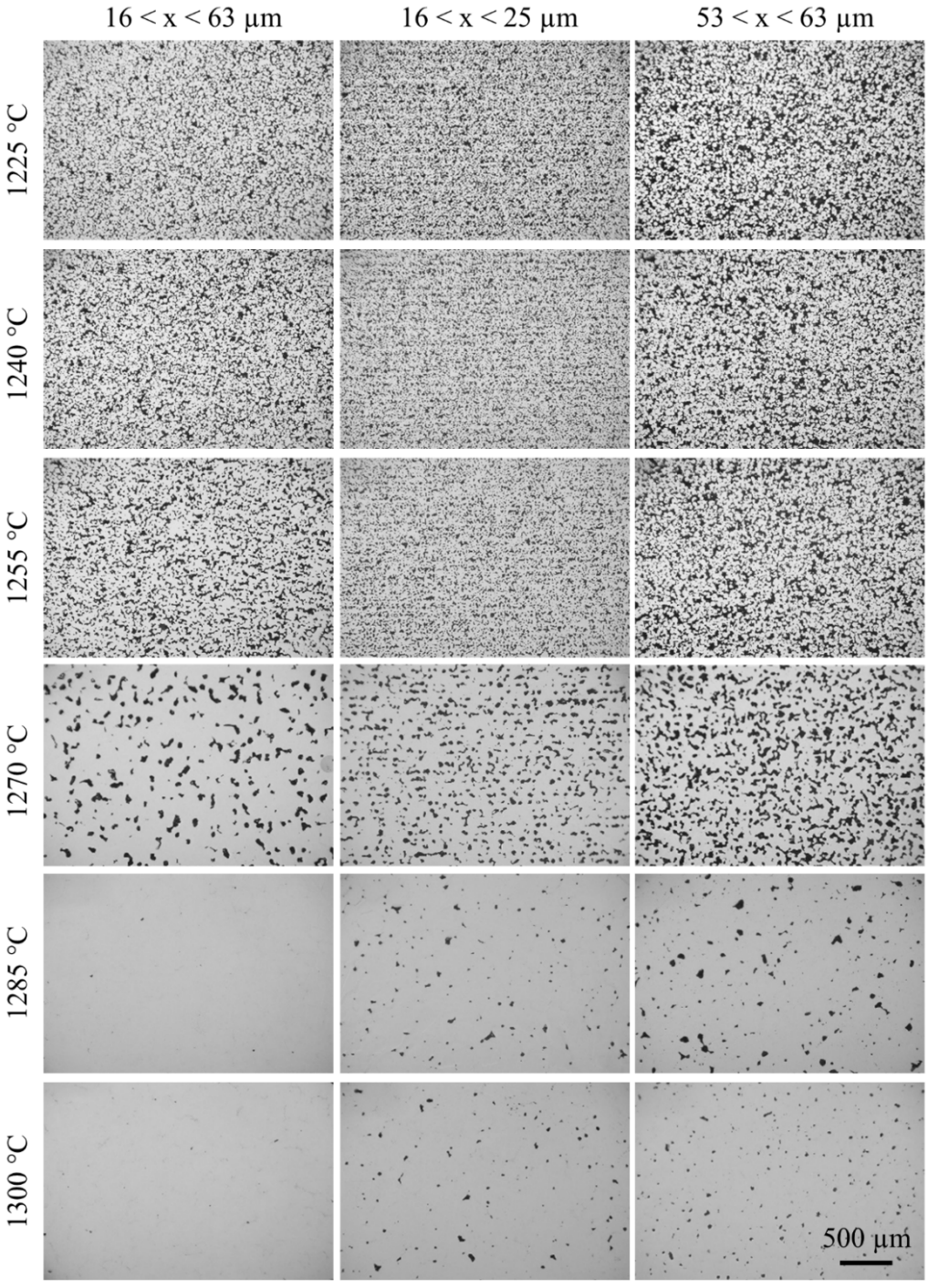

Figure 49. Optical micrographs of BJ3DP alloy 625 samples sintered at different temperatures for 4 h.

Figure 50a shows the variation of solid volume fraction (obtained from image analysis of the presented results in Figure 49) for different particle sizes as a function of temperature. It is seen that the solid volume fraction increased with increasing sintering temperature from 1225 °C to 1300 °C. At the sintering temperature of 1225 °C, it was observed that the powder particles with size range of 53-63 μm had lower density compared to the two other size distribution while the distribution of small powder particles showed higher density. As the sintering temperature increased above 1270 °C, powder particles with size range of 16-63 μm showed higher density compared to the 16-25 μm, with a maximum density of 99.9% achieved at sintering temperature above 1285 °C.

Figure 50b illustrates the variation of bulk density (obtained from Archimedes method) for different particle sizes as a function of temperature. In general, it is seen that the bulk density increased with increasing sintering temperature from 1225 °C to 1285 °C. It was also observed that the powder particles with size range of 53-63 μm had lower density compared to the two other size distribution while the distribution of small powder particles showed the highest density up to 1270 °C. Above 1270 °C, powder particles with size range of 16-63 μm showed higher density, with a maximum density of 99.2 ± 0.2% (based on the Archimedes method). At the maximum sintering temperature of 1285 °C, pore coarsening was observed in some samples. Pore coarsening and its effect on densification during final stage sintering is a well-established phenomenon. In fact, pore size differences and curvature led to the growth of large pores at the expense of the smaller, stable pores [33,129,181]. Typically, powders with smaller particle size (in this study, 16-25 μm) have higher surface energy per unit weight compared to larger powder particles (in this study, 53-63 μm). Therefore, higher density is expected for 16-25 μm at any particular sintering temperature. The wide particle size distribution (16-63 μm) gave lower bulk density than the 16-

25 μm powder for sintering temperatures less than 1270 °C, consistent with the presence of larger particles and lower surface area. Interestingly above 1270 °C the wider particle size distribution gave slightly higher density.

Figure 50c shows the linear shrinkage $\left(\frac{\delta L}{L}\right)$ for different particle sizes as a function of temperature with L being the length of the as-printed part. Here, dimensional variations are considered for x, y and z. It is found that the linear shrinkage of the small powder particles in all three dimensions is higher than the two other powder size distributions at all temperatures, consistent with the lower green density. There is a cross-over point in the shrinkage plot of 16-63 μm and 53-63 μm powders at 1270 °C. Sintering at a maximum temperature of 1300 °C for 4 h led to the surface melting in samples and it was not practical to measure the linear shrinkage. P. Nandwana et al. reported the effect of powder particle size effect on the sintering of BJ3DP alloy 718 [26]. It was shown that the 21 μm feedstock had a solidus temperature that was ~30 °C and 40 °C higher than the 7 μm and 70 μm feedstock, respectively. Additionally, an increase of 50 °C above the liquidus temperature increased the liquid volume fraction to about 55% leading to the shape loss. Such a variation might be indicative of a change in the sintering mechanism, possibly from solid-state sintering to supersolidus liquid phase sintering (SLPS) [156]. It is seen that the linear shrinkage was higher in z direction which can be affected by gravity and rigidity of the solid structure during SLPS.

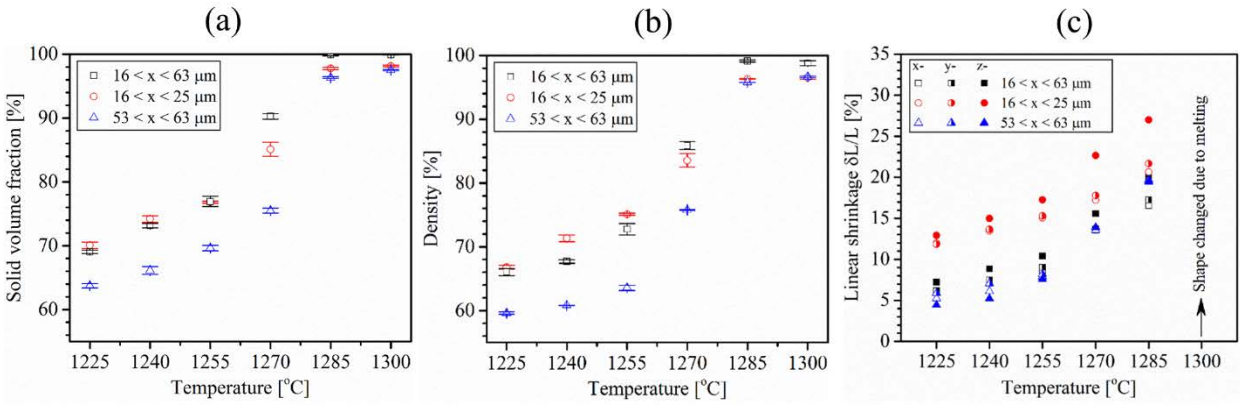

Figure 50. (a) Solid volume fraction obtained from image analysis shown in Figure 49, (b) relative density for different particle sizes as a function of temperature and (c) linear shrinkage in x, y and z directions for the three different powder particle sizes as a function of temperature.

To study the densification kinetics during solid-state sintering, three temperatures (1240 °C, 1270 °C and 1280 °C) were selected for isothermal sintering studies for the BJ3DP alloy 625 powder. Optical micrographs of the different sintered samples at 1240 °C (Figure 51), 1270 °C (Figure 52) and 1280 °C (Figure 53) for holding times between 0 and 12 h were studied. In the distribution of small powder particles sintered at 1240 °C (Figure 51) and 1270 °C (Figure 52), the printing lines were obvious in the printed parts while they were not seen in samples printed with the large powder particles(53-63 µm) and full range size distribution (16-63 µm) powder particle size distribution. Since 1240 °C is well below the solidus temperature for the alloy 625 powder, solid-state sintering is the dominant and microstructural evolution due to densification is within intermediate sintering but relatively limited. Therefore, the optical micrographs of sintered samples (as shown in Figure 51) did not show dramatic microstructural evolution as holding time increased from 0 h to 12 h. As the sintering temperature increases to 1270 °C (Figure 52), more extensive microstructural evolution can be seen for unetched samples depending on the holding time. It was found that there was a pronounced evolution in pore size and reduction in the number

of pore sections in the image. Basically, grain growth, an increase in the pore intercept and a decrease in the number of pore sections per unit area occurred in all three sets of samples at this temperature. This was particularly noticeable after sintering for 2h for the 16-63 μm powder, after 2 h for the 16-25 μm powder and after 8 h for the 53-63 μm powder. Based on our earlier study on the solidus temperature of gas atomized alloy 625 [33,54], the solidus temperature is ~1283 °C for the 16-63 μm powder. As the powder particle size decreases, the effective surface area increases, thus there is a higher driving force for densification. In other words, for the large powder particle of 53-63 μm, lower relative density was seen for the sintering temperature below 1270 °C compared to the small and full range powder particles sintered at the same temperature and holding time. Finally, at 1280 °C which is below of the reported solidus temperature for our metal powder [33], microstructure evolution and densification was relatively rapid. For the 16-63 μm powder, prolonging the holding time led to the pore shrinkage and removal during final stage densification. Although the sintered density was increased for the sintered parts made from 16-25 μm and 53-63 μm powders, density was lower compared to that of the 16-63 μm powder at the same sintering conditions. In addition, there was less pore elimination at the longer hold times, even for the finer powder. This may be associated with the lower green part density of the BJP part prepared from the narrower size distributions with small and large powder particles. Even though printing parameters (e.g. binder saturation), were similar for all powder types, the BJ3DP powder with wide size distribution (e.g. 16-63 μm) resulted in higher green part density compared to small and large powder particles. Regarding the 16-63 μm powder, the maximum sintered density of 99.7% (optical image analysis result) was achieved for samples sintered for 4 h or longer. Finally sintering at 1280 °C caused a readily observable change from irregular, elongated pore shapes to more rounded pore shapes (see Figure 53).

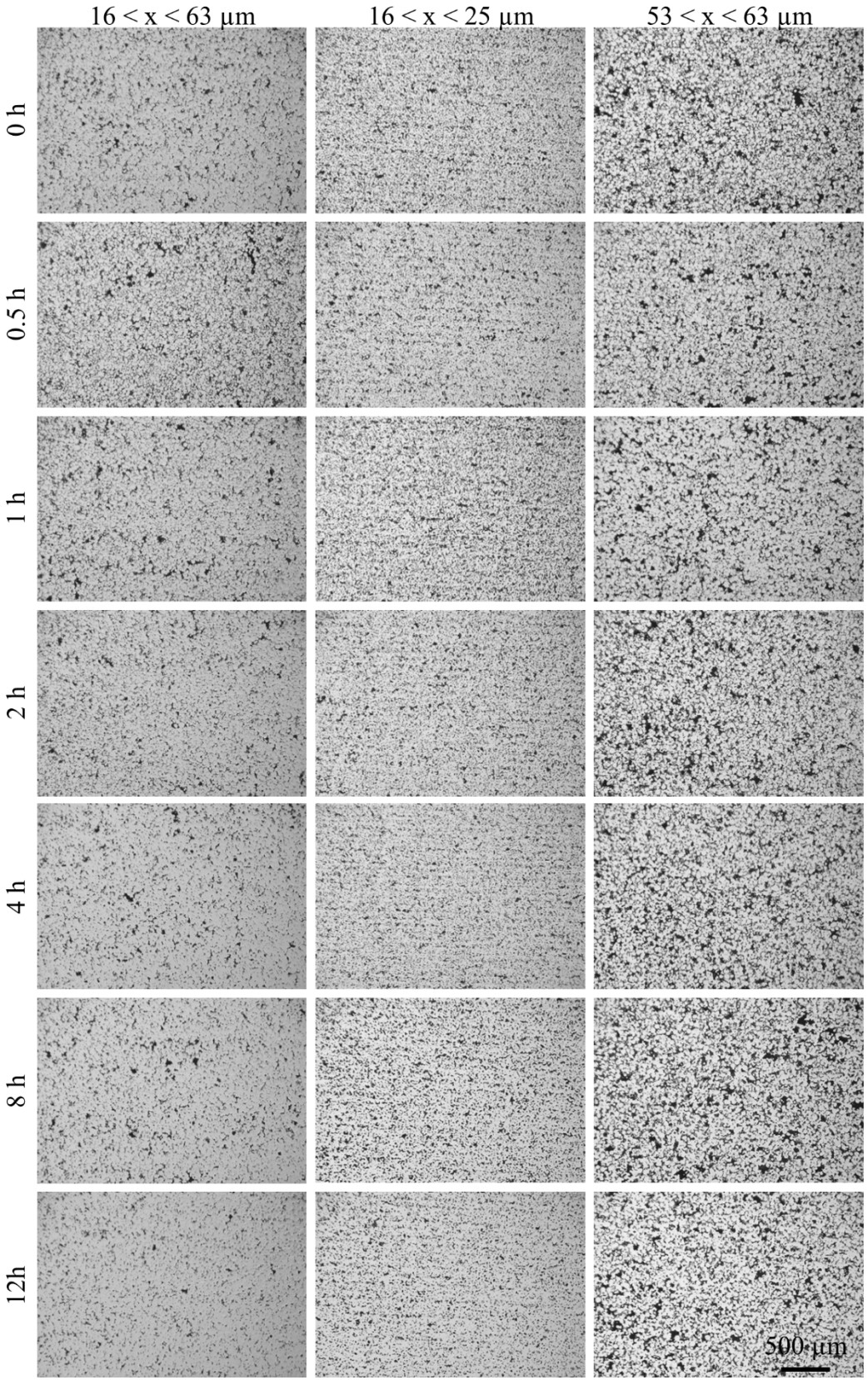

Figure 51. Optical micrographs of the BJ3DP alloy 625 samples sintered at 1240 °C.

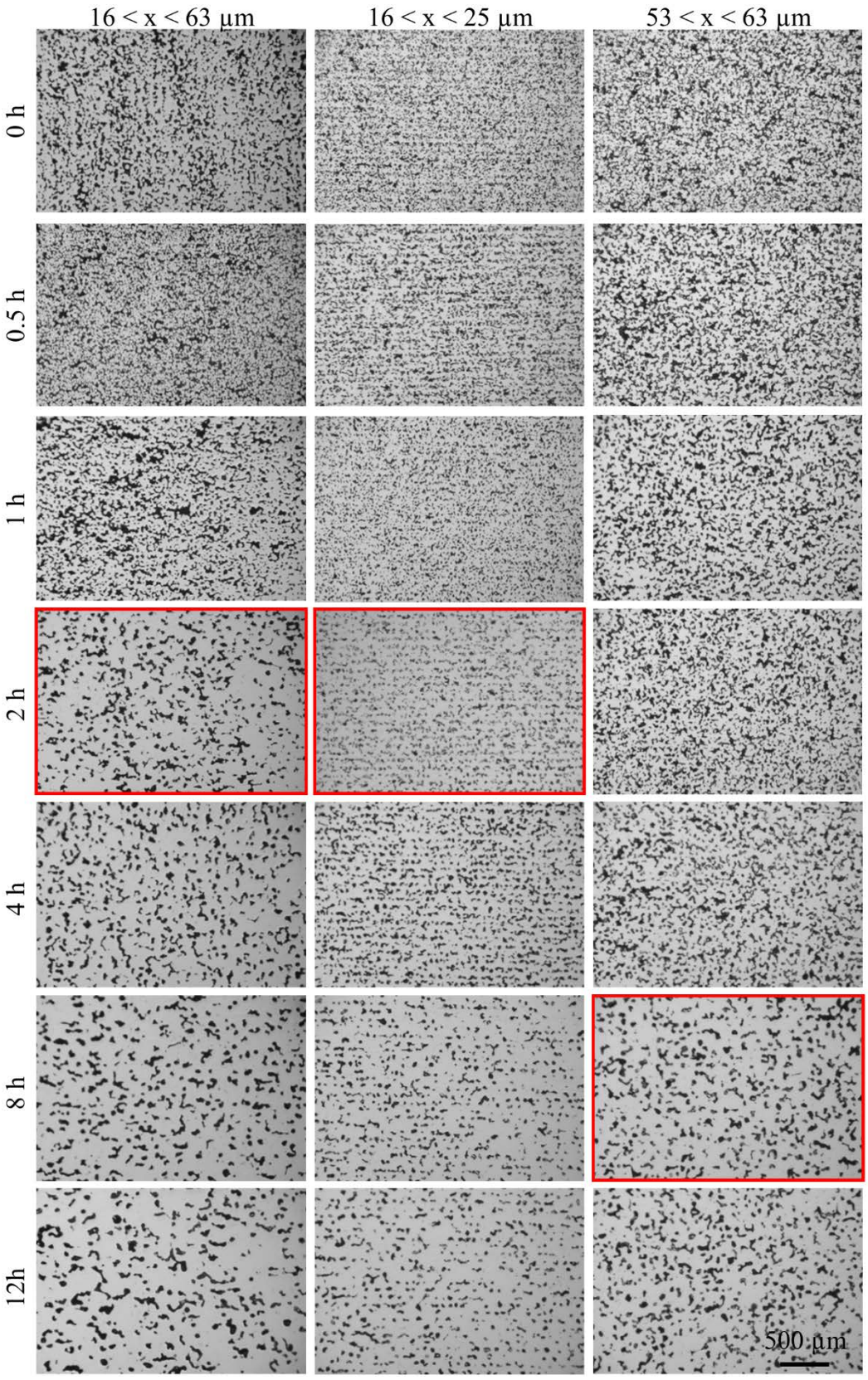

Figure 52. Optical micrographs of the BJ3DP alloy 625 samples sintered at 1270 °C.

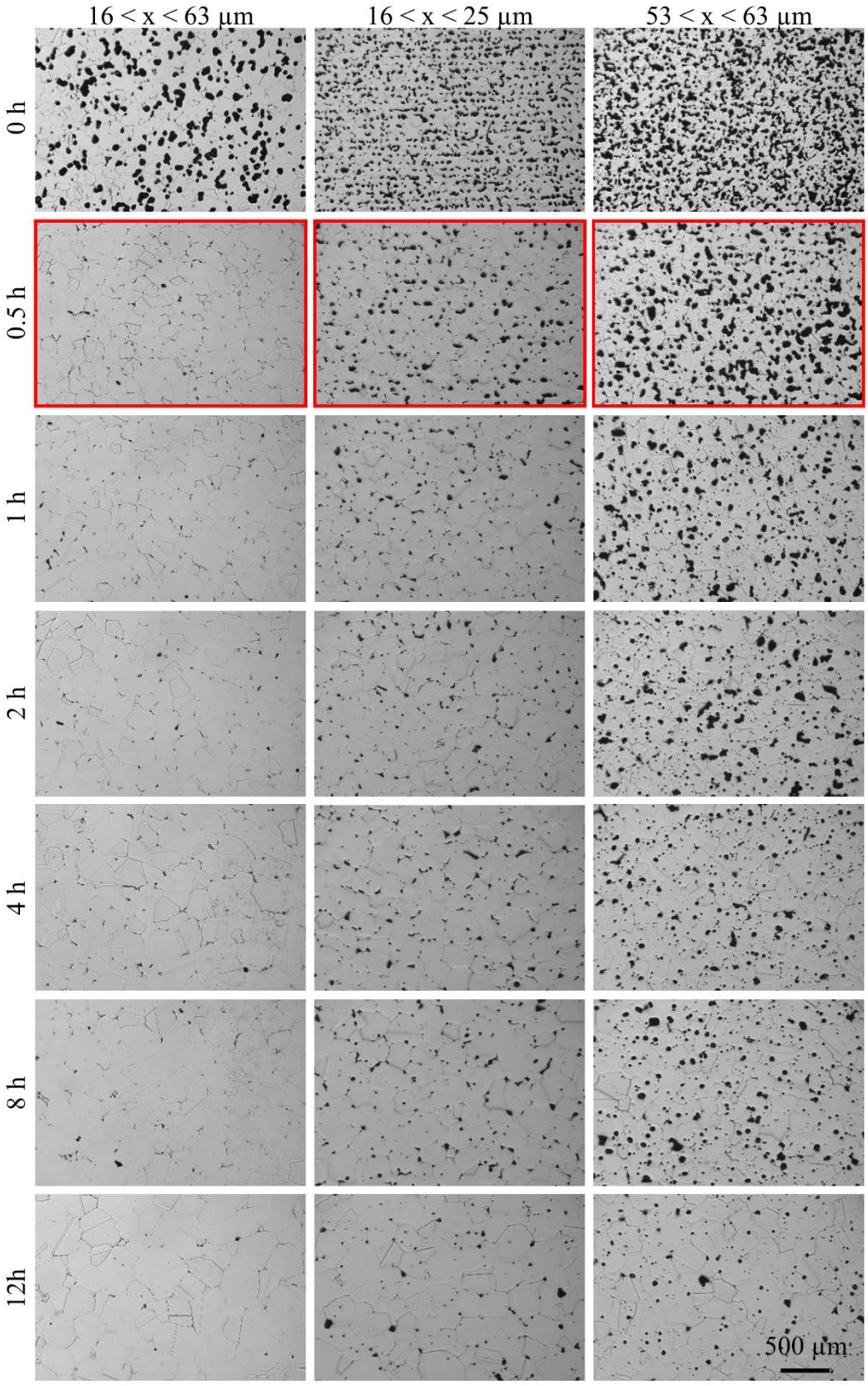

Figure 53. Optical micrographs of the BJ3DP alloy 625 samples sintered at 1280 °C.

Several microstructural parameters were examined to characterize the evolution of the microstructure during densification at the different temperatures. The terms low, intermediate and high solid volume fraction refer to 0.82, 0.90 and 0.96 solid volume fractions, respectively. The time evolution of the solid volume fraction obtained from the BJ3DP parts with the three powder size distributions sintered at 1240 ºC, 1270 ºC and 1280 ºC is shown in Figure 54a-c. Typically, it was seen that for the same sintering time, a powder with smaller particle size had higher solid volume fraction. It was observed that at the lowest sintering temperature (1240 ºC), a low solid volume fraction was achieved for all samples after 12 h sintering, the maximum solid volume fraction being 78% for the 16-25 μm powder. There is a significant difference between the range of solid volume fraction for 53-63 μm, which only achieved 70% compared to the two others which reached significantly higher values. With increasing sintering temperature to 1270 ºC, the solid volume fraction for 53μm-63μm was well below the solid volume fraction for the other two distributions sintered at the same sintering time. At the longest time, 53μm-63μm achieved 80% but the other two powders gave significantly higher solid volume fraction. At both sintering temperatures, the presence of the fine powder particles in the distribution enhanced the densification kinetics. Finally, sintering at 1280 ºC the densification kinetics were significantly improved. As at the lower temperatures, the coarse powder gave lower solid volume fraction at times less than 2 h. However, all the powders quickly attained solid volume fractions associated with final sintering stage (with density above 96%). It is known that the driving force for sintering is the reduction of free energy by reduction in the amount of surface area. The surface area per unit volume of a particle is inversely proportional to its size (powder particle's diameter), smaller particles have larger amounts of surface area per unit solid volume and a greater potential for sintering. Hence, the small powder particles showed higher densification for solid state sintering

at 1240 ºC and 1270 ºC. Apparent density values for the samples sintered at 1280 ºC is also shown in Figure 54a-c (blue solid data points). The difference between apparent and bulk density indicates the proportion of the pores that are open and connected to the surface. It was seen for the 16-25 μm and 16-63 μm powders sintered at 1280 ºC that the relative and apparent densities were almost the same for any holding time longer than 1 h. This suggests all the pores are closed as required by final stage sintering. This did not occur for the 53-63 μm powder until 8 h. The fitted lines on Figure 54a-c are the common relationship fitted to intermediate and final stage densification. In other words, the sintering kinetics follows the equation shown below:

$$\rho = \rho_0 + k \ln(t) \qquad (6\text{–}6)$$

where ρ is the bulk density after isothermal sintering for a period of t, ρ_0 is the bulk density after isothermal sintering for 1 h, k is a constant which could be viewed as the isothermal rate constants. These calculations are necessary to determine volume strain rate using the experimental results using the first derivative of equation 13.

A comparison between the bulk density values obtained from the Archimedes method and the solid volume fraction from the image analysis results is displayed in Figure 54d-f. It was seen at sintering temperature of 1240 ºC, there was a significant, but relatively small difference between these measurements for some samples. This could be related to the inability to detect and measure the smallest pores during image analysis. As the sintering temperature increased to 1270 ºC, the differences in the measured bulk density and solid volume fraction values were usually within the error of the measurements indicating the images are collectively representative. Finally, both the bulk density and the solid volume fraction from the image analysis matched (specifically for the 16-25 μm and 16-63 μm powders) for the sintering times at 1280 ºC. Therefore these images were also considered representative

Figure 54g-i illustrates the linear shrinkage $\left(\frac{\delta L}{L}\right)$ for different powder particle size sintered at the selected temperatures as a function of time with L being the length of the as-printed part. Similar to our earlier measurements, dimensional variations are considered for x, y and z directions. It is found that the linear shrinkage for the powder made from small powder particles at any temperature and/or holding time is higher than for the two other powders. Additionally, a larger linear shrinkage occurred in the z direction for the small powder particles while for the two other powders, linear shrinkage were similar in x, y and z directions. The maximum linear shrinkages of 18% (x and y directions) and 20% (z direction) were attained for the 16-63 μm and 53-63 μm powders while linear shrinkages of 21%, 25% and 29% in x, y and z direction was seen for the 16-25 μm powder.

The stereological measurements of the solid-solid (S_V^{SS}, grain to grain or particle to particle interfaces) surface area to volume ratio and solid-vapor (S_V^{SV}, grain to pore or particle to pore interfaces) surface area to volume ratio were made using standard methods of point counting. The evolution of the surface area per unit volume is shown in Figure 54j-l. At the sintering temperature of 1240 ºC and 1270 ºC, S_V^{SV} values were higher than S_V^{SS} values at any holding time. As the sintering temperature increased to 1280 ºC, it was seen that S_V^{SS} was higher than S_V^{SV} indicating an evolution in microstructure into final stage sintering. Results of the 1280 ºC showed a steady decrease in solid/solid surface areas (S_v), which implied that grain growth is occurring over the entire density range covered.

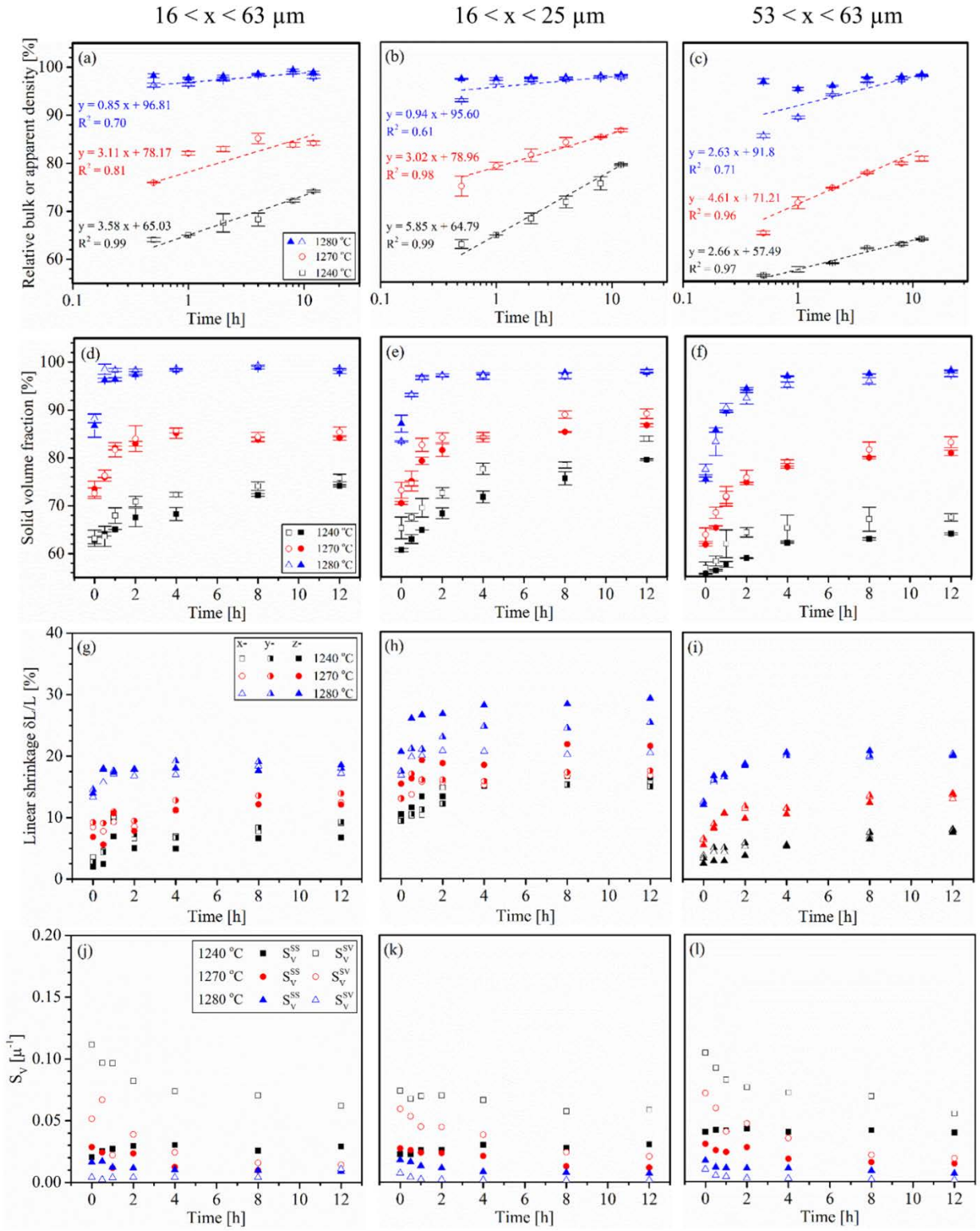

Figure 54. (a-c) Relative or apparent density, (d-f) comparison between density obtained from Archimedes method (solid points) and image analysis results (emply points), (g-i) linear shrinkage as a function of temperature, and (j-l) surface area per unit volume results.

The volume strain rate is defined as the ratio of the slope of the graph of density vs. sintering time (see Figure 54a-c) and obtained results are shown in Figure 55. As expected the densification rate tends to decrease with increased sintering time and with increasing solid volume fraction. At 1280 ºC the densification rate is uniformly low because the materials are in final stage sintering and the associated diffusion distance is increasing quickly. Interestingly, the coarser powder gives higher densification rates at this temperature probably because this is associated with lower solid fractions for all but the longest times. The particle size distributions have a more significant effect at the lowest temperature, 1240 ºC where the materials made from the fine particles have a much higher densification rate than for the other size distributions that contain coarse particles. Indeed some of the highest densification rates were measured for the fine particle size distribution at 1240 ºC. This is entirely consistent with the effect of small particles on surface area per unit volume and sinterability [121]. At 1270 ºC the distributions containing fine particles showed much the same variation in densification rate with sintering time. Interestingly, the distribution made of coarser particles showed significantly higher densification rate as a function of time but the earlier sintering times corresponded to lower solid volume fraction when the densification rates are expected to be higher during isothermal sintering. Therefore, the densification rate results show an interdependence on temperature, solid volume fraction and particle size that is consistent with the expected effect of these variables on densification kinetics.

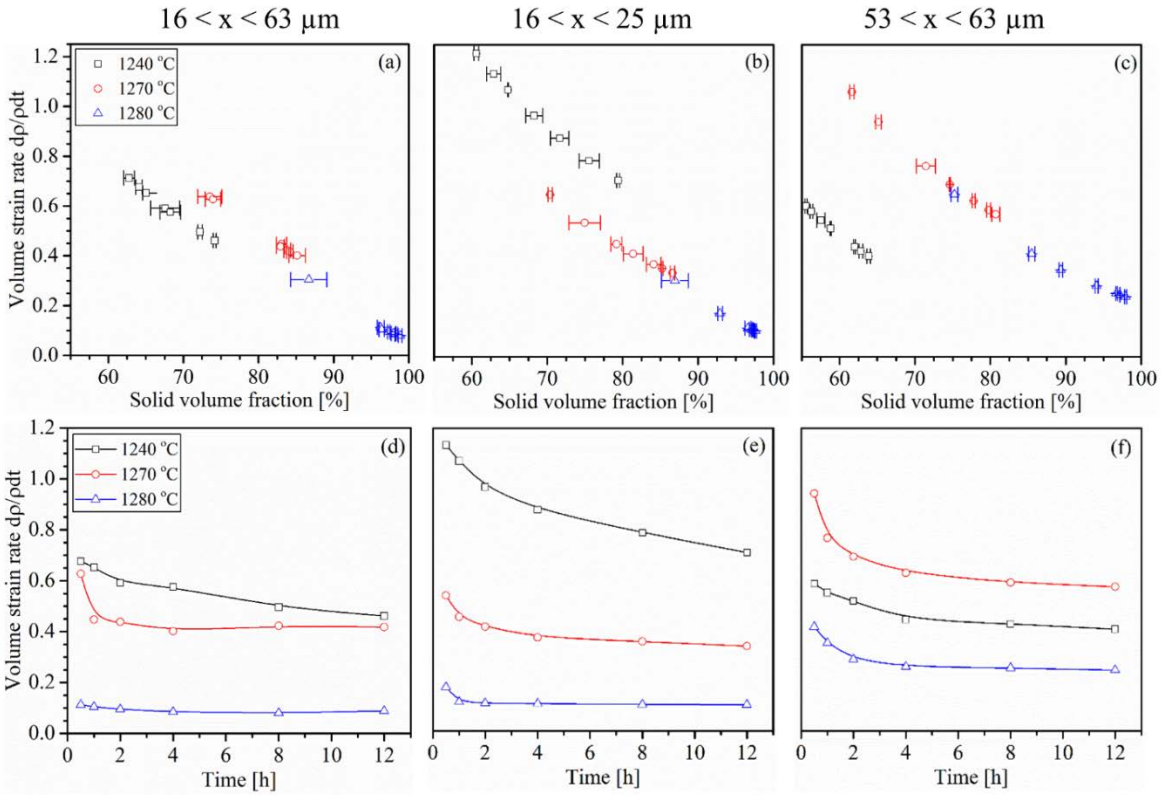

Figure 55. Volume strain rate (densification rate) vs (a-c) density or (d-f) holding time indicating the relationship for isotermal sintering of different powder particle sizes.

In general, it is thought that the wide pore size distribution and low green density associated packing defects affect microstructural evolution and in particular the grain size and diffusion distances in final stage sintering. Thus, it was essential to examine as the effect on the average microstructural descriptors associated with the densification process. These include the average grain size, pore size and pore separation to determine if the observed effects of processing variables on density and densification rate are associated with an increase in the size of the pores and grains. The evolution of microstructural features such as the grain intercept (λ_G), pore intercept (λ_P) and pore separation or spacing (λ_{PS}) are summarized as a function of relative density and sintering time in Figure 56 and Figure 57.

The mean grain intercept length results (Figure 56a-c) illustrated that in general, the grain intercept evolves along one microstructural pathway for all of the particle size distributions, the largest grain intercepts were observed for the wide size distribution at the longest times at the highest sintering temperatures. Figure 57 illustrates more clearly the pronounced grain growth at 1280 ºC and the significant effect of temperature and solid volume fraction on the grain intercept evolution of BJ3DP alloy 625.

The evolution of the mean pore intercept length is illustrated in Figure 56d-f. The analytical models of sintering suggest that the pore intercept length should decrease throughout sintering. The results of this study show this is not the case. The microstructural pathways show broadly similar trends for the three particle size distributions. It is noticeable that the pore intercept increases significantly with very little increase in solid volume fraction at 1270 ºC for all three particle size distribution. In all cases, the "coarsening" of the microstructure occurred over the solid volume fraction range 0.8 to 0.85. This is consistent with the qualitative observations in Figure 51 and Figure 52 which suggest fine pore sections are being preferentially removed leading to an increase in pore intercept. When the sintering temperature was increased to 1280 ºC, the pore intercept dramatically decreased with prolonging holding time for 16-63 μm powder while it remained relatively constant (or decreased slowly) in the 16-25 μm and 53-63 μm powders. This was associated with higher sintered density for the 16-53 μm samples. The average pore separation values are shown in Figure 56g-i. It was seen that the microstructure pathway for pore spacing was very similar for all three powder types sintered at 1240 ºC and 1270 ºC. However, the pore spacing is dramatically increased for the 16-63 μm powder at 1280 ºC in which the maximum pore spacing of ~3000 μm was obtained. In other words, the pore spacing increased with increasing solid volume fraction due to pore shrinkage and/or the elimination of pores. The examination of these

microstructural pathways for grains, pores and pore separation show the differences in microstructure evolution that result in strikingly different final microstructures for 16-63 µm at 1280 ºC in final stage sintering.

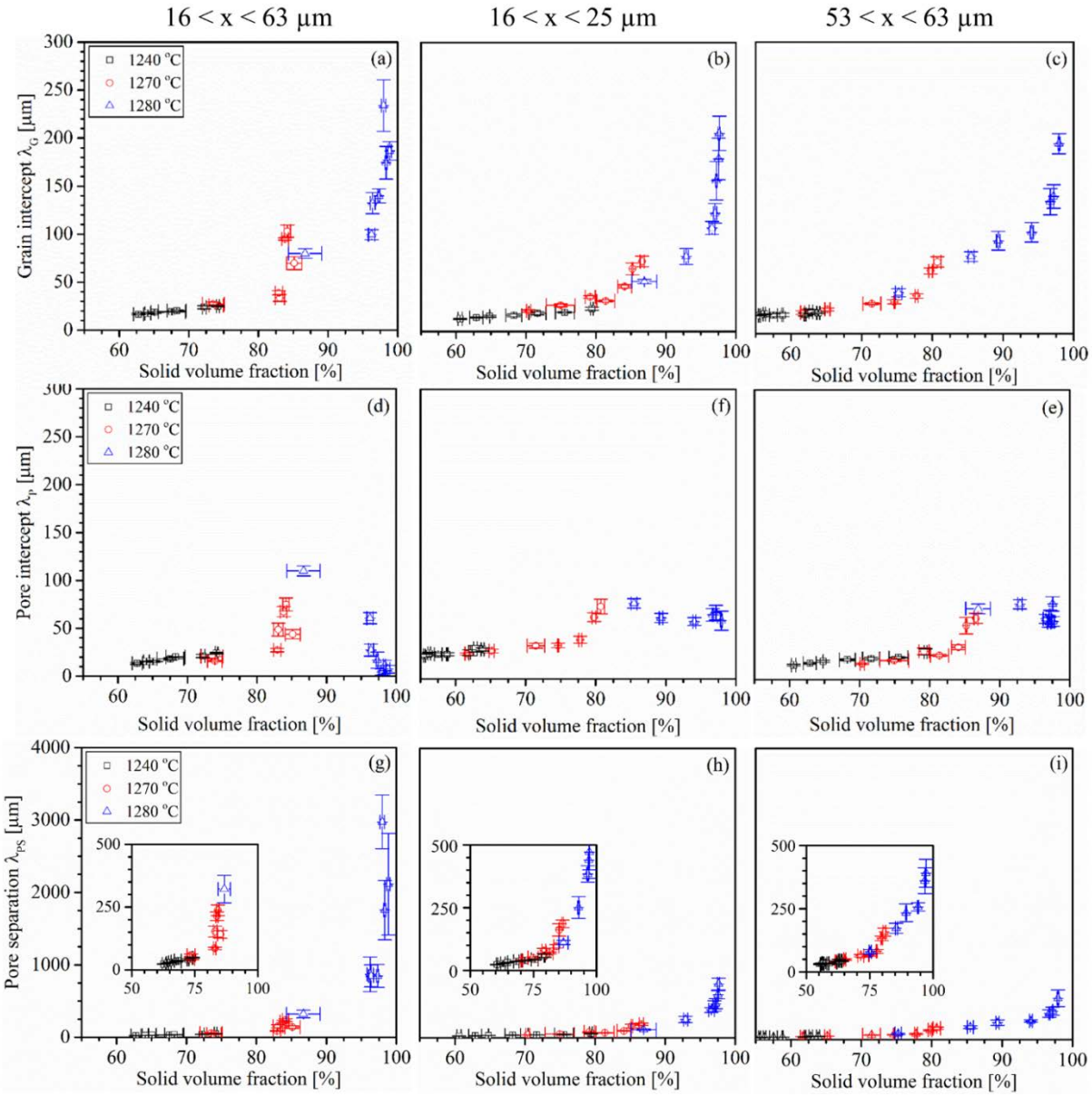

Figure 56. The average grain, pore and pore separation intercept length plotted against density. Samples were BJ3DP from three different powder sizes and distibutions of alloy 625.

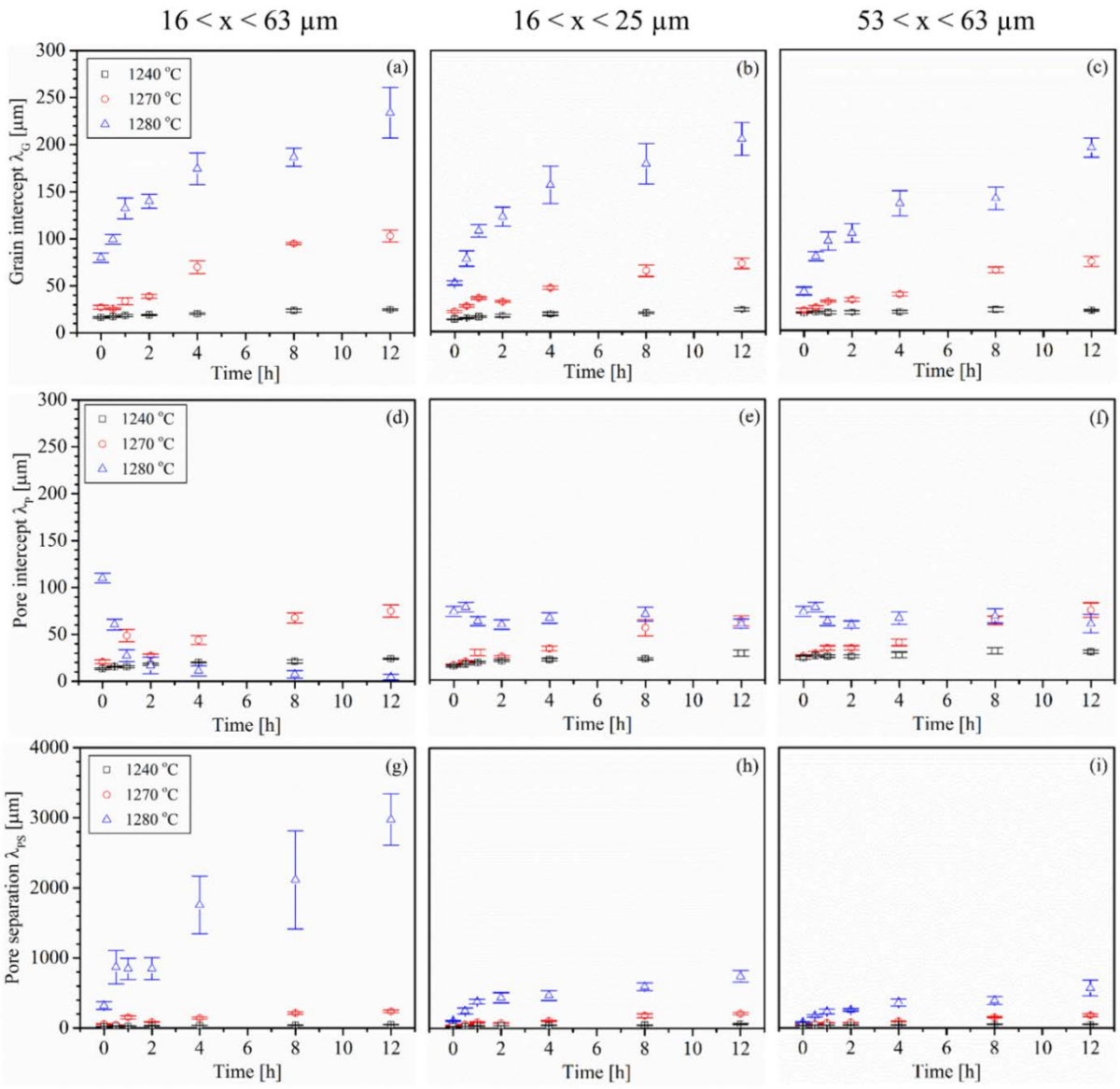

Figure 57. The average grain, pore and pore separation intercept length plotted against sintering time. Samples were BJ3DP from three different powder sizes and distributions of alloy 625.

Three dimensionless microstructural parameters including Λ, ψ and Σ are plotted against relative density in Figure 58. These parameters can be used to determine if the evolution of the grain size and pore size and pore intercept evolve in a similar ways (self-similar microstructural evolution), during sintering. The mean pore spacing to mean grain intercept length ratio (Σ) of the

differently sintered parts made from three types of alloy 625 powder is shown in Figure 58a-c. Trends in this microstructural pathway may indicate the degree to which pore spacing is correlated with grain growth or alternatively the degree to which grain growth is controlled by pore spacing. It can be seen that all three powder particles showed the same ratio of Σ for the sintering temperatures of 1240 ºC and 1270 ºC as the solid volume fraction increases indicating the evolution of pore spacing and grain growth happened such that the ratio was ~2. The Σ value increased to ~3 for the 16-25 μm and 53-63 μm powders as the sintering temperature increased to 1280 ºC during final stage sintering. However, the Σ values significantly increased during final stage sintering for 16-63 μm powder sintered at 1280 ºC, suggesting that the pore separation was increasing much faster than the grains. Hence, grain coarsening alone could not be responsible for the increase in pore separation. In fact, the mean pore spacing is not controlled by grain growth alone but by pore shrinkage and especially pore section removal. Clearly, this is dependent on the original particle size distribution and its effect on particle packing in printing.

Another dimensionless parameter examined is the mean grain to mean pore intercept ratio (Λ). The results shown in Figure 58d-f suggested that the evolution in the size of grains and pores of all three powder particles types happened such that the ratio remained constant for any holding time at the sintering temperatures of 1240 ºC and/or 1270 ºC during intermediate stage sintering. In addition, similar trends were observed for the 16-25 μm and 53-63 μm powders in final stage sintering at 1280 ºC. However, the ratio of grain to pore intercept length was more than 30 for the 16-63 μm powder sintered at 1280 ºC for 12 h, suggesting that grain growth rate was faster than pore coarsening or pore removal may also be happening. Optical microscopy observation as well as pore intercept measurements for the 16-63 μm powder sintered at 1280 ºC showed that pore elimination and pore shrinkage occurred as the holding time increased from 0 h to 12 h.

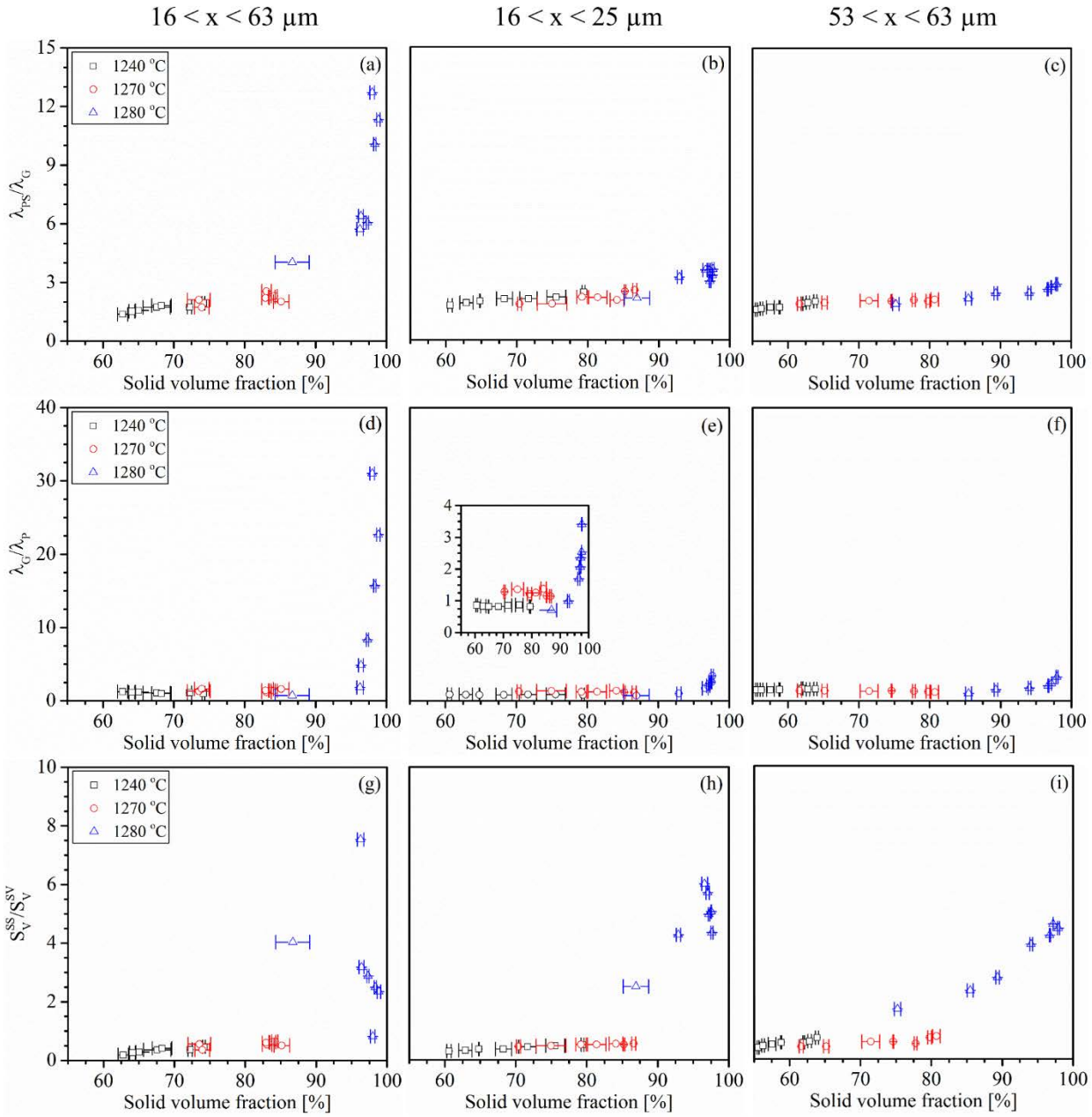

Figure 58. Dimenssionless results vs. relative density for (a-c) the pore separation to grain intercept ratio, (d-f) the grain to pore intercept ratio, and (g-i) The solid-solid surface area to solid-vapor surface area ratio. Samples were BJ3DP from three different powder sizes and distibutions of alloy 625.

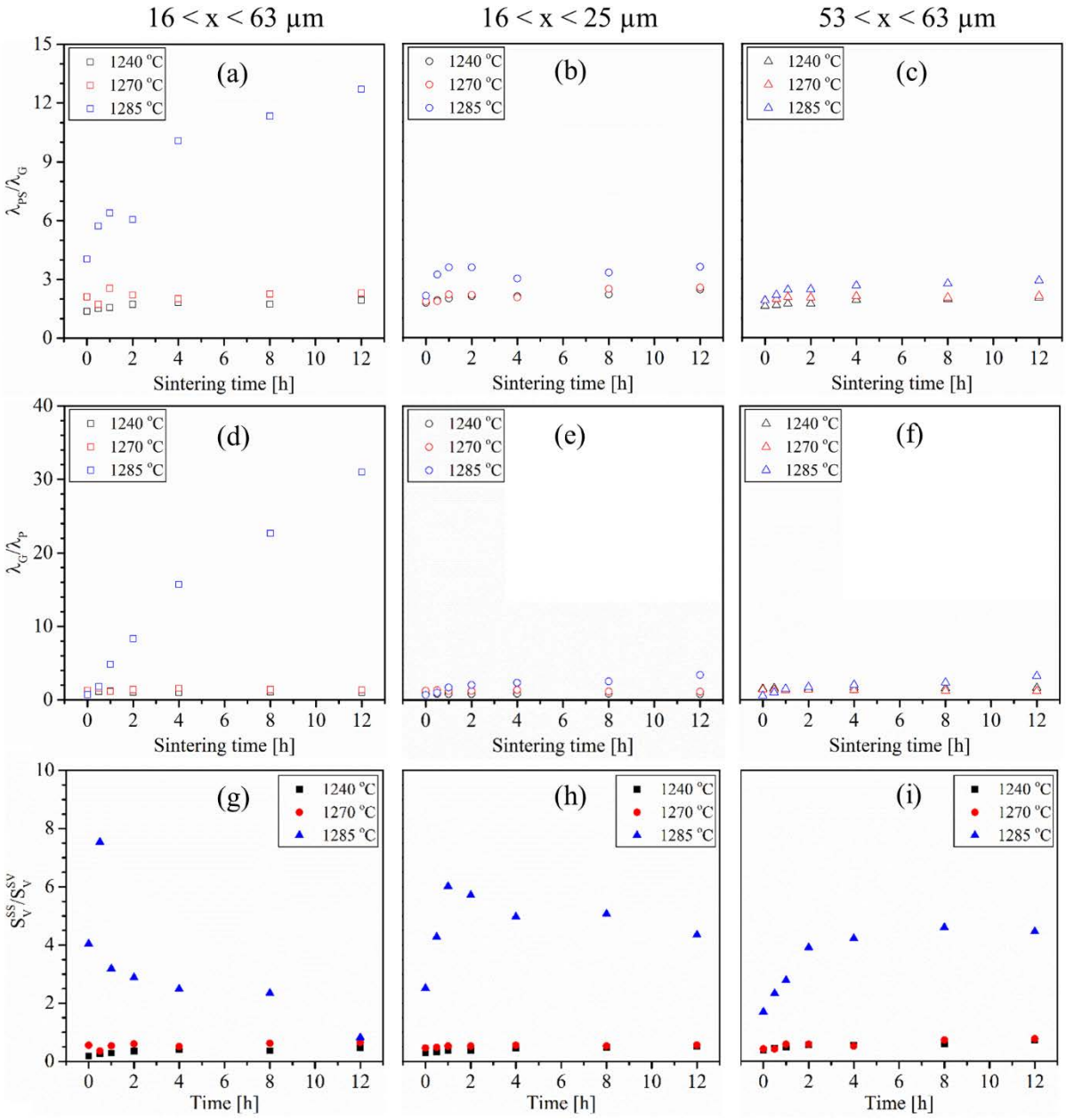

Figure 59. Dimenssionless results vs. sintering time for (a-c) the pore separation to grain intercept ratio, (d-f) the grain to pore intercept ratio, and (g-i) The solid-solid surface area to solid-vapor surface area ratio. Samples were BJ3DP from three different powder sizes and distibutions of alloy 625.

The surface area ratio (ψ) was calculated and presented in Figure 58g-i. It was found that the change in the ratio was negligible for the sintering temperatures of 1240 ºC and 1270 ºC and various holding times, suggesting that even if there was any evolution in the microstructure due to different sintering temperatures and times, the surface area ratio did not change. As the sintering temperature increased to 1280 ºC, different behavior was observed between the 16-63 μm powder and the two other ones (16-25 μm and 53-63 μm powders). For the 16-63 μm powder at the sintering temperature of 1280 ºC, it was seen that the surface area ratio was increased as the holding time increased from 0 h to 0.5 h. Afterward, it was decreased as the holding time increased to 12 h. As a wide powder size distribution was used in the 16-63 μm powder, a relative density of ~96% was achieved for the sample sintered for 0.5 h. The optical micrograph shown in Figure 53 illustrated that a significant pore removal happened in the sintered sample form the 16-63 μm powder for 0.5 h while the grain size remained about the same compared to 0 h, resulting in higher surface area ratio. Although relative density increased within prolonging the holding time, grain growth happened in the microstructure leading to the reduction of S_V^{SS}. However, in the 16-25 μm and 53-63 μm powders, it was seen that the surface area ratio was increased as the holding time changed from 0 h to 12 h (see Figure 58h-i).

The predicted evolutions of dimensionless parameters during densification in the simple geometric models have been previously determined by Nettleship et al. [158,182]. It was proposed that dimensionless parameters can be used to make direct comparisons of coarsening between densification models and experiments, independent of scale. Since Λ, ψ and Σ are independent of the length scale of the microstructure, they are unaffected by self-similar coarsening from the fixed microstructural geometry assumed in the models. ψ is better than Λ or Σ for final stage sintering evaluation due to the assumption that all pores are on grain boundaries in the definition of λ_G. The

final stage sintering model commonly underestimates ψ, which can be explained by the fact that pores in the model are too small relative to the grains and therefore some grain edges and grain corners do not contain pores in the real materials.

The total number of pore sections per unit area is plotted against solid area fraction and/or sintering time in Figure 60. It was found that the total number of pore sections per unit area, N_A, of the samples sintered at 1240 ºC increased as the holding time increased from 0 h to 1h when solid volume fractions were less than 0.7. This is thought to be due to new neck formation during sintering shrinkage. On 2D sections this is characterized by the break-up of the elongated pore sections that did not affect the average pore intercept because of the elongated pore shape. This is observed on the optical micrographs (Figure 51) leading to an increase in N_A. As the sintering temperature increased to 1270 ºC, an approximately linear decrease in N_A was seen with increasing holding time and solid volume fraction through the intermediate stage of sintering. This is thought to be due to elimination of small pore sections. Finally, N_A decreased significantly in the 16-63 μm powder in final stage sintering at 1280 ºC relative to the other powder size distributions due to enhanced elimination of isolated pores.

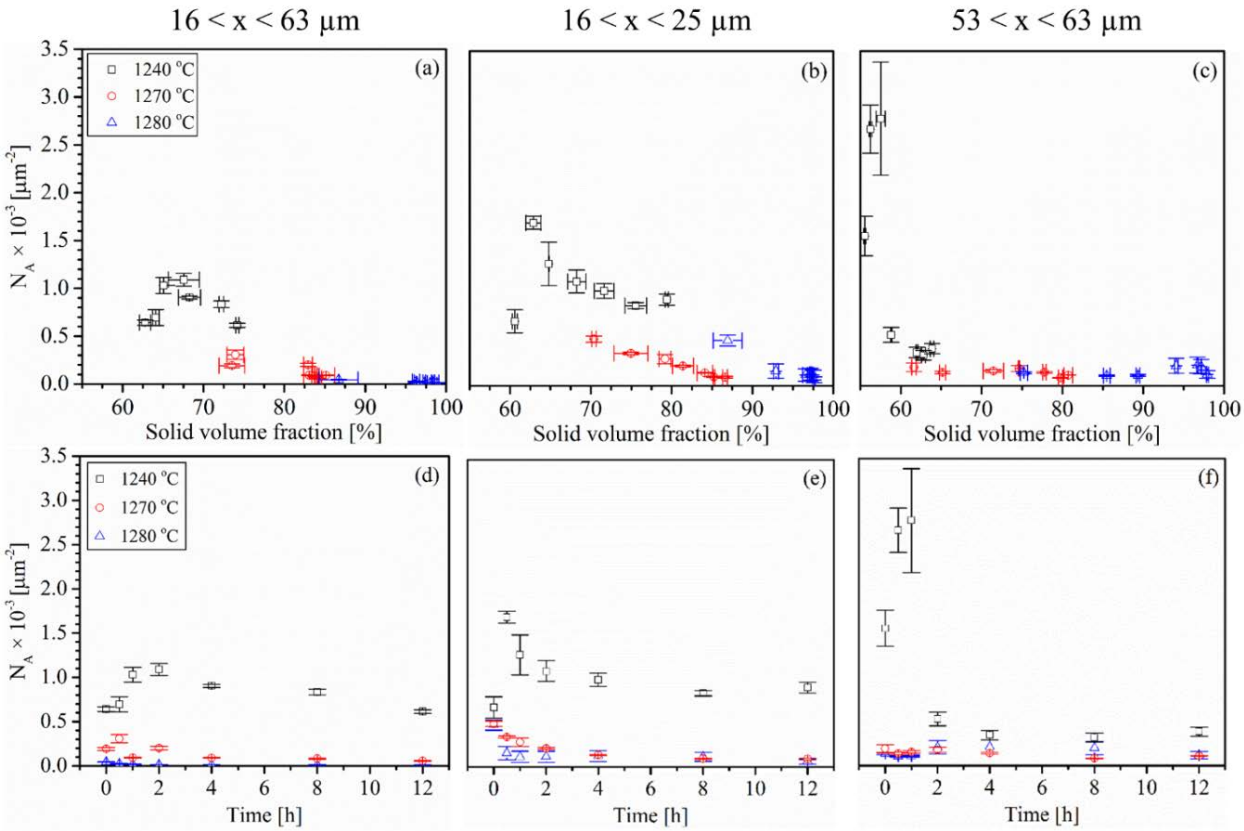

Figure 60. Number of pore sections per unit area against relative density or sintering time for the BJ3DP from three different powder sizes and distibutions of alloy 625.

Figure 61a-c illustrates the relationship between the volume strain rate and the grain size for BJ3DP parts prepared from three sifferent alloy 625 powders which sintered at 1240 °C, 1270 °C and 1280 °C. For each powder size sintered at 1240 °C, the plot gave a grain size exponent of 8.8, 7.12 and 14.35 for the 16-63 µm, 16-25 µm and 53-63 µm powders, respectively, which were all above any reasonable value (3-4) that could represent the effect of grain size on isothermal densification kinetics expected from the models of sintering. This might be attributed to the fact that the grain size was not increasing fast enough to fully explain the decrease in the densification rate during isothermal sintering observed in this study. As the temperature increased to 1270 °C,

a step can be seen in each fitted plot. At the shorter holding times (fittet line is labeled by '*'), the slopes were 3.56, 5.9 and 5.21 while with the prolonged holding time, they decreased to 2.63, 2.46 and 3.34 (fittet line is labeled by '**') for the 16-63 μm, 16-25 μm and 53-63 μm powders, respectively. If only one fitting line was applied at 1270 ºC, the exponents were significantly reduced. Finally, the grain size exponents of the samples sintered at 1280 °C were 4.02, 3.43 and 3.83 for the 16-63 μm, 16-25 μm and 53-63 μm powders, respectively. These values are much closer to those expected and suggest that the grain intercept more accurately represents the diffusion distance and how it evolves. An alternative explanation for the high measured grain size exponents of the samples sintered at 1240 °C compared with the higher sintering temperatures of 1270 °C and 1280 °C can be related to the differences observed in microstructures and the grain growth behavior.

Generally, the lower sintering temperature, 1240 °C, tends to result in a situation in which a significant number of the grain boundaries are retained; while rapid grain growth is observed at higher sintering temperatures and higer densities. In other words, the enhanced grain boundary mobility and/or the mobility of grain edges at higher sintering temperatures of 1270 °C and 1280 °C can reduce the number of grains between pores, resulting in a greater proportion of the grain boundaries being directly inhibited by the pore phase. It is necessary to bear in mind that the use of grain size as a measure of average diffusion distance will be complicated by the spatial arrangement of the pores and grains, and this should be taken into consideration when interpreting the results of sintering experiments. Based on the kinetic models of sintering, the isothermal volume strain rate should have a power-law dependence on the grain size, the latter approximating the controlling diffusion distance. It has been predicted that the different sintering mechanisms have different grain size exponents, and typically, experimental measurement of the grain size

exponent have, in the past, been used to identify the sintering mechanism. A grain size exponent of 4 suggests that densification could be attributed to grain-boundary diffusion, while an exponent of 3 has been used to indicate that densification occurs by volume diffusion. It was found that the time exponent (n) is decreasing with the increase in sintering temperature. Besides, it was worth noting that although the grain size exponent was very high for the sintering temperature of 1240 °C, there was still a strong correlation between the grain size and the volume strain rate suggesting a real but somewhat more complicated relationship. At 1280 °C, it was thought that the grain boundary diffusion was the dominant sintering mechanism for the 16-63 μm, 53-63 μm powders and the 16-25 μm powder, it was thought that grain boundary diffusion could be the main sintering mechanism.

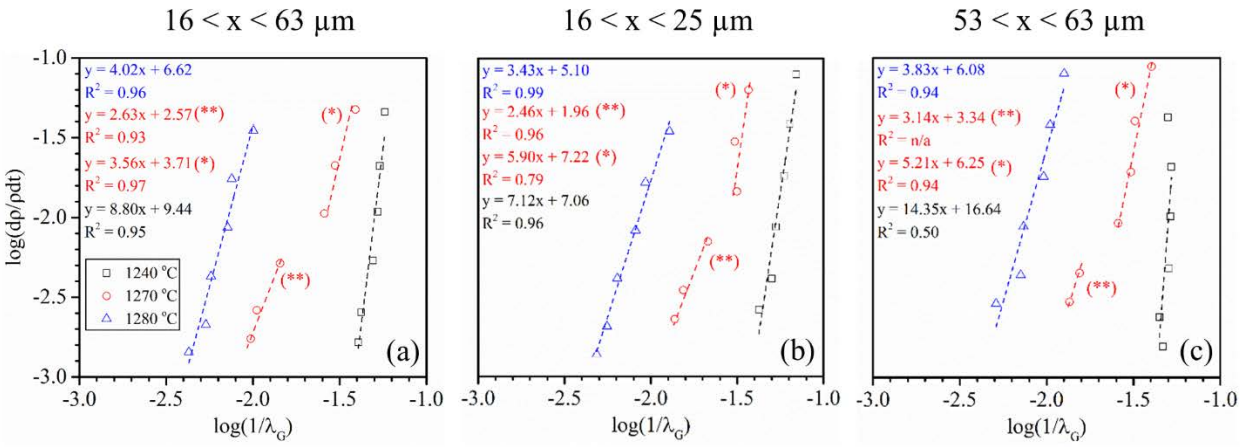

Figure 61. Plot of log volume strain rate against log inverse intercept length of grain intercept for the BJ3DP from three different powder sizes and distibutions of alloy 625.

The sintering process is a critical step in binder jet 3D printing technology (BJ3DP) since the densification of the green part. Unlike compacted P/M parts, the green densities of binder jet 3D printed parts are low, in the density range ~40-60%. Depending on the morphology, particle

size and powder size distribution, it is possible to improve green part density. Powder packing density is an important criteria in powder bed additive manufacturing processes in which the higher packing density can lead to less shrinkage in the final part. Consequently, lower sintering shrinkages would be expected to improve dimensional control and uniformity in part. Therefore, the use of powders with wide size distributions can be beneficial. The driving force of the sintering is primarily based on the reduction of surface energy of the BJ3DP part and the diffusional processes at the sintering temperature. Figure 62 illustrates the microstructural evolution of the printed parts through the three stages of the sintering process. Prior to sintering, the green part density of the BJ3DP specimens from the three types of alloy 625 powders were about 52%, 45% and 48% for the 16-63 μm, 16-25 μm and 53-63 μm powders, respectively. The differences in green density are due to differences in packing of the particles. The initial stage of sintering happens at lower temperatures. Initially, particles that are in contact form necks at the contact point through the diffusion processes of densification. Necks begin to form at the contact points between the adjacent particles without much dimensional change or porosity reduction. Generally, neck growth happens with increasing the sintering temperature or prolonging the holding time causing a linear shrinkage (dimensional changes) [93–95]. In this study, the 16-25 μm powder which gave the lowest green densities showed slightly higher linear shrinkage compared to the 16-63 μm and 53-63 μm powders. It is worth noting that printing lines were seen at the cross section of the 16-25 μm powder while no continuous lines of pores were found on the cross section of printed samples made from 16-63 μm and 53-63 μm powders. As the layer thickness during printing process is 100 μm, the chance of powder compaction using roller is higher for the 16-63 μm and 53-63 μm powders. In fact, smaller powder particles have lower powder packing rate and therefore cause higher porosity in the powder bed.

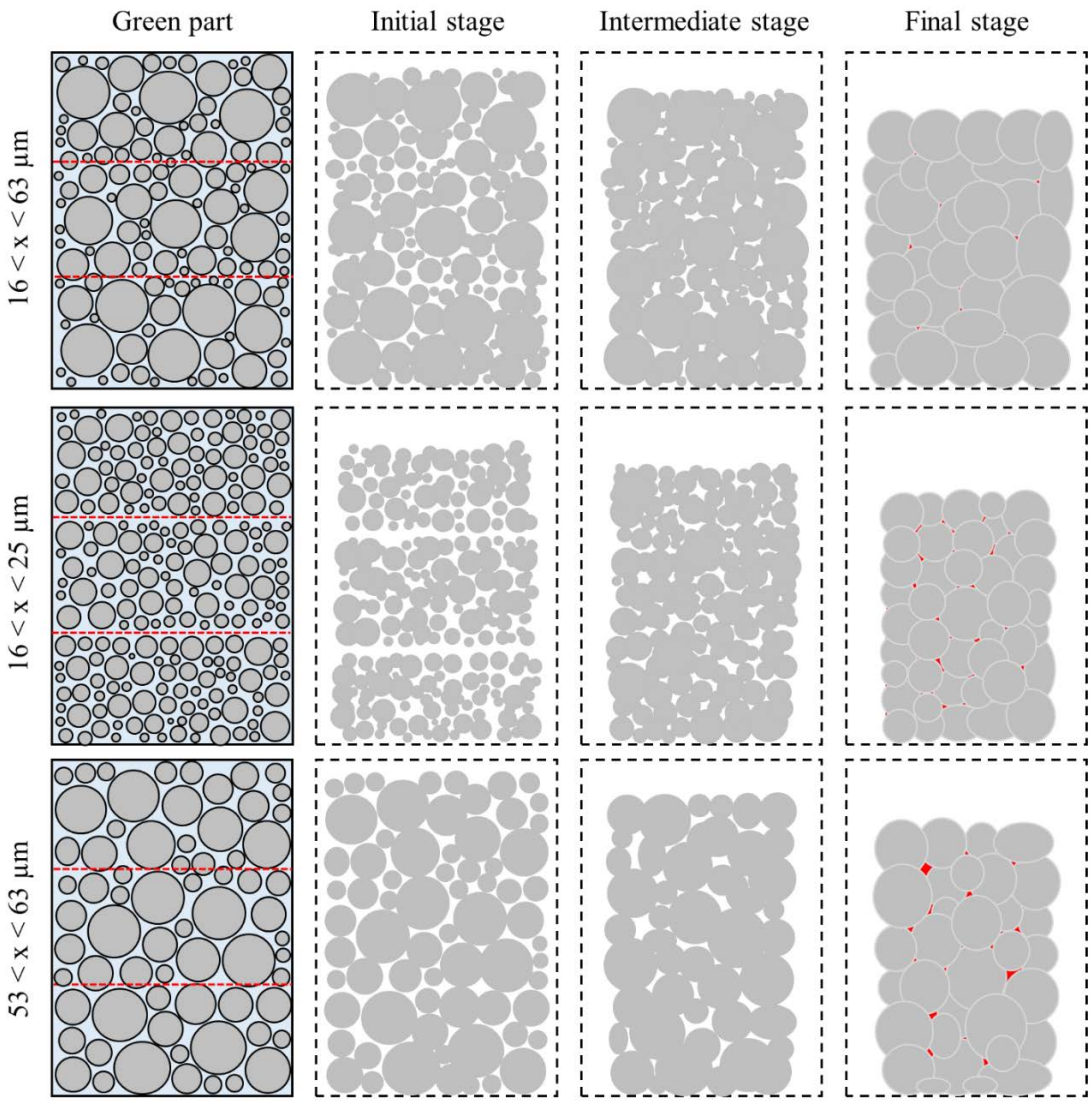

Figure 62. Schematic of the green parts, initial, intermediate and final stage of sintering of the BJ3DP parts from three different powder sizes and distibutions of alloy 625. Red dash lines shown in green parts are indicative of the printed layers with 100 µm thickness. After sintering, samples experienced shrinkage. In the final stage of sintering, residual pores are displayed by red color.

The particle size and particle size distribution are important parameters in BJ3DP affecting flowability of the powder particles during printing step. Lu et al. [38] used TiNiHf powder with different powder size distributions. They observed that large particles are preferred for binder

jetting due to its excellent flowability and low surface area; while, fine powder can spread as slurry due to high surface area and its propensity to easily absorb moisture leading agglomeration and less powder flowability. The packing of the particles and the consequent green density also effect the initial stage of sintering. The lower green density associated with the finer particles can lead to more spatially heterogeneous neck formation that extends initial stage sintering to higher density.

Intermediate stage was more rapid at higher temperatures (1270 ºC and 1280 ºC) where the part experiences significant evolution in density as shown in Figure 62. During the intermediate stage further neck growth and pore filling will give pore sections that are more discontinuous on 2D sections resulting in a mixture of elongated pore sections in the plane of the section and smaller more equiaxed pore sections derived from elongated pores that are oriented perpendicular to the plane of polish. Notice that pore intercept analysis will be biased to directions perpendicular to the axis of elongated pore sections and so the pore shape results in pore intercepts that do not reflect the larger pore area of the larger elongated pores. While it is in general assumed that sintering at 1280 ºC was still fully in solid state, SEM micrographs suggest that a very small liquid film might have formed on powder particles, assisting and accelerating densification (see Figure 63).

As the density increases to ~92% the pores close and the microstructure enters final stage. The densification rate in this stage is much slower than the initial and intermediate stages. During this stage, elimination of the closed pores takes place to achieve final density. Throughout the final sintering stage, grain coarsening can be rapid. Importantly the pore intercept remained constant for the two narrower particle size distributions but decreased for the samples made from the powder with wider particle size distribution. This was correlated with relatively high final density. However, it has been reported by Koseski et al. [47] on the injection molded 316L stainless steel

powder and Dourandish et al. [181] on the P/M Co-based alloy that pore coarsening may happen during final stage sintering. In fact, differences in the pore curvature can result in growth of the large pores at the expense of the smaller stable pores. Similar results on the pore coarsening of the binder jetted alloy 625 was reported by Mostafaei et al. in [52].

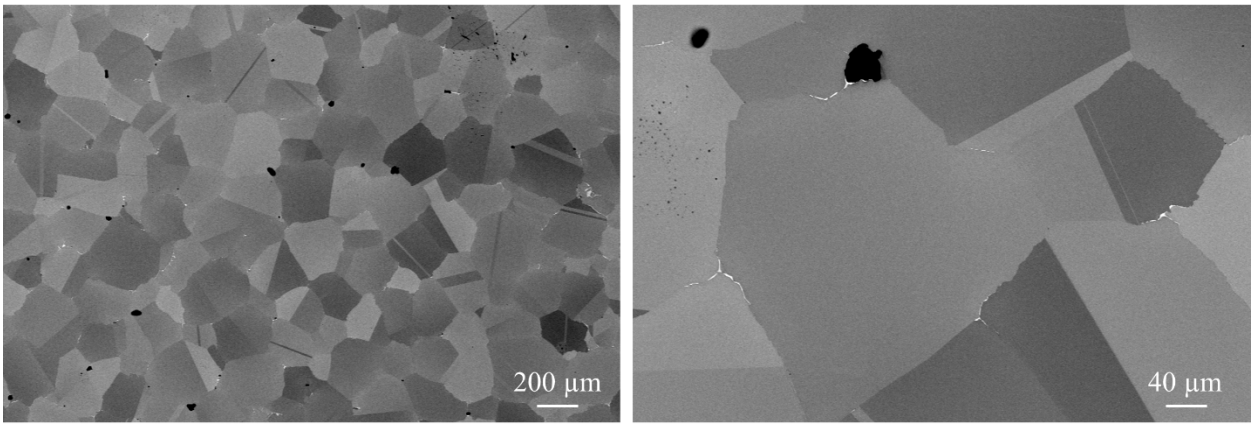

Figure 63. SEM micrographs taken from the 16-63 µm powder sintered at 1280 °C for 4 h. A very small liquid film was observed at the boundaries.

6.3.1 Summary

Here, we investigated the microstructural evolution during sintering of the binder jetted parts from three different sets of alloy 625 powders. Binder jet 3D printing parameters including layer thickness, binder saturation and drying time were kept constant to study the effect of particle size and powder size distribution on the kinetics of densification. The following conclusions are drawn:

1. During densification studies of parts sintered between 1225 °C and 1300 °C for 4 h, powder particle of the 16-25 μm showed higher linear shrinkage compared to the 16-63 μm and 53-63 μm powders. Additionally, it was seen that as the sintering temperature increased to 1285 °C, linear shrinkage in z direction was higher than x and y directions in 16-25 μm. Similarly, densification was faster in the 16-25 μm powder up to 1270 °C but at the higher sintering temperature, the 16-63 μm powder showed higher densification rate.
2. Densification kinetic studies showed that at 1240 °C, solid-state sintering was dominant in which the 16-25 μm powder had higher densification rate and linear shrinkage than the two other powders. As the sintering temperature increased to 1270 °C the microstructural observations showed that the 16-63 μm powder could reach a maximum density of ~99% after sintering for 8 h at 1280 °C while the 16-25 μm and 53-63 μm powders had pores even after sintering at 1280 °C for 12h.
3. Stereological measurements including solid volume fraction, grain/pore intercept length, pore separation, surface area per unit volume, and number of pore sections per unit area were obtained from optical micrographs. Dramatic grain growth happened in all samples after sintering at 1280 °C for 12h. Additionally, pore intercept results showed that it was only possible to eliminate pores in the BJ3DP part from the 16-63 μm powder after sintering at 1280 °C for 4 h or longer while pores removal was not achieved in two other powders.
4. Dimensionless parameters such as intercept ratio (Λ), surface area ratio (ψ) and the mean pore spacing to mean grain intercept length ratio (Σ) were used to make direct comparisons of nature of the microstructural coarsening in the samples. Σ increased for the 16-63 μm powder sintered at 1280 °C for 1 h or longer, meaning that the pore separation grew faster than grains while no such change were seen for the 16-25 μm and 53-63 μm powders.. For the 16-63 μm powder,

the number of pore sections per unit area results indicated that the number of pores significantly decreased as the holding time increased to 1 h at 1280 ºC. Additionally, grain growth happened when prolonging the sintering time at 1280 °C. During the microstructural evolution in the 16-63 μm powder, grain growth happened rapidly meaning that the solid/solid boundary decreased faster than solid/vapor boundary and therefore leading to the reduction in the ψ in the 16-63 μm powder.

5. The relationship between the volume strain rate and the grain size were measured for all samples sintered at three different temperatures. At low sintering temperature of 1240 °C, the exponent values were high and could be attributed to the fact that the grain size was not increasing fast enough to fully explain the decrease in the densification rate during isothermal sintering. This suggested that grain size was not an appropriate length-scale to represent the diffusion distance in real systems for the kinetic models of sintering. However, at 1270 °C and 1280 °C, the exponent values were between 2 and 5 which could be more reasonably interpreted based on the diffusion mechanism and the commonly accepted models of sintering.

7.0 FUTURE WORK

1. Densification study on the water atomized powder with different powder mean size and distribution spans. Besides, the effect of bi- or tri-modal powder size distribution on the densification behavior of alloy 625 can be of interest. Since production of water atomized powder is cheaper than gas atomized powder, it is worth studying the possibility of part production with ~ 99% density made from water atomized powder. A cyclic sintering profile is suggested so that the sintering temperature may reach to a high temperature of 1285 °C and then is cooled down to below solidus temperature. By doing so, densification may be assisted due to short term liquid phase formation followed by solid state sintering.
2. Optimization of printing parameters such as layer thickness, binder saturation and drying time on the green density of BJ3DP parts from fine particles of gas atomized alloy 625. Additionally, densification kinetics, microstructural evolution and mechanical properties of the fully dense part from fine powder is of interest and needs to be compared with presented results in this study.
3. Effect of surface finish on the fatigue behavior is a well-known aspect. In this research, as-sintered and mechanically ground samples were tested and fatigue life was compared with the cast alloy 625. Other surface treatments such as sand blast, electrochemical etching and wire electrical discharge machining (EDM) can be applied on the samples and fatigue life can be evaluated.

4. There is limited information of the corrosion behavior of BJ3DP parts specifically alloy 625. High temperature corrosion in different corrosive environment and electrochemical behavior in various solutions of the BJ3DP alloy 625 parts may be of interest since this alloy has application in oil and petroleum, aerospace and in general harsh environments. Besides, high temperature crack susceptibility of this alloy can be studied.

BIBLIOGRAPHY

[1] K. Ullakko, J.K. Huang, C. Kantner, R.C. O'Handley, V. V. Kokorin, Large magnetic-field-induced strains in Ni2MnGa single crystals, Appl. Phys. Lett. 69 (1996) 1966.

[2] J. Pons, V.A. Chernenko, R. Santamarta, E. Cesari, Crystal structure of martensitic phases in Ni–Mn–Ga shape memory alloys, Acta Mater. 48 (2000) 3027–3038.

[3] M. Elahinia, N. Shayesteh Moghaddam, M. Taheri Andani, A. Amerinatanzi, B.A. Bimber, R.F. Hamilton, Fabrication of NiTi through additive manufacturing: A review, Prog. Mater. Sci. 83 (2016) 630–663.

[4] B.Q. Lin J, Review and Analysis of Powder Prior Boundary (PPB) Formation in Powder Metallurgy Processes for Nickel-based Super Alloys, J. Powder Metall. Min. 4 (2015) 1–6.

[5] M.H. Elahinia, M. Hashemi, M. Tabesh, S.B. Bhaduri, Manufacturing and processing of NiTi implants: A review, Prog. Mater. Sci. 57 (2012) 911–946.

[6] L.E. Murr, E. Martinez, K.N. Amato, S.M. Gaytan, J. Hernandez, D. a. Ramirez, P.W. Shindo, F. Medina, R.B. Wicker, Fabrication of Metal and Alloy Components by Additive Manufacturing: Examples of 3D Materials Science, J. Mater. Res. Technol. 1 (2012) 42–54.

[7] W.E. Frazier, Metal Additive Manufacturing : A Review, J. Mater. Eng. Perform. 23 (2014) 1917–1928.

[8] W.J. Sames, F.A. List, S. Pannala, R.R. Dehoff, S.S. Babu, The metallurgy and processing science of metal additive manufacturing, Int. Mater. Rev. 61 (2016) 315–360.

[9] T. DebRoy, H.L. Wei, J.S. Zuback, T. Mukherjee, J.W. Elmer, J.O. Milewski, A.M. Beese, A. Wilson-Heid, A. De, W. Zhang, Additive manufacturing of metallic components – Process, structure and properties, Prog. Mater. Sci. 92 (2018) 112–224.

[10] S. Bose, D. Ke, H. Sahasrabudhe, A. Bandyopadhyay, Additive Manufacturing of Biomaterials, Prog. Mater. Sci. 93 (2017) 45–111.

[11] B. Bhushan, M. Caspers, An overview of additive manufacturing (3D printing) for microfabrication, Microsyst. Technol. 23 (2017) 1117–1124.

[12] E. Sachs, M. Cima, J. Cornie, D. Brancazio, J. Bredt, A. Curodeau, T. Fan, S. Khanuja, A. Lauder, J. Lee, S. Michaels, Three-dimensional printing: the physics and implications of additive manufacturing, Ann. CIRP. 42 (1993) 257–260.

[13] W.Y. Zhou, S.H. Lee, M. Wang, W.L. Cheung, W.Y. Ip, Selective laser sintering of porous tissue engineering scaffolds from poly(L-lactide)/carbonated hydroxyapatite nanocomposite microspheres, J. Mater. Sci. Mater. Med. 19 (2008) 2535–2540.

[14] J.P.P. Kruth, L. Froyen, J. Van Vaerenbergh, P. Mercelis, M. Rombouts, B. Lauwers, Selective laser melting of iron-based powder, J. Mater. Process. Technol. 149 (2004) 616–622.

[15] S. Wieland, F. Petzoldt, Binder Jet 3D-Printing for metal additive manufacturing: Applications and innovative approaches, CFI Ceram. Forum Int. 93 (2016) E26–E30.

[16] J. Giannatsis, V. Dedoussis, Additive fabrication technologies applied to medicine and health care: A review, Int. J. Adv. Manuf. Technol. 40 (2009) 116–127.

[17] A. Dawood, B.M. Marti, V. Sauret-Jackson, A. Darwood, 3D printing in dentistry, Br. Dent. J. 219 (2015) 521–529.

[18] N. Guo, M.C. Leu, Additive manufacturing: Technology, applications and research needs, Front. Mech. Eng. 8 (2013) 215–243.

[19] A. Mostafaei, K.A. Kimes, E.L. Stevens, J. Toman, Y.L. Krimer, K. Ullakko, M. Chmielus, Microstructural evolution and magnetic properties of binder jet additive manufactured Ni-Mn-Ga magnetic shape memory alloy foam, Acta Mater. 131 (2017) 482–490.

[20] E.M. Sachs, J.S. Haggerty, M.J. Cima, P.A. Williams, Three-Dimensional Printing Techniques, US5340656 A, 1993.

[21] S.M. Allen, E.M. Sachs, Three-dimensional printing of metal parts for tooling and other applications, Met. Mater. Int. 6 (2000) 589–594.

[22] H. Shao, D. Zhao, T. Lin, J. He, J. Wu, 3D gel-printing of zirconia ceramic parts, Ceram. Int. 43 (2017) 13938–13942.

[23] S.L. Taylor, R.N. Shah, D.C. Dunand, Ni-Mn-Ga micro-trusses via sintering of 3D-printed inks containing elemental powders, Elsevier B.V., 2018.

[24] M.P. Paranthaman, C.S. Shafer, A.M. Elliott, D.H. Siddel, M.A. McGuire, R.M. Springfield, J. Martin, R. Fredette, J. Ormerod, Binder Jetting: A Novel NdFeB Bonded Magnet Fabrication Process, Jom. 68 (2016) 1978–1982.

[25] A. Mostafaei, Y. Behnamian, Y.L. Krimer, E.L. Stevens, J.L. Luo, M. Chmielus, Effect of solutionizing and aging on the microstructure and mechanical properties of powder bed binder jet printed nickel-based superalloy 625, Mater. Des. 111 (2016) 482–491.

[26] P. Nandwana, A.M. Elliott, D. Siddel, A. Merriman, W.H. Peter, S.S. Babu, Powder bed binder jet 3D printing of Inconel 718: Densification, microstructural evolution and challenges, Curr. Opin. Solid State Mater. Sci. 12 (2017) 1–12.

[27] R.K. Enneti, K.C. Prough, T.A. Wolfe, A. Klein, N. Studley, J.L. Trasorras, Sintering of WC-12%Co processed by binder jet 3D printing (BJ3DP) technology, Int. J. Refract. Met. Hard Mater. 71 (2017) 28–35.

[28] M.P. Watters, M.L. Bernhard, Modified curing protocol for improved strength of binder-jetted 3D parts, Rapid Prototyp. J. 10 (2004) 5–6.

[29] H. Miyanaji, S. Zhang, A. Lassell, A. Zandinejad, L. Yang, Process Development of Porcelain Ceramic Material with Binder Jetting Process for Dental Applications, Jom. 68 (2016) 831–841.

[30] Y.L. Yap, C. Wang, S.L. Sing, V. Dikshit, W.Y. Yeong, J. Wei, Material jetting additive manufacturing: An experimental study using designed metrological benchmarks, Precis. Eng. 50 (2017) 275–285.

[31] E.O. Garzón, J.L. Alves, R.J. Netvo, Post-process Influence of Infiltration on Binder Jetting Technology, in: Mater. Des. Appl. Adv. Struct. Mater., 2017: p. Springer, Cham.

[32] A. Levy, A. Miriyev, A. Elliott, S.S. Babu, N. Frage, Additive manufacturing of complex-shaped graded TiC/steel composites, Mater. Des. (2017).

[33] A. Mostafaei, J. Toman, E.L. Stevens, E.T. Hughes, Y.L. Krimer, M. Chmielus, Microstructural evolution and mechanical properties of differently heat-treated binder jet printed samples from gas- and water-atomized alloy 625 powders, Acta Mater. 124 (2017) 280–289.

[34] A. Mostafaei, E.T. Hughes, C. Hilla, E.L. Stevens, M. Chmielus, Data on the densification during sintering of binder jet printed samples made from water- and gas-atomized alloy 625 powders, Data Br. 10 (2017) 116–221.

[35] A. Mostafaei, E.L. Stevens, J.J. Ference, D.E. Schmidt, M. Chmielus, Binder jet printing of partial denture metal framework from metal powder, in: Mater. Sci. Technol., 2017: pp. 289–291.

[36] ExOne company, http://www.exone.com/Systems/Production-Printers, (n.d.).

[37] Y. Bai, G. Wagner, C.B. Williams, Effect of Particle Size Distribution on Powder Packing and Sintering in Binder Jetting Additive Manufacturing of Metals, J. Manuf. Sci. Eng. 139 (2017) 81019.

[38] K. Lu, M. Hiser, W. Wu, Effect of particle size on three dimensional printed mesh structures, Powder Technol. 192 (2009) 178–183.

[39] M. Vaezi, C.K. Chua, Effects of layer thickness and binder saturation level parameters on

3D printing process, Int. J. Adv. Manuf. Technol. 53 (2011) 275–284.

[40] W. Zhang, R. Melcher, N. Travitzky, R.K. Bordia, P. Greil, Three-dimensional printing of complex-shaped alumina/ glass composites, Adv. Eng. Mater. 11 (2009) 1039–1043.

[41] S. Cao, Y. Qiu, X.-F. Wei, H.-H. Zhang, Experimental and theoretical investigation on ultra-thin powder layering in three dimensional printing (3DP) by a novel double-smoothing mechanism, J. Mater. Process. Technol. 220 (2015) 231–242.

[42] A.T. Sutton, C.S. Kriewall, M.C. Leu, J.W. Newkirk, Powders for Additive Manufacturing Processes: Characterization Techniques and Effects on Part Properties, Solid Free. Fabr. Proc. (2016) 1004–1030.

[43] M. Valdek, K. Helmo, K. Pritt, M. Besterci, Characterization of Powder Particle, Methods. 7 (2001) 22–34.

[44] P.K. Samal, J.W. Newkirk, Powder Metallurgy, Metal Powder Characterization, Bulk Properties of Powders, ASM Handb. 7 (2015) 93–168.

[45] J.M. Contreras, A. Jiménez-Morales, J.M. Torralba, Improvement of rheological properties of Inconel 718 MIM feedstock using tailored particle size distributions, Powder Metall. 51 (2008) 103–106.

[46] B.N. Nobrega, W. Ristow, Jr, R. Machado, MIM processing and plasma sintering of nickel base superalloys for aerospace and automotive applications, Powder Metall. 51 (2008) 107–110.

[47] R.P. Koseski, P. Suri, N.B. Earhardt, R.M. German, Y.-S. Kwon, Microstructural evolution of injection molded gas- and water-atomized 316L stainless steel powder during sintering, Mater. Sci. Eng. A. 390 (2005) 171–177.

[48] H.Ö. Gülsoy, S. Özbek, T. Baykara, Microstructural and mechanical properties of injection moulded gas and water atomised 17-4 PH stainless steel powder, Powder Metall. 50 (2007) 120–126.

[49] L. Zhang, X. Chen, D. Li, C. Chen, X. Qu, X. He, Z. Li, A comparative investigation on MIM418 superalloy fabricated using gas- and water-atomized powders, Powder Technol. 286 (2015) 798–806.

[50] R. Li, Y. Shi, Z. Wang, L. Wang, J. Liu, W. Jiang, Densification behavior of gas and water atomized 316L stainless steel powder during selective laser melting, Appl. Surf. Sci. 256 (2010) 4350–4356.

[51] M. Rombouts, G. Maes, M. Mertens, W. Hendrix, Laser metal deposition of Inconel 625: Microstructure and mechanical properties, J. Laser Appl. 24 (2012) 52007.

[52] A. Mostafaei, E.L. Stevens, E.T. Hughes, S.D. Biery, C. Hilla, M. Chmielus, Powder bed binder jet printed alloy 625: Densification, microstructure and mechanical properties,

Mater. Des. 108 (2016) 126–135.

[53] Y.F. Ternovoi, A.G. Tsipunov, S.B. Kuratchenko, O.M. Kuimova, K. V. Kondakova, Pore formation in atomized powder, Sci. York. 99 (1985) 50–52.

[54] A. Mostafaei, C. Hilla, E.L. Stevens, P. Nandwana, A.M. Elliott, M. Chmielus, Comparison of characterization methods for differently atomized nickel-based alloy 625 powders, Powder Technol. 333 (2018) 180–192.

[55] K. Heim, F. Bernier, R. Pelletier, L.-P. Lefebvre, High resolution pore size analysis in metallic powders by X-ray tomography, Case Stud. Nondestruct. Test. Eval. 6 (2016) 45–52.

[56] J.H. Tan, W.L.E. Wong, K.W. Dalgarno, An overview of powder granulometry on feedstock and part performance in the selective laser melting process, Addit. Manuf. 18 (2017) 228–255.

[57] E. Börjesson, J. Karlsson, F. Innings, C. Trägårdh, B. Bergenståhl, M. Paulsson, Entrapment of air during imbibition of agglomerated powder beds, J. Food Eng. 201 (2017) 26–35.

[58] R.P. Zou, M.L. Gan, A.B. Yu, Prediction of the porosity of multi-component mixtures of cohesive and non-cohesive particles, Chem. Eng. Sci. 66 (2011) 4711–4721.

[59] M. a P. J. A. Slotwinski, E. J. Garboczi, P. E. Stutzman, C. F. Ferraris, S. S. Watson, Additive Manufacturing, J. Res. Natl. Inst. Standars Technol. 119 (2014) 460–493.

[60] B.L. DeCost, H. Jain, A.D. Rollett, E.A. Holm, Computer Vision and Machine Learning for Autonomous Characterization of AM Powder Feedstocks, Jom. 69 (2017) 456–465.

[61] H. Chen, Q. Wei, S. Wen, Z. Li, Y. Shi, Flow behavior of powder particles in layering process of selective laser melting: Numerical modeling and experimental verification based on discrete element method, Int. J. Mach. Tools Manuf. 123 (2017) 146–159.

[62] K.P. Hapgood, J.D. Litster, S.R. Biggs, T. Howes, Drop Penetration into Porous Powder Beds, J. Colloid Interface Sci. 253 (2002) 353–366.

[63] Z. Zhou, F. Buchanan, C. Mitchell, N. Dunne, Printability of calcium phosphate: Calcium sulfate powders for the application of tissue engineered bone scaffolds using the 3D printing technique, Mater. Sci. Eng. C. 38 (2014) 1–10.

[64] R.K. McGeary, Mechanical Packing of Spherical Particles, J. Am. Ceram. 44 (1961) 513–522.

[65] H. Miyanaji, S. Zhang, L. Yang, A new physics-based model for equilibrium saturation determination in binder jetting additive manufacturing process, Int. J. Mach. Tools Manuf. 124 (2018) 1–11.

[66] J.F. Bredt, Binder Stability and Powder\Binder Interaction in Three Dimensional Printing,

Dept. of Mechanical Engineering, Massachusetts Institute of Technology,–Cambridge, 1995.

[67] S. Shrestha, G. Manogharan, Optimization of Binder Jetting Using Taguchi Method, Jom. 69 (2017) 491–497.

[68] E.J.R. Parteli, T. Pöschel, Particle-based simulation of powder application in additive manufacturing, Powder Technol. 288 (2016) 96–102.

[69] H. Miyanaji, N. Momenzadeh, L. Yang, Effect of printing speed on quality of printed parts in Binder Jetting Process, Addit. Manuf. 20 (2018) 1–10.

[70] H. Miyanaji, L. Yang, Equilibrium Saturation in Binder Jetting Additive Manufacturing Processes: Theoretical Model Vs. Experimental Observeations, in: 27th Annu. Int. Solid Free. Fabr. Symp. – An Addit. Manuf., 2016: pp. 1945–1959.

[71] A.C. Hoffmann, H.J. Finkers, A relation for the void fraction of randomly packed particle beds, Powder Technol. 82 (1995) 197–203.

[72] A.B. Spierings, G. Levy, Comparison of density of stainless steel 316L parts produced with selective laser melting using different powder grades, Solid Free. Fabr. Proc. (2009) 342–353.

[73] A. Cooke, J. Slotwinski, Properties of metal powders for additive manufacturing: A review of the state of the art of metal powder property testing, Addit. Manuf. Mater. Stand. Test. Appl. (2015) 21–48.

[74] a. Simchi, The role of particle size on the laser sintering of iron powder, Metall. Mater. Trans. B. 35 (2004) 937–948.

[75] A.M. Elliott, P. Nandwana, D. Siddel, B.G. Compton, A Method for Measuring Powder Bed Density in Binder Jet Additive Manufacturing Process and the Powder Feedstock Characteristics Influencing the Powder Bed Density, Solid Free. Fabr. 2016. Proceeding (2016) 1031–1037.

[76] R.M. German, Particle Packing Characteristics, Metal Powder Industries Federation, Princeton N.J, 1989.

[77] R.K. McGEARY, Mechanical Packing of Spherical Particles, J. Am. Ceram. Soc. 44 (1961) 513–522.

[78] G. Egger, P.E. Gygax, R. Glardon, N.P. Karapatis, Optimization of powder layer density in selective laser sintering, 10th Solid Free. Fabr. Symp. (1999) 255–263.

[79] H.H. Zhu, J.Y.H. Fuh, L. Lu, The influence of powder apparent density on the density in direct laser-sintered metallic parts, Int. J. Mach. Tools Manuf. 47 (2007) 294–298.

[80] R.M. German, Prediction of sintered density for bimodal powder mixtures, Metall. Trans.

A. 23 (1992) 1455–1465.

[81] C.T. Schade, T.F. Murphy, C. Walton, Development of atomized powders for additive manufacturing, World Congr. Powder Metall. Part. Mater. PM 2014, May 18, 2014 - May 22, 2014. (2014) 215–226.

[82] S.-J.J. Lee, Powder Layer Generation for Three Dimensional Printing, Massachusetts Institute of Technology, Cambridge, MA, 1992.

[83] J.F. Bredt, T.C. Anderson, D.B. Russell, Three dimensional printing material system and method. US6610429 B2, 2003.

[84] J.F. Bredt, S. Clark, G. Gilchrist, Three dimensional printing material system and method. US7087109 B2, 2006.

[85] M.A. Caradonna, M.J. Cima, J. Grau, J. Moon, E.M. Sachs, P.C. Saxton, J.G. Serdy, S.A. Uhland, Jetting layers of powder and the formation of fine powder beds thereby. EP1009614 A1, 2000.

[86] B. Khoshnevis, Selective inhibition of bonding of power particles for layered fabrication of 3-D objects. US6589471 B1, 2003.

[87] B. Derby, Inkjet Printing of Functional and Structural Materials: Fluid Property Requirements, Feature Stability, and Resolution, Annu. Rev. Mater. Res. 40 (2010) 395–414.

[88] H. Chen, H. Chen, Y.F. Zhao, Y.F. Zhao, Process parameters optimization for improv- ing surface quality and manufacturing accuracy of binder jetting additive manufacturing process, Rapid Prototyp. J. 22 (2016) 527–538.

[89] H. Fayazfar, M. Salarian, A. Rogalsky, D. Sarker, P. Russo, V. Paserin, E. Toyserkani, A critical review of powder-based additive manufacturing of ferrous alloys: Process parameters, microstructure and mechanical properties, Mater. Des. 144 (2018) 98–128.

[90] K. Lu, W.T. Reynolds, 3DP process for fine mesh structure printing, Powder Technol. 187 (2008) 11–18.

[91] C.B. Williams, J.K. Cochran, D.W. Rosen, Additive manufacturing of metallic cellular materials via three-dimensional printing, Int. J. Adv. Manuf. Technol. 53 (2011) 231–239.

[92] T. Do, C.S. Shin, D. Stetsko, G. VanConant, A. Vartanian, S. Pei, P. Kwon, Improving Structural Integrity with Boron-based Additives for 3D Printed 420 Stainless Steel, Procedia Manuf. 1 (2015) 263–272.

[93] R.M. German, Coarsening in sintering: Grain shape distribution, grain size distribution, and grain growth kinetics in solid-pore systems, Crit. Rev. Solid State Mater. Sci. 35 (2010) 263–305.

[94] J.G.R. Rockland, The determination of the mechanism of sintering, Acta Metall. 15 (1967) 277–286.

[95] G.. Kuczynski, The mechanism of densification during sintering of metallic particles, Acta Metall. 4 (1956) 58–61.

[96] W.D. Kingery, M.D. Narasimhan, Densification during Sintering in the Presence of a Liquid Phase. II. Experimental, J. Appl. Phys. 30 (1959) 307–310.

[97] E. Wheat, M. Vlasea, J. Hinebaugh, C. Metcalfe, Sinter structure analysis of titanium structures fabricated via binder jetting additive manufacturing, Mater. Des. (2018).

[98] J.L. Johnson, R.M. German, Theoretical modeling of densification during activated solid-state sintering, Metall. Mater. Trans. A Phys. Metall. Mater. Sci. 27 (1996) 441–450.

[99] Y. Kornyushin, Thermodynamic theory of sintering and swelling, Metallofiz. I Noveishie Tekhnologii. 29 (2007) 949–970.

[100] R.M. German, Thermodynamics of sintering, in: Sinter. Adv. Mater., 2010: pp. 3–32.

[101] M.N. Rahaman, Kinetics and mechanisms of densification, in: Sinter. Adv. Mater., 2010: pp. 33–64.

[102] W.D. Kingery, M. Berg, Study of the Initial Stages of Sintering by Viscous Flow, Evaporation—Condensation, and Self-Diffusion, Sinter. Key Pap. SE - 22. 1160 (1990) 367–382. doi:10.1007/978-94-009-0741-6_22.

[103] M.N. Rahaman, Ceramic processing and sintering, 2nd Edition, Taylor and Francis, (2003).

[104] L. Zhang, D. Li, X. Qu, M. Qin, X. He, Z. Li, Microstructure and tensile properties optimization of MIM418 superalloy by heat treatment, J. Mater. Process. Technol. 227 (2016) 71–79.

[105] Ö. Özgün, H.Ö. Gülsoy, R. Yilmaz, F. Findik, Microstructural and mechanical characterization of injection molded 718 superalloy powders.pdf, J. Alloys Compd. 576 (2013) 140–153.

[106] Ö. Özgün, H.Ö. Gülsoy, F. Findik, R. Yilmaz, Microstructure and mechanical properties of injection moulded Nimonic-90 superalloy parts, Powder Metall. 55 (2012) 405–414.

[107] Ö. Özgün, R. Yılmaz, H. Özkan Gülsoy, F. Fındık, The effect of aging treatment on the fracture toughness and impact strength of injection molded Ni-625 superalloy parts, Mater. Charact. 108 (2015) 8–15.

[108] Ö. Özgün, H. Özkan Gülsoy, R. Yilmaz, F. Findik, Injection molding of nickel based 625 superalloy: Sintering, heat treatment, microstructure and mechanical properties, J. Alloys Compd. 546 (2013) 192–207.

[109] L. Zhang, D. Li, X. Chen, X. Qu, M. Qin, X. He, Z. Li, J. Wang, Microstructure and mechanical properties of MIM213 superalloy, Mater. Chem. Phys. 168 (2016) 18–26.

[110] C.F. Tang, F. Pan, X.H. Qu, B.H. Duan, X.B. He, Nickel base superalloy GH4049 prepared by powder metallurgy, J. Alloys Compd. 474 (2009) 201–205.

[111] Y. Behnamian, A. Mostafaei, A. Kohandehghan, B.S. Amirkhiz, D. Serate, Y. Sun, S. Liu, E. Aghaie, Y. Zeng, M. Chmielus, W. Zheng, D. Guzonas, W. Chen, J.L. Luo, A comparative study of oxide scales grown on stainless steel and nickel-based superalloys in ultra-high temperature supercritical water at 800°C, Corros. Sci. 106 (2016) 188–207.

[112] Q. Jia, D. Gu, Selective laser melting additive manufactured Inconel 718 superalloy parts: High-temperature oxidation property and its mechanisms, Opt. Laser Technol. 62 (2014) 161–171.

[113] M. Turker, D. Godlinski, F. Petzoldt, Effect of production parameters on the properties of IN 718 superalloy by three-dimensional printing, Mater. Charact. 59 (2008) 1728–1735.

[114] R.M. German, Supersolidus liquid-phase sintering of prealloyed powders, Metall. Mater. Trans. A. 28 (1997) 1553–1567.

[115] Y. Liu, R. Tandon, R.M. German, Modeling of supersolidus liquid phase sintering: I. Capillary force, Metall. Mater. Trans. A. 26 (1995) 2415–2422.

[116] Y. Liu, R. Tandon, R.M. German, Modeling of supersolidus liquid phase sintering: II. Densification, Metall. Mater. Trans. A. 26 (1995) 2423–2430.

[117] J. Mittra, J.S. Dubey, S. Banerjee, Acoustic emission technique used for detecting early stages of precipitation during aging of Inconel 625, Scr. Mater. 49 (2003) 1209–1214. 203004883.

[118] S.K. Rai, A. Kumar, V. Shankar, T. Jayakumar, K. Bhanu Sankara Rao, B. Raj, Characterization of microstructures in Inconel 625 using X-ray diffraction peak broadening and lattice parameter measurements, Scr. Mater. 51 (2004) 59–63.

[119] A. Sarkar, P. Mukherjee, P. Barat, T. Jayakumer, S. Mahadevan, S.K. Rai, Lattice Misfit Measurement in Inconel 625 By X-Ray Diffraction Technique, Int. J. Mod. Phys. B. 23 (2008) 3977–3985.

[120] A. Mostafaei, Y. Behnamian, Y.L. Krimer, E.L. Stevens, J.L. Luo, M. Chmielus, Effect of solutionizing and aging on the microstructure and mechanical properties of powder bed binder jet printed nickel-based superalloy 625, Mater. Des. 111 (2016) 482–491.

[121] Z. Yan, S. Hara, N. Shikazono, Effect of powder morphology on the microstructural characteristics of La 0.6 Sr 0.4 Co 0.2 Fe 0.8 O 3 cathode: A Kinetic Monte Carlo investigation, Int. J. Hydrogen Energy. 42 (2017) 12601–12614.

[122] L.G. Campbell, R.M. German, Detailed linkage of powder characteristics to properties in

press-sintered of powder metalls, Adv. Powder Metall. Part. Mater. (2007) 1–19.

[123] L.C. Lim, P.M. Wong, M. Jan, Microstructural evolution during sintering of near-monosized agglomerate-free submicron alumina powder compacts, Acta Mater. 48 (2000) 2263–2275.

[124] S. Hara, A. Ohi, N. Shikazono, Sintering analysis of sub-micron-sized nickel powders: Kinetic Monte Carlo simulation verified by FIB-SEM reconstruction, J. Power Sources. 276 (2015) 105–112.

[125] P.W. Trester, J.L. Kaae, R. Gallix, Fatigue strength of inconel 625 plate and weldments used in the DIII-D configuration vacuum vessel, J. Nucl. Mater. 133–134 (1985) 347–350.

[126] P. Ganesh, R. Kaul, C.P. Paul, P. Tiwari, S.K. Rai, R.C. Prasad, L.M. Kukreja, Fatigue and fracture toughness characteristics of laser rapid manufactured Inconel 625 structures, Mater. Sci. Eng. A. 527 (2010) 7490–7497.

[127] J.F. Grubb, Fatigue Resistance of Alloy 625 Sheet, Miner. Met. Mater. Soc. (1997) 629–637.

[128] P. Edwards, M. Ramulu, Fatigue performance evaluation of selective laser melted Ti-6Al-4V, Mater. Sci. Eng. A. 598 (2014) 327–337.

[129] A. Mostafaei, E.L. Stevens, E.T. Hughes, S.D. Biery, C. Hilla, M. Chmielus, Powder bed binder jet printed alloy 625: densification, microstructure and mechanical properties, Mater. Des. 108 (2016) 126–135.

[130] A. Mostafaei, E.L. Stevens, J.J. Ference, D.E. Schmidt, M. Chmielus, Binder jetting of a complex-shaped metal partial denture framework, Addit. Manuf. 21 (2018) 63–68.

[131] E. Wheat, Process Mapping and Optimization of Titanium Parts Made by Binder Jetting Additive Manufacturing by, (2018).

[132] E. Sheydaeian, Z. Fishman, M. Vlasea, E. Toyserkani, On the effect of throughout layer thickness variation on properties of additively manufactured cellular titanium structures, Addit. Manuf. 18 (2017) 40–47.

[133] J.J.S. Dilip, H. Miyanaji, A. Lassell, T.L. Starr, B. Stucker, A novel method to fabricate TiAl intermetallic alloy 3D parts using additive manufacturing, Def. Technol. 13 (2017) 72–76.

[134] D. Hong, D.T. Chou, O.I. Velikokhatnyi, A. Roy, B. Lee, I. Swink, I. Issaev, H.A. Kuhn, P.N. Kumta, Binder-jetting 3D printing and alloy development of new biodegradable Fe-Mn-Ca/Mg alloys, Acta Biomater. 45 (2016) 375–386.

[135] A. Levy, A. Miriyev, A. Elliott, S.S. Babu, N. Frage, Additive manufacturing of complex-shaped graded TiC/steel composites, Mater. Des. 118 (2017) 198–203.

[136] D.S.D. Uduwage, Binder Jet Additive Manufacturing of Stainless Steel-Hydroxyapatite Bio-composite, 2015.

[137] M. Doyle, K. Agarwal, W. Sealy, K. Schull, Effect of Layer Thickness and Orientation on Mechanical Behavior of Binder Jet Stainless Steel 420 + Bronze Parts, Procedia Manuf. 1 (2015) 251–262.

[138] Y. Tang, Y. Zhou, T. Hoff, M. Garon, Y.F. Zhao, Elastic modulus of 316 stainless steel lattice structure fabricated via binder jetting process, Mater. Sci. Technol. 32 (2016) 648–656.

[139] T. Do, P. Kwon, C.S. Shin, Process development toward full-density stainless steel parts with binder jetting printing, Int. J. Mach. Tools Manuf. 121 (2017) 50–60.

[140] A. Kumar, Y. Bai, A. Eklund, C.B. Williams, Effects of Hot Isostatic Pressing on Copper Parts Fabricated via Binder Jetting, Procedia Manuf. 10 (2017) 935–944.

[141] R.K. Enneti, K.C. Prough, T.A. Wolfe, A. Klein, N. Studley, J.L. Trasorras, Sintering of WC-12%Co processed by binder jet 3D printing (BJ3DP) technology, Int. J. Refract. Met. Hard Mater. (2017).

[142] P. Stoyanov, K. Andre, P. Prichard, M. Yao, C. Gey, Microstructural and Mechanical Characterization of Mo-containing Stellite Alloys Produced by three Dimensional Printing, Procedia CIRP. 45 (2016) 167–170.

[143] M.P. Caputo, A.E. Berkowitz, A. Armstrong, P. Müllner, C.V. Solomon, 4D Printing of Net Shape Parts Made from Ni-Mn-Ga Magnetic Shape Memory Alloys, Addit. Manuf. 21 (2018) 579–588.

[144] A. Mostafaei, P. Rodriguez De Vecchis, E.L. Stevens, M. Chmielus, Sintering regimes and resulting microstructure and properties of binder jet 3D printed Ni-Mn-Ga magnetic shape memory alloys, Acta Mater. 154 (2018) 355–364.

[145] M.N. Islam, S. Sacks, An experimental investigation into the dimensional error of powder-binder three-dimensional printing, Int. J. Adv. Manuf. Technol. 82 (2016) 1371–1380.

[146] M. Doyle, K. Agarwal, W. Sealy, K. Schull, Effect of Layer Thickness and Orientation on Mechanical Behavior of Binder Jet Stainless Steel 420 + Bronze Parts, Procedia Manuf. XXX (2015) 1–12.

[147] A. Mostafaei, E. Stevens, E. Hughes, S. Biery, C. Hilla, M. Chmielus, Powder bed binder jet printed alloy 625: densification, microstructure and mechanical properties, Mater. Des. 108 (2016) 126–135.

[148] A. Mostafaei, E.T. Hughes, C. Hilla, E.L. Stevens, M. Chmielus, Data on the densification during sintering of binder jet printed samples made from water- and gas-atomized alloy 625 powders, Data Br. 10 (2016) 116–121. doi:10.1016/j.dib.2016.11.078.

[149] D. Hong, D.T. Chou, O.I. Velikokhatnyi, A. Roy, B. Lee, I. Swink, I. Issaev, H.A. Kuhn, P.N. Kumta, Binder-jetting 3D printing and alloy development of new biodegradable Fe-Mn-Ca/Mg alloys, Acta Biomater. 45 (2016) 375–386.

[150] M. Ziaee, E.M. Tridas, N.B. Crane, Binder-Jet Printing of Fine Stainless Steel Powder with Varied Final Density, Jom. (2016).

[151] S. Ahn, S.J. Park, S. Lee, S. V. Atre, R.M. German, Effect of powders and binders on material properties and molding parameters in iron and stainless steel powder injection molding process, Powder Technol. 193 (2009) 162–169.

[152] C.A. Schneider, W.S. Rasband, K.W. Eliceiri, NIH Image to ImageJ: 25 years of image analysis, Nat. Methods. 9 (2012) 671–675.

[153] ASM-Standard, Metallography and Microstructures of Nonferrous Alloys, ASM Handb. 9 (2004) 711–751.

[154] ASTM E466-07. Standard practice for conducting constant amplitude axial fatigue tests of metallic materials. Annual book of ASTM standards, vol. 03.01. American Society for Automotive Engineers; 1993., (n.d.).

[155] J. McCall, W. Mueller, Microstructural Anlaysis Tools and Techniques, Plenum Press, 1973.

[156] J. Liu, A. Lal, R.M. German, Densification and shape retention in supersolidus liquid phase sintering, Acta Mater. 47 (1999) 4615–4626.

[157] T. Chen, I. Nettleship, R.J. McAfee, T.R. Hinklin, K.G. Ewsuk, An experimental measurement of effective diffusion distance for the sintering of ceramics, J. Am. Ceram. Soc. 92 (2009) 1481–1486.

[158] I. Nettleship, B.R. Patterson, W.S. Slaughter, Evolution of Average Microstructural Properties in the Final Stage Sintering of Alumina, J. Am. Ceram. Soc. 56 (2003) 252–256.

[159] Roger C. Reed, The Superalloys, Fundumentals and Applications, Cambrige University Press, 2006.

[160] A. Simchi, Densification and microstructural evolution during co-sintering of Ni-base superalloy powders, Metall. Mater. Trans. A Phys. Metall. Mater. Sci. 37 (2006) 2549–2557.

[161] A. Mostafaei, E.L. Stevens, E.T. Hughes, S.D. Biery, C. Hilla, M. Chmielus, Powder bed binder jet printed alloy 625: Densification, microstructure and mechanical properties, Mater. Des. 108 (2016) 126–135. http://linkinghub.elsevier.com/retrieve/pii/S026412751630819X.

[162] M. Turker, Formation of porosity in ferritic ODS alloys on high temperature exposure, J. Mater. Sci. 40 (2005) 1201–1208.

[163] H.Ö. Gülsoy, Ö. Özgün, S. Bilketay, Powder injection molding of Stellite 6 powder: Sintering, microstructural and mechanical properties, Mater. Sci. Eng. A. 651 (2016) 914–924.

[164] R. Rolland, C. Issartel, S. Perrier, H. Buscail, Effects of 7·5 vol.-% water vapour on oxidation of nickel based alloy between 900 and 1100°C, Corros. Eng. Sci. Technol. 46 (2011) 634–641.

[165] A. Theriault, L. Xue, J.R. Dryden, Fatigue behavior of laser consolidated IN-625 at room and elevated temperatures, Mater. Sci. Eng. A. 516 (2009) 217–225.

[166] Q. Bader, E.K. Njim, Effect of Stress Ratio and V Notch Shape on Fatigue Life in Steel Beam, Int. J. Sci. Eng. Res. 5 (2014) 1145–1154.

[167] F.C. Campbell, Fatigue and fracture: understanding the basics. ASM International., 2012.

[168] Fatigue - ASM International, Elements of Metallurgy and Engineering Alloys, Chapter 14 (2008) 243–265.

[169] T.D. Jacobs, T. Junge, L. Pastewka, Quantitative characterization of surface topography using spectral analysis, Surf. Topogr. Metrol. Prop. 5 (2017) 13001.

[170] S. Dai, Y. Zhu, Z. Huang, Microstructure evolution and strengthening mechanisms of pure titanium with nano-structured surface obtained by high energy shot peening, Vacuum. 125 (2016) 215–221.

[171] O. Unal, R. Varol, Surface severe plastic deformation of AISI 304 via conventional shot peening, severe shot peening and repeening, Appl. Surf. Sci. 351 (2015) 289–295.

[172] O. Unal, E. Maleki, R. Varol, Effect of severe shot peening and ultra-low temperature plasma nitriding on Ti-6Al-4V alloy, Vacuum. 150 (2018) 69–78.

[173] M. Benedetti, M. Cazzolli, V. Fontanari, M. Leoni, Fatigue limit of Ti6Al4V alloy produced by Selective Laser Sintering, Procedia Struct. Integr. 2 (2016) 3158–3167.

[174] P. Li, D.H. Warner, A. Fatemi, N. Phan, Critical assessment of the fatigue performance of additively manufactured Ti-6Al-4V and perspective for future research, Int. J. Fatigue. 85 (2016) 130–143. doi:10.1016/j.ijfatigue.2015.12.003.

[175] D. Greitemeier, C. Dalle Donne, F. Syassen, J. Eufinger, T. Melz, Effect of surface roughness on fatigue performance of additive manufactured Ti–6Al–4V, Mater. Sci. Technol. 32 (2016) 629–634.

[176] S. Leuders, M. Thone, A. Riemer, T. Niendorf, T. Troster, H. Richard, H. Maier, On the mechanical behaviour of Titanium alloy Ti-6Al-4V manufactured by Selective Laser Melting: fatigue resistance and crack growth performance, Int. J. Fatigue. 48 (2012) 300–307.

[177] O. Scott-Emuakpor, J. Schwartz, T. George, C. Holycross, C. Cross, J. Slater, Bending fatigue life characterisation of direct metal laser sintering nickel alloy 718, Fatigue Fract. Eng. Mater. Struct. 38 (2015) 1105–1117. doi:10.1111/ffe.12286.

[178] S. Gribbin, J. Bicknell, L. Jorgensen, I. Tsukrov, M. Knezevic, Low cycle fatigue behavior of direct metal laser sintered Inconel alloy, Int. J. Fatigue. 93 (2016) 156–167.

[179] D. Arola, M. Ramulu, An examination of the effects from surface texture on the strength of fiber reinforced plastics, J. Compos. Mater. 33 (1999) 102–123.

[180] M. Suraratchai, J. Limido, C. Mabru, R. Chieragatti, Modelling the influence of machined surface roughness on the fatigue life of aluminium alloy, Int. J. Fatigue. 30 (2008) 2119–2126.

[181] M. Dourandish, D. Godlinski, A. Simchi, V. Firouzdor, Sintering of biocompatible P/M Co-Cr-Mo alloy (F-75) for fabrication of porosity-graded composite structures, Mater. Sci. Eng. A. 472 (2008) 338–346.

[182] W.S. Slaughter, I. Nettleship, M.D. Lehigh, P.P.-O. Tong, A quantitative analysis of the effect of geometric assumptions in sintering models, Acta Mater. 45 (1997) 5077–5086.